ABSTRACT

Title of dissertation: MEASUREMENT OF $1/\sigma$ dσ/dy FOR $Z/\gamma^* \rightarrow e^+e^-$ AT $\sqrt{S} = 1.96$ TeV

Ming Yan, Doctor of Philosophy, 2007

Dissertation directed by: Professor Andrew Baden
Department of Physics

Author presents the measurement of $p\bar{p} \rightarrow Z/\gamma^* \rightarrow e^+e^- + X$ inclusive differential cross section as a function of boson rapidity. The data, which correspond to an integrated luminosity of 0.4 fb^{-1}, were collected with $D\O$ detector at Tevatron $p\bar{p}$ collider. At the Run II energy of $\sqrt{s}=$ 1.96 TeV, Z bosons are produced with rapidity out to $\pm$ 3. The cross section is measured in a mass range between 71 to 111 GeV for the allowed kinematic range.

MEASUREMENT OF $1/\sigma \mathrm{d}\sigma/\mathrm{dy}$ FOR $Z/\gamma^* \rightarrow e^+e^-$ AT $\sqrt{S} = 1.96$ TeV

by

Ming Yan

Dissertation submitted to the Faculty of the Graduate School of the
University of Maryland, College Park in partial fulfillment
of the requirements for the degree of
Doctor of Philosophy
2007

Advisory Committee:

Professor Andrew R. Baden, Chair/Advisor
Professor Nicholas J. Hadley
Professor Rabindra N. Mohapatra
Professor Patrick G. O'Shea
Accociate Professor Douglas A. Roberts

ACKNOWLEDGMENTS

I would like to thank my dissertation advisor, Professor Andrew Baden, for the opportunity to work with him and for his encouragement, inspiration and guidance over the past years on this research project. I am truly grateful for all that I have learned from him. I am also indebted to Dr. Terrence Toole for his mentorship, helpful discussions and ideas during my time at Fermi lab.

In addition, I would like to thank Professor Sarah Eno, Professor Nicholas Hadley, and Professor Ia Iashvili for their encouragement, guidance, and helpful discussions, and acknowledge help from Professor Jeremiah Mans, Dr. Marco Verzocchi and Chad Jarvis.

I owe my gratitude to all the people who have made this dissertation possible.

This work was supported in part by the US Department of Energy, Division of High Energy Physics under Grant Number DE-FG05-97ER41015.

Table of Contents

List of Tables

List of Figures

Outline of this dissertation

This dissertation presents the $1/\sigma d\sigma/dy$ differential cross section measurement of Z boson decaying to electron positron pair as a function of Z boson rapidity. The dissertation starts with a general introduction of Z/γ^* production at Tevatron and the motivation of this measurement. It is followed by a brief overview of Tevatron and the *DØ* detector.

The detail of this measurement starts in Chapter 3, where the events selection are discussed. The efficiencies associated with these events selections are presented in the following chapter. Z boson efficiency×acceptance is calculated based on the Monte Carlo simulation using the measured electron efficiencies. Data and Monte Carlo simulation are also compared side by side to verify the validity of the Monte Carlo simulation. These processes are covered in Chapter 5. In addition, the systematic and statistical uncertainties of this measurement are presented in Chapter 6. The final results are given in Chapter 7, followed by a brief analysis in Chapter 8.

Chapter 1

Z and Drell-Yan Production at Tevatron

In this chapter the author presents a brief introduction of the hadron collider and parton model, as well as an overview of kinematics of Z and Drell-Yan production at Tevatron. The author also discusses how the study on distribution of Z boson in rapidity can be used to probe parton distribution functions.

1.1 Hadron collider and parton model

Tevatron is a hadron collider with proton (p) and anti-proton ($\overline{p}$) beams at 1.96 TeV center of mass energy. Proton and anti-proton are composite particles made of partons. The parton is a collection of quarks and gluons, which are the elements in reaction during proton anti-proton collision. Assuming a parton in $p\bar{p}$ collision carrying fraction x ($0 \leq x \leq 1$) of hadron momentum p^{μ}. Define the probability to find parton i carries fraction x of momentum is $f_i(x, Q^2)$, where Q^2 is the momentum-squared transfer in the hard scattering. When we sum over all partons of a proton, we have:

$$\sum_i \int x f_i(x, Q^2) dx = 1 \tag{1.1}$$

If life time of parton is τ in the parton rest frame. The value in the center of mass frame is $\tau/\sqrt{(1 - v^2/c^2)} \gg \tau$, where v is the velocity of parton. This means that the lifetime of a parton tends to be infinity for the incoming particles. Or the parton state looks *frozen* if viewed by the incoming particles. Because the partons are *frozen* for incoming particles, probability for the incoming particles to find a nearby parton in a hard scattering will be suppressed by a factor of $1/Q^2\pi R_0^2$, where R_0 is the radius of parton.

Based on the above assumptions, we can use *Born* approximation and parton distribution probability $f_i(x, Q^2)$ to calculate cross section involving parton process even without knowing the structure of a parton. For example, in an inclusive process of proton anti-proton to final state F, cross section can be derived by summing over all partons involved in this process:

$$\sigma(p\overline{p} \to F + X) = \sum_{i,j} \int_0^1 dx dx^{'} \sigma_{ij}(xP, x^{'}P^{'}) f_i(x, Q^2) f_j(x^{'}, Q^2) \tag{1.2}$$

where σ_{ij} is the *Born* approximation of cross section of parton i, j to final state F. $f_i(x, Q^2)$ and $f_j(x^{'}, Q^2)$ are the parton distribution probabilities, or called patron distribution functions (PDF) of the parton i and j, respectively . PDFs are derived from various experiments. By knowing the PDF, one can calculate hard scattering cross section in the hadron collider. On the other hand, the cross section measurements also provide inputs PDF determination.

1.2 Parton distribution function

Parton distribution function $f(x, Q^2)$ gives parton distribution probability as functions of momentum fraction x and invariant momentum-squared transferred Q^2. It is determined by the various experimental data. The most commonly used PDFs are made by Alekhin [3], CTEQ [4], and MRST [5]. Among those PDFs, CTEQ PDFs are more widely used in the *DØ* [1] experiment. CTEQ6 is the most recent CTEQ PDF set. There are many sub-sets in CTEQ6 PDFs. CTEQ6M is the sub-set of CETQ PDF with the next-to-leading (NLO) fitting of the global inputs. CTEQ6L is the leading order (LO) one. In this analysis, CTEQ6M PDF set is used in Monte Carlo events generator. MRST and Alekhin PDF sets are also used in theoretical calculation to cross check the experimental results by using CTEQ6M PDF.

CTEQ PDFs are described in the following equation [9]:

$$xf(x, Q^2) = A_0 x^{A_1} (1 - x)^{A_2} e^{A_3 x} (1 + e^{A_4} x)^{A_5} \tag{1.3}$$

Each of u_v, d_v and $\bar{u} + \bar{d}$ has a set of independent parameters. An additional equation is used to distinguish $\bar{d}$ and $\bar{u}$:

$$\bar{d}(x,Q^2)/\bar{u}(x,Q^2) = A_0 x^{A_1}(1-x)^{A_2} + (1+A_3 x)(1-x)^{A_4} \tag{1.4}$$

There are total twenty parameters to determine one parton distribution function at Q^2.

CTEQ6M parton distributions at different values of Q^2 are plotted on FIG 1.1. Left of FIG 1.1 shows $Q = 2\ GeV$ and right plot has $Q = 100\ GeV$. Those plots indicate valence quarks and gluons more tend to have large x value, and sea quarks are more dominant at small x regions. When Q^2 increases, small x regions are more dominant by the sea quarks.

As described in equation 1.3 and 1.4, each of the CTEQ6 PDF set has 20 parameters. By shifting one of those 20 parameters one σ away from their respective central value, the PDF set has total 40 variations. Those additional 40 variations can be used to determine the systematic uncertainty from this PDF.

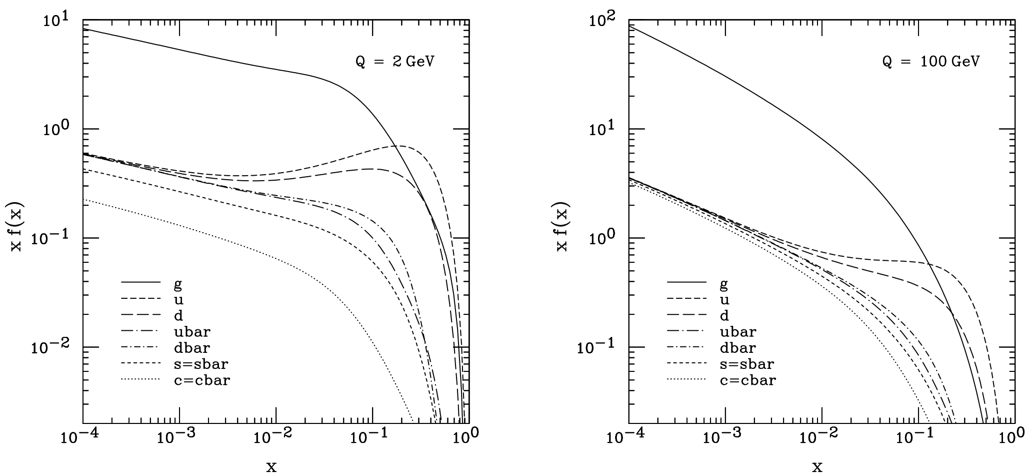

Figure 1.1: CTEQ6M PDFs at Q=2 GeV and Q=100 GeV [9]

1.3 WZ production through Drell-Yan process

Starting with parton level differential cross section of $Z/\gamma^* \to l\bar{l}$ process:

$$\frac{d\widehat{\sigma}(q\overline{q} \to z/\gamma^* \to l\bar{l})}{dcos\theta} = \frac{1}{32\pi\widehat{s}}\overline{|\mathcal{M}|^2}; \tag{1.5}$$

Where the leading order matrix element is:

$$\overline{|\mathcal{M}|^2} = \frac{1}{36}\sum_{color}\sum_{spin}|\mathcal{M}|^2 = \frac{1}{36}\frac{e_f^2 g_2^4 sin^4\theta_W}{q^4}\sum_{color}\sum_{spins}\gamma^{\alpha}_{ab}\gamma^{\beta}_{cd}\gamma_{\alpha ab}\gamma_{\beta cd} \tag{1.6}$$

The above process starts with quark and anti-quark annihilating to Z boson or γ^*, and then decays to two opposed charged leptons. In hadron collider, the Z/$\gamma^* \rightarrow l\bar{l}$ process involves the parton process. The cross section is modified to:

$$\frac{d\sigma(p\bar{p} \rightarrow Z + X)}{dy} = \sum_{ij}\int dx_i \int dx_j f(x_i, Q^2) f(x_j, Q^2) \frac{d\sigma(ij \rightarrow Z)}{dy} \tag{1.7}$$

The next to next leading order differential cross section can also be derived. FIG 1.2 shows the results from the next to next leading order calculation. The calculation on FIG 1.2 is based on the study by Anastasiou et al [14], with the latest PDFs from CTEQ, MRST and Alekhin and $D\O$ parameters: invariant mass window is 71 to 111 GeV. Proton and anti-proton center of mass energy is $\sqrt{S} = 1.96$ TeV.

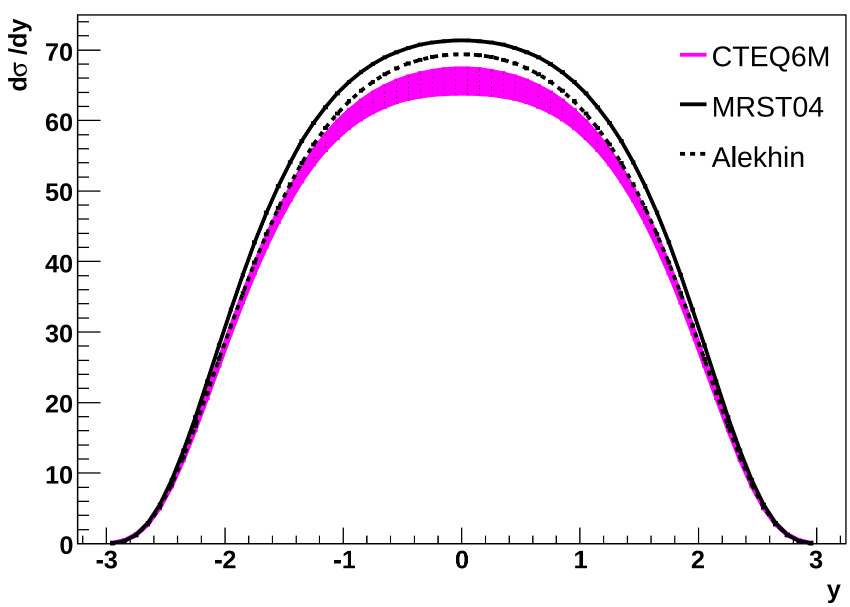

Figure 1.2: Theoretical calculation of $d\sigma(Z/\gamma^* \rightarrow e^+e^-)$/dy distribution using different PDF sets. The distribution from CTEQ6M shows the band with 40 variations of PDF.

Besides the difference in total cross section predicted by different PDFs, there are differences in shape after scaling those curves to their respective total cross sections (FIG 1.3). The main causes of these differences are [8]: MRST and CTEQ [9] use different types of parameterization (equation 1.3); CTEQ uses data with $Q^2 > 4\ GeV^2$, and MRST uses data with $Q^2 > 2\ GeV^2$; CTEQ does not use SLAC data and one H1 high-Q^2 set of F_2 data; CTEQ uses positive-define small-x gluon at starting scale of $Q_0^2 = 1.69\ GeV^2$. Those different approaches cause difference in gluon distribution, and lead to difference in Z boson rapidity distribution. Since contribution of small x large Q^2 data to Z boson rapidity distribution is small, the difference in the shape of Z boson rapidity distribution from MRST and CTEQ PDF is not obvious (FIG 1.3).

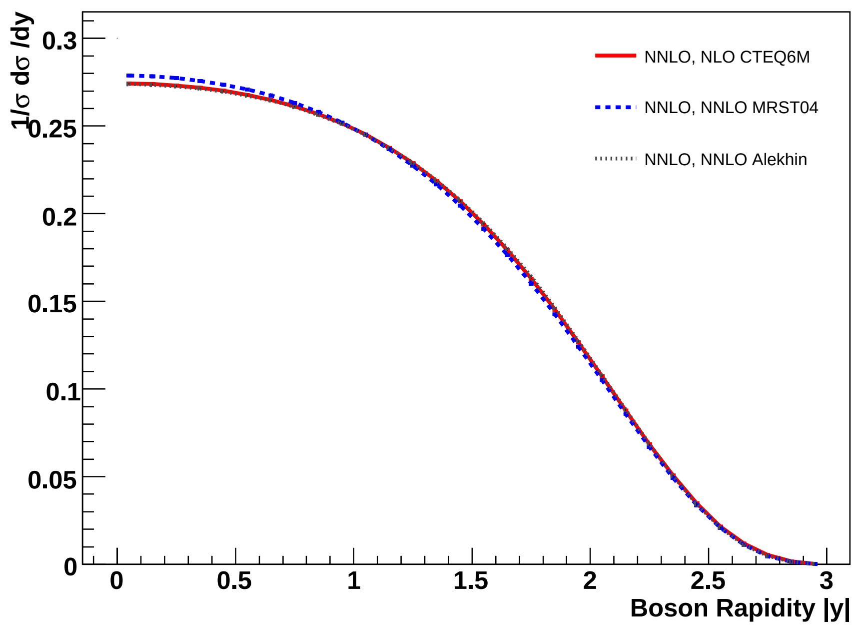

Figure 1.3: Theoretical calculation of $1/\sigma d\sigma(Z/\gamma^* \to e^+e^-)$/dy distribution using different PDF sets

1.4 Quark substructure

If quarks have substructure, a simple model to describe quark compositeness is to apply a form factor $F(q^2) \simeq 1 + q^2/\Lambda^2$ to the gauge propagator [10]. Compositeness signals are then related to the mass scale Λ. When $\Lambda \gg \sqrt{\hat{s}}$, the form factor is unity and the dominant signals are still from QCD. CDF reported an observation consistent with quark compositeness in 1996 [11]. However, further studies show that the upper limit on Λ for quark compositeness (at the 95% confidence level) is higher than 2 TeV. For example, *DØ* reported limits of quark compositeness with constructive interference (Λ^+) and destructive interference (Λ^-): $\Lambda^+ > 2.7$ TeV, and $\Lambda^- > 2.4$ TeV (with $\mu = E_T^{max}$ and CTEQ3M) [12], which are much higher than the CDF results.

At low x region, the contribution to quark compositeness measurements strongly depends on the jet energy scale measurement. The large uncertainty from jet energy scale, with large fluctuations in the measured jet energy can fake a compositeness signal. In high x region, the PDFs play a more important role. Since the uncertainty from jet energy scale does not contribute to the measurement of Z boson rapidity distribution, the Z boson rapidity analysis provides a method to check how current PDFs differ from the experimental measurement at high Q^2 and large x. This can help us understand the relationship between PDFs and the quark compositeness.

With the current amount of integrated luminosity used in this measurement, the statistical uncertainty is larger than the uncertainties from PDFs. It is difficult to see the quark compositeness signal using this measurement. But quark substructure will be a good topic for the future Z boson rapidity analysis when enough integrated luminosity is reached.

1.5 Kinematics

Consider a particle with rest mass M and momenta $\mathbf{p}$ in a frame A, (E, $\mathbf{p}$) is the four momentum of this particle. Rapidity y is defined in energy E, and momentum z component in the following way:

$$y = \frac{1}{2} ln \frac{E + p_z}{E - p_z} \tag{1.8}$$

Now consider there is a boost along z axis with respect to the frame A, with relative velocity β_0. Using *Lorentz* transformation, four momentum (E', $\mathbf{p}'$) under boost is:

$$
\begin{pmatrix} E' \\ p'_z \end{pmatrix} = \begin{pmatrix} \gamma_0 & -\gamma_0\beta_0 \\ -\gamma_0\beta_0 & \gamma_0 \end{pmatrix} \begin{pmatrix} E \\ p_z \end{pmatrix}
$$

$$
= \begin{pmatrix} \cosh y_0 & -\sinh y_0 \\ -\sinh y_0 & \cosh y_0 \end{pmatrix} \begin{pmatrix} E \\ p_z \end{pmatrix}, \tag{1.9}
$$

where $y_0 = \frac{1}{2}ln((1+\beta_0)/(1-\beta_0))$, and $\gamma_0 = 1/\sqrt{1-\beta_0^2}$. New rapidity y' under boost is:

$$
y' = \frac{1}{2}ln\frac{E'+p'_z}{E'-p'_z} = \frac{1}{2}ln\frac{(1-\beta_0)(E+p_z)}{(1+\beta_0)(E-p_z)} = y - y_0 \tag{1.10}
$$

This indicates *Lorentz* boost β_0 along z axis only adds a constant term y_0 to rapidity y. Rapidity y is invariant under boost.

If we define momentum fraction of two partons involved in collision is $x_1 = p_1/P_A$, and $x_2 = p_2/P_B$. Rapidity y can also rewrite in form of x_1, and x_2:

$$
y = \frac{1}{2}ln\frac{x_1}{x_2} \tag{1.11}
$$

Notice center of mass energy $\sqrt{s} = (P_A + P_B)$. In the leading order, momentum transferred Q must satisfy on-shell condition, that is:

$$
Q^2 = x_1 x_2 s \tag{1.12}
$$

Immediately we have equation 1.13 for Z/γ^* analysis, with momentum transferred Q equals to the mass of Z boson:

$$
x_{1,2} = \frac{M_Z}{\sqrt{s}}e^{\pm y} \tag{1.13}
$$

Equation 1.13 indicates large rapidity of Z boson will either have small or large momentum fraction x. Fig 1.5 shows the CTEQ6M PDF distribution at $Q^2 = M_Z^2$. Study rapidity distribution of particles with high Q^2, such as Z boson, especially study its distribution at the higher rapidity region, can provide a window to probe the distribution of sea quarks (at large x), valence quarks and gluons (at small x).

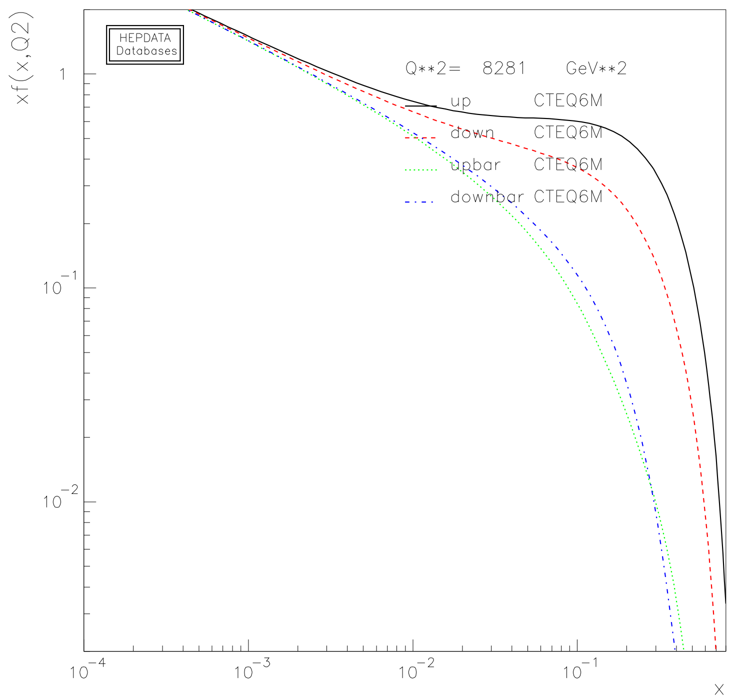

Figure 1.4: CTEQ6M PDF distribution at $Q^2 = M_Z^2$

1.6 Summary

This Z boson rapidity distribution measurement is a measurement at high Q^2 and large x region. High Q^2 and large x value measurements are usually covered by inclusive jet cross section measurement [7]. However, the measurement of jet cross section involves large uncertainty from jet energy scale measurement. Z boson rapidity measurement is a measurement at electroweak channel. It has much smaller uncertainty.

The widely used PDF sets: CTEQ, MRST and Alekhin are made based on different treatments, fitting techniques and experimental data. Using different PDF sets in the theoretical calculation can predict different values of cross section and shape of rapidity distributions for the same physics process. The Z boson rapidity distribution measurement can provide a method to test which PDF set is the most favorable one for electroweak physics.

Chapter 2

$D\O$ Detector

$D\O$ detector consists of three major systems: tracking system, calorimeter and muon system. This chapter provides an overview on $D\O$ tracking system, the electronic-magnetic calorimeter and the muon system. The trigger system, the luminosity measurement system, and the energy response of the electronic-magnetic calorimeter are also discussed. FIG 2.1 is the side view of $D\O$ detector.

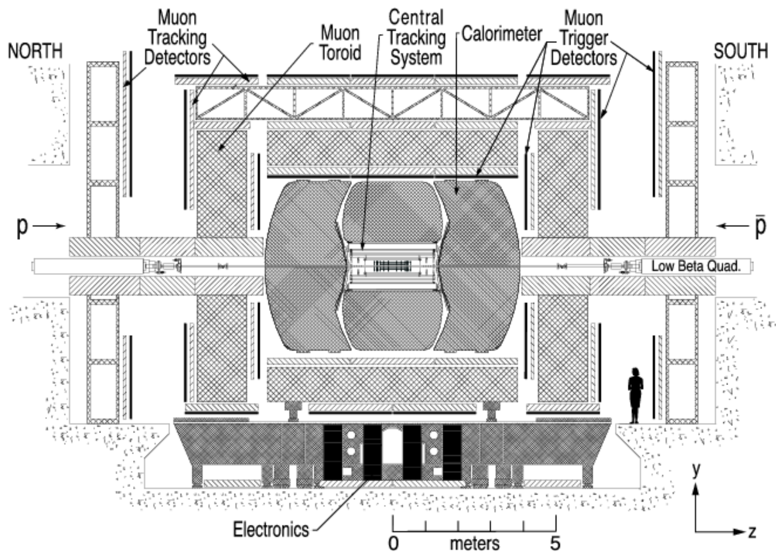

Figure 2.1: A side view of the $D\O$ detector at RunII

2.1 $D\O$ coordinate system

The $D\O$ coordinate system (FIG 2.2) is a right handed *Cartesian* coordinate system. The z axis of $D\O$ coordinate is along the beam pipe, in the direction of proton traveling. The direction of z axis is also called *south* at $D\O$. x, y and z axis are shown on FIG 2.2. A spherical coordinate system (ϕ, θ, z) is also defined. It is used more frequently in this dissertation. In the spherical coordinate system, ϕ is the azimuthal angle along z axis. It becomes positive x axis at $\phi = 0$. θ is the polar angle from (x, z) plane. FIG 2.2 shows $D\O$ coordinate system in both spherical and

$Cartesian$ coordinate.

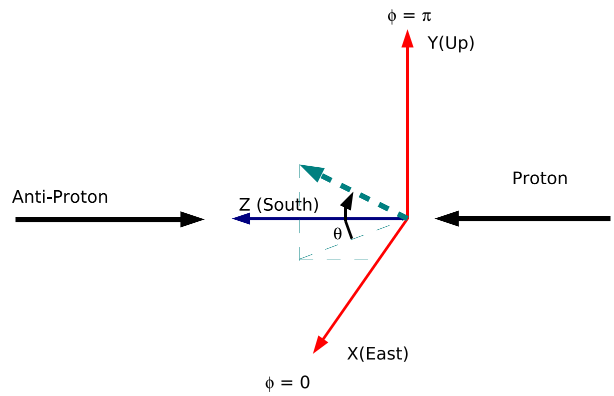

Figure 2.2: $D\emptyset$ coordinate system. The direction of z axis is the direction which proton travels

Rapidity y of a particle with energy E and momentum $\mathbf{p}$ can be written in the following expression:

$$y = \frac{1}{2} ln \frac{1 + \beta cos\theta}{1 - \beta cos\theta} \tag{2.1}$$

When $\beta \to 1$, rapidity y becomes pseudo-rapidity η. The pseudo-rapidity η is more widely used as a substitute of θ in collider experiment, which is defined in the following:

$$\eta = \frac{1}{2} ln \frac{1 + cos\theta}{1 - cos\theta} = -ln(tan\frac{\theta}{2}) \tag{2.2}$$

FIG 2.3 shows the distribution of pseudo-rapidity η at $D\emptyset$ detector.

The proton anti-proton hard scattering center may not be the geometry center of $D\emptyset$ calorimeter. Pseudo-rapidity of event with respect to $D\emptyset$ geometry center is called the detector η, or, η_D. The pseudo-rapidity of event with respect to hard scattering center is called physics η, or η. The hard scattering center is called vertex. $(x_{vtx}, y_{vtx}, z_{vtx})$ is the position of vertex in the

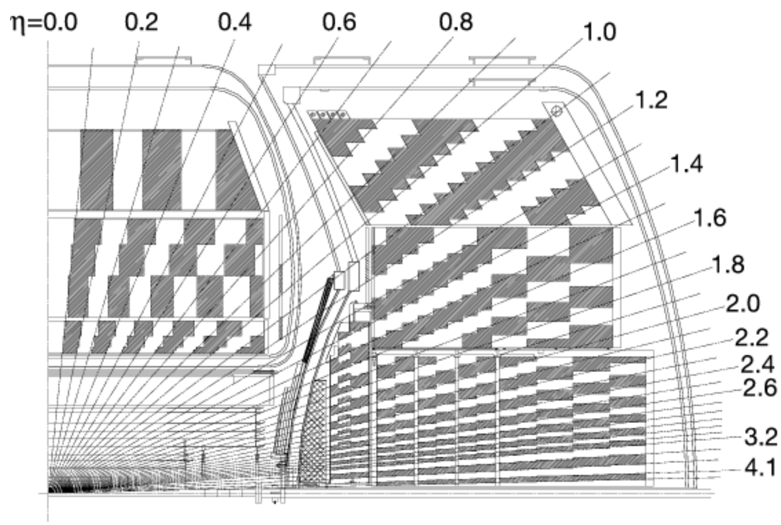

Figure 2.3: Distribution of Pseudo-rapidity η along $D\O$ detector

$D\O$ coordinate system.

2.2 Tracking system

The $D\O$ tracking system consists of a silicon micro-strip tracker (SMT), a central fiber tracker (CFT), and a solenoidal magnet, from inside to outside. The tracking system determines trajectory and vertex position of the charged particles. Tracking system also passes vertex information to the trigger system. FIG 2.4 shows side view of the tracking system.

SMT is located between beam pipe and CFT. It is placed in the central region of the detector, covers almost all η_D range. It has six barrel detectors interspersed with 12 F disks in central and 4 H disks in forward region. The barrier detectors measure r-ϕ coordinate and disk detectors measure r-ϕ and r-z coordinate of a track. Twelve F disks are double-sided smaller disks placed between each of six barrels, exactly located at $|z|$ = 12.5, 25.3, 38.2, 43.1, 48.1 and 53.1 cm. In the forward region, four large H disks are placed at $|z|$ = 100.4, and 121.0 cm. Each of F disks consists of twelve double-sided wedges. Each of H disks has twenty four wedges. The barrel detectors end at $|z| = 38.1$ cm. Each barrel has four silicon readout layers. Since there is no barrel detector beyond 38.1 cm, relative low vertex reconstruction efficiency usually can be observed if

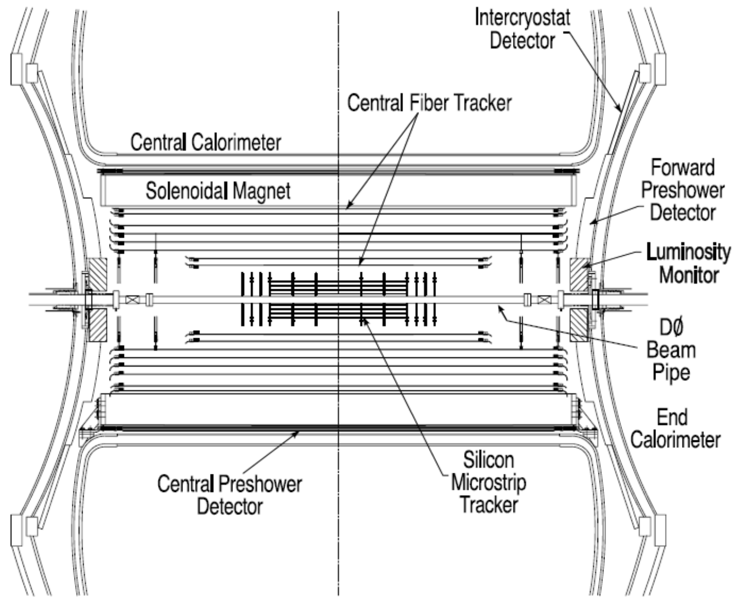

Figure 2.4: The structure of $D\O$ tracking system in x-z plane [17]

z_{vtx} of event is larger than 38 cm. FIG 2.5 shows the design of SMT detector.

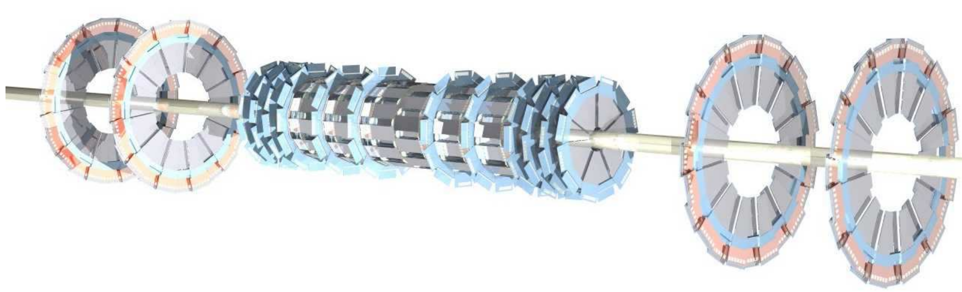

Figure 2.5: The barrels, F disks and H disks of SMT [17]

CFT is installed between 20 to 52 cm from center of beam pipe in radius, surrounding the SMT. Due to size difference between F and H disks, the CFT has two smaller inner cylinders and six larger outer cylinders. Scintillating fibers are mounted on those eight concentric cylinders. The length of two inner cylinders is 1.66 m. The length of outer cylinder is 2.52 m. CFT covers η_D up to 1.7. The scintillating fibers of CFT are connected to wave guides and transmit the collected photons to visible light photon counter cassettes (VLPC) and then send to the read out electronics. The diameter of scintillating fibers is about 835 μm and it provides less than 100 μm of inherent double layer resolution in the measurement.

The surrounding solenoidal magnet is driven by a two-layer superconducting solenoid. It provides a 2 *Tesla* central magnetic field. This magnetic field applies on the tracking system to determine trajectory of charged particle. Outside of the solenoidal magnet is preshower detector. It is composed by a central preshower detector (CPS) and two forward preshower detectors (FPS). The CPS covers $|\eta_D| < 1.3$ of detector, and the FPS covers covers $1.5 < |\eta_D| < 2.5$ of detector. The preshower detector provides electron identification and background rejection information. It helps determine the electromagnetic energy losses in the solenoid and upstream material, and improves the spatial matching between calorimeter shower and the charged particle trajectories. FIG 2.6 shows the perspective view of the solenoid.

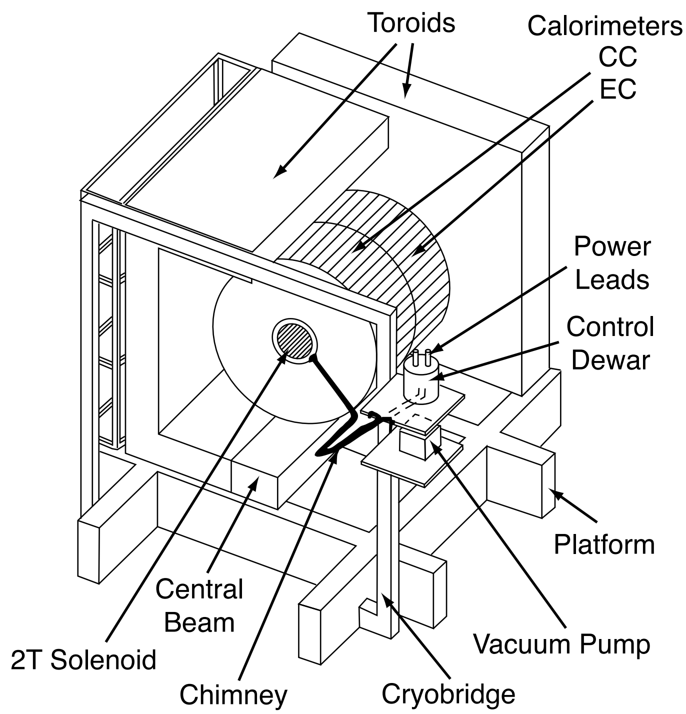

Figure 2.6: Magnetic solenoid inside the central calorimeter [17]

2.3 Calorimeter

DØ calorimeter consists of one central calorimeter (CC), and two end calorimeters (EC north, and EC south), with inter cryostat detector (ICD) and mass-less gaps (MG) located in the gap between CC and EC calorimeter. CC covers $|\eta_D| < 1.2$. ICD covers $1.1 < |\eta_D| < 1.4$, and EC covers $1.4 < |\eta_D| < 4.2$. The structure of $D\O$ calorimeter is shown on FIG 2.7.

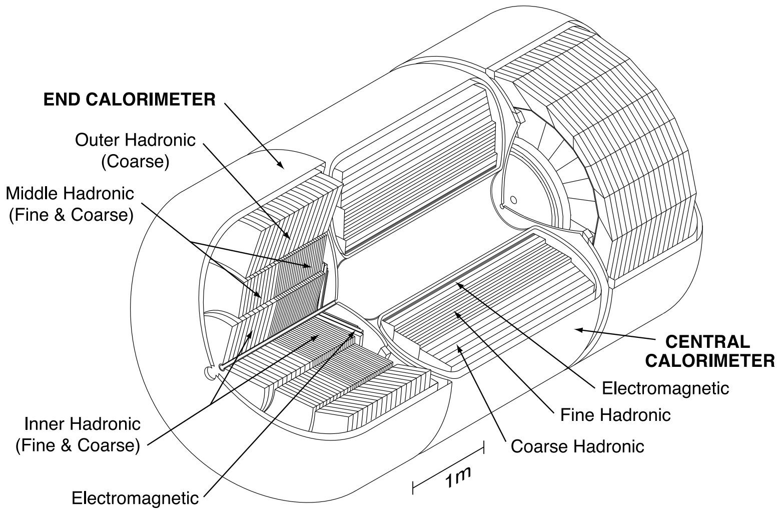

Figure 2.7: The structure of $D\O$ calorimeter [17]

The calorimeter measures energy and shower of electrons, photons and jets. It has electromagnetic and hadronic layers to measure electromagnetic and hadronic shower, respectively. However, the ICD does not have electromagnetic layer. It only provides hadronic energy and shower information.

The electromagnetic layers are located at the inner part of central and end calorimeters. The hadronic layers are placed at the outside of electromagnetic layers. Electromagnetic part of the calorimeter has four readout layers (from EM1 to EM4). Each central electromagnetic layer has 21 cells in radial. Each cell is composed of 3 mm depleted uranium absorber plate filled with a 2.3 mm liquid Argon gap, as shown on FIG 2.9. EM1, EM2, and EM4 electromagnetic layers are layers with 0.1×0.1 in $\eta \times \phi$ transverse segmentation. Since EM3 layer collects most of the electromagnetic energy. It has 0.05×0.05 in $\eta \times \phi$, which is the most finest segmentation. EM layer of end calorimeters has the disk-like shape. Each disk starts from 5.7 cm in radius. But the maximum radius varies from 84 to 104 cm, depends on the distance along z axis where the EM layers of the end calorimeters located. Each of the electromagnetic layers in the end calorimeter has 18 radial cells. Each cell consists of a 4 mm depleted uranium absorber plate filled with 2.3 mm liquid Argon gap, which is the same as those used in central electromagnetic layer. The transverse segmentation has size of 0.1×0.1 in $\eta \times \phi$ when $|\eta_D| < 3.2$ and it is increased to 0.2×0.2 in $\eta \times \phi$ when $|\eta_D| > 3.2$, except the third layer of end calorimeter. The third layer of end calorimeter has segmentation in size of 0.05×0.05 in $\eta \times \phi$ when $|\eta_D| < 2.7$, 0.1×0.1 when $2.7 < |\eta_D| < 3.2$ and 0.2×0.2 if $|\eta_D| > 3.2$.

The hadronic calorimeter has inner fine hadronic layers (FH) and an outer coarse hadronic layer (CH). It is designed to detect hadron part of the energy and shower. The fine hadron layer is made with 6 mm thick uranium-niobium absorbers sandwiched with 2.3 mm liquid Argon gap between those absorbers. There are total 16 fine hadronic (FH) modules and 16 coarse hadronic (CH) modules. In the CC region, each of the fine hadronic modules has 50 radial cells in three layers (FH1 to FH3). Each coarse hadronic layer has 9 radial cells. Each of those cells is made of 4.75 cm thick copper absorber plate filled with 2.3 mm thick liquid Argon. In the EC region, the fine hadronic modules have four layers (FH1 to FH4), but only have one coarse hadronic layer.

FIG 2.8 shows the transverse segmentation of the calorimeter.

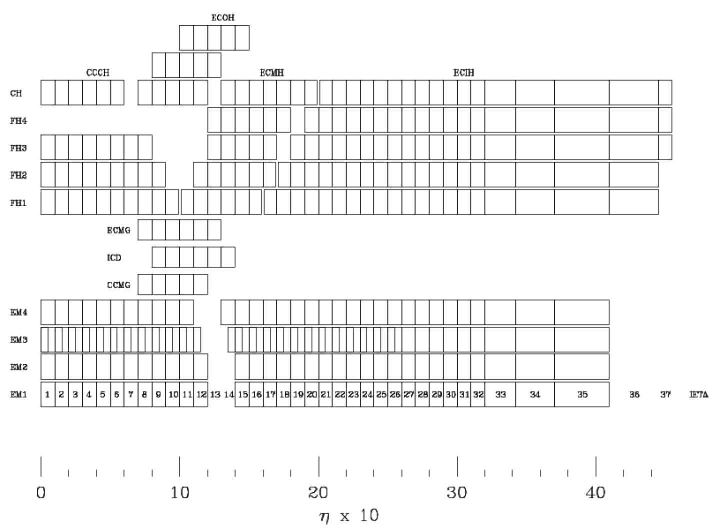

Figure 2.8: Transverse segmentation of $D\emptyset$ calorimeter

FIG 2.9 shows the structure of a calorimeter read out cell. There are copper pads with resistive coat between two absorber plates in the read out cell . The gap between two absorber plates is filled with liquid Argon and applied about 2.0 kV high voltage. High P_T electron loses its energy by *Bremsstrahlung*, high P_T photon loses its energy by pair production when colliding with

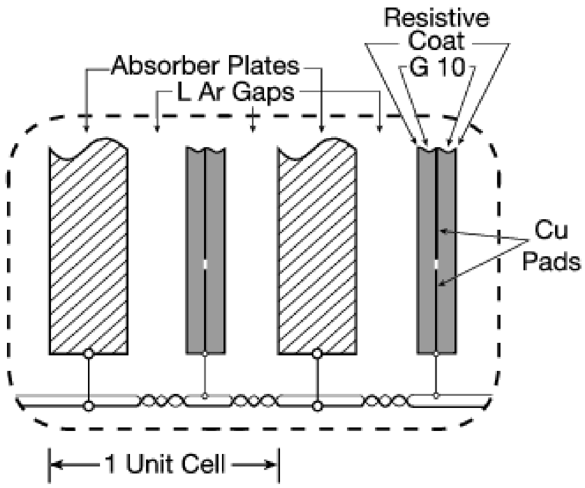

Figure 2.9: Typical calorimeter read out cell [17]

depleted uranium plates inside a cell. The second generation of photons and electrons will also generate new generation of photons and electrons by *Bremsstrahlung* and pair production. As a result, electromagnetic shower is formed when electrons and photons collide with the cells. Define the radiation length X_0, which is the thickness of the absorber plates that loses $1/e$ of the initial energy:

$$\frac{dE}{E} = -\frac{dx}{X_0} \tag{2.3}$$

In order to optimize electromagnetic and hadronic showers, plates with different thickness are used. In CC, thickness of four EM layers is approximate 1.4, 2.0, 6.8 and $9.8X_0$, in EC, thickness is about 1.6, 2.6, 7.9 and $9.3X_0$ [17], respectively.

$\mathrm{Z} \to e^+e^-$ invariant mass distribution and $\mathrm{J}/\psi \to e^+e^-$ resonance peak are used in an *in situ* calibration of electromagnetic energy resolution. Photon-jet events are used to measure calorimeter response. Di-jets and photon-jet events are used to determine hadronic energy resolution. FIG 2.10 shows the hadronic energy resolution [18] of $D\varnothing$ calorimeter.

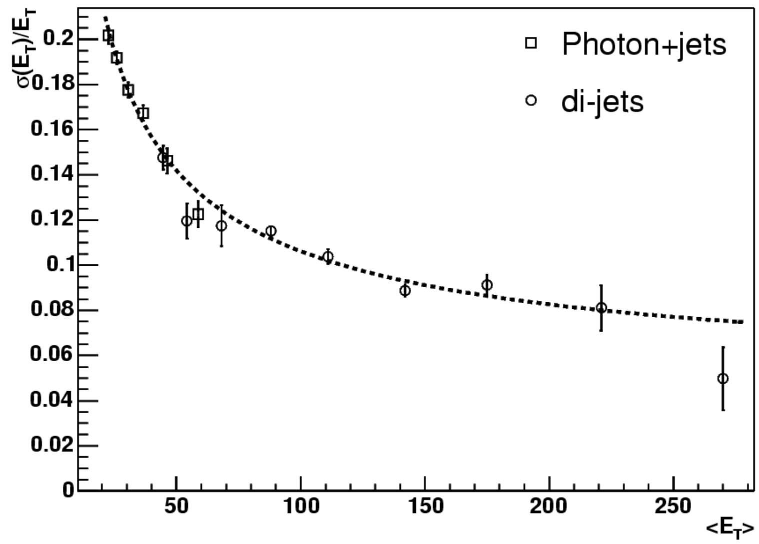

Figure 2.10: Measured hadronic energy resolution of *DØ* calorimeter [18]

2.4 Muon system

DØ muon system includes a central muon system and a forward muon system. Central muon system consists of a toroidal magnet, three layers of proportional drift tubes (PDT), cosmic cap and scintillation counters. Forward muon system has end toroidal magnets, three layers of mini drift tubes (MDT) and three layers of scintillation counters. Central muon system covers up to 1.0 in η_D, forward muon system covers up to about 2.0 in η_D. FIG 2.11 shows the exploded view of wire chambers of the *DØ* muon system.

In the central muon detector, toroidal magnets cover about $|\eta_D| < 1$ region, it provides stand-alone muon momentum measurement. Central drift chambers have three layers, as shown on FIG 2.11. A layer is located inside of the central toroidal magnet, B and C layers are located outside of the magnet. Central drift chambers cover $|\eta_D| < 1$ region. Those drift chambers are made of rectangular extruded aluminum tubes. Cosmic cap and bottom counters are installed on the top, bottom and outside of the central muon drift chambers. Those scintillators are used to determine cosmic ray background by providing information between bunch crossing and muons in the central drift chambers. Aϕ scintillation counters cover the A layer PDTs. Those scintillators reject out-of-time back scatter from the forward direction, and also identify and trigger on the

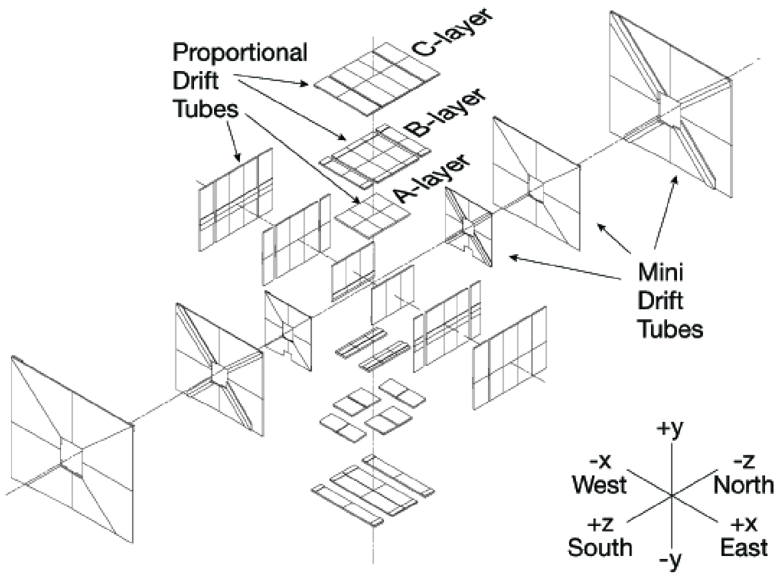

Figure 2.11: Exploded view of $D\O$ muon system wire chambers [17]

muons. MDTS of the forward muon detector are designed to have short electron drift time and a good coordinate resolution. They are used in muon track re-construction. Three layers of trigger scintillation counters provide the good time resolution and amplitude uniformity for background rejection.

2.5 Trigger and data acquisition

$D\O$ trigger system is a three-level trigger system. Each level of trigger exams fewer number of events but in more detail than the lower levels. Data from the detector will have about 1.7 MHz rate. The rate is reduced to about 2 kHz after processed by Level 1 trigger, and is further reduced to 1 kHz at Level 2 trigger. After processed by a more sophisticated software trigger at Level 3, the final trigger rate is reduced to 50 Hz. FIG 2.12 is the block diagram of $D\O$ trigger system.

Level 1 trigger is a hardware trigger system, consists of calorimeter trigger (L1Cal), muon system trigger (L1Muon), and forward proton detector trigger (L1FPD). Decision from the Level 1 trigger must arrive at trigger framework within 3.5 μs for events pipelined at the Level 1 trigger.

Level 2 trigger can accept maximum input rate up to 10kHz, and the maximum accept rate is about 1 kHz. The events at the Level 2 trigger are first processed by detector-specific preprocessing

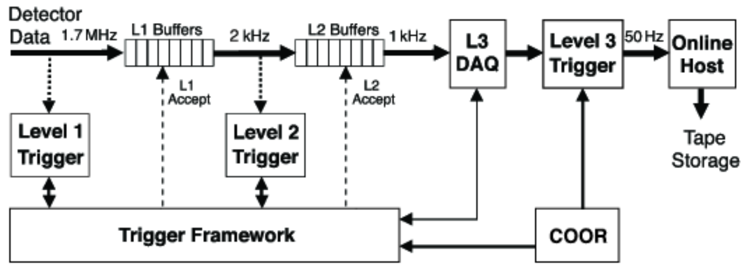

Figure 2.12: Block diagram of $D\emptyset$ trigger systems [17]

engines and then sent to a global stage (L2Global) to determine correlation in physics signature from all detector subsystems.

Level 3 trigger is a software trigger designed to unpack, re-construct, and filter events out from the Level 2 trigger. It provides further reduction of trigger rate-to-tape to 50 Hz. Level 3 trigger decisions are fully based on physics objects and the relationships between those physics objects.

2.6 Luminosity monitor

Luminosity detector has two arrays located at $z = \pm 140$ cm along the beam pipe. Each array has 24 plastic scintillation counters. FIG 2.13 shows the location of luminosity detector. Luminosity detector covers region of $2.7 < |\eta_D| < 4.4$. It also provides z coordination of the vertex of $p\bar{p}$ interaction.

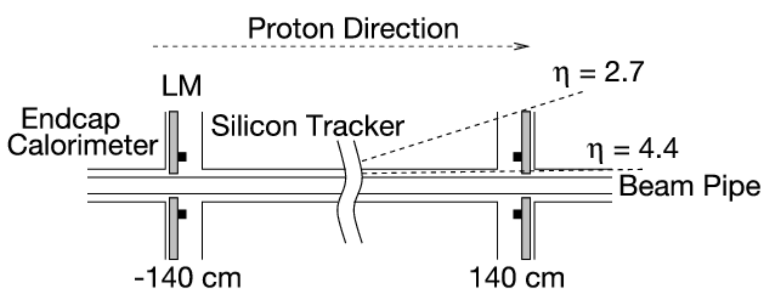

Figure 2.13: Location of luminosity detector [17]

Luminosity calculation is based on equation:

$$\mathcal{L} = \frac{f\bar{N}_{LM}}{\sigma_{LM}} \tag{2.4}$$

where f is the beam crossing frequency, $\bar{N}_{LM}$ is the average number of inelastic collisions per beam crossing, and σ_{LM} is the effective cross section for the luminosity detector. In order to remove the beam halo background, $|z_v|$ needs to be smaller than 100 cm, where $z_v = (t_- - t_+)$, t_- (or t_+) is time of flight measured at particles hit luminosity detector located at $z = 140$ cm (or $z = -140$cm, respectively). Luminosity is measured in unit of luminosity block (LBN). In each LBN, the instantaneous luminosity is stable enough so that we can treat it as linear in the period of each LBN. The total luminosity for this analysis is calculated based on these LBNs.

Barn is the convenient unit for the luminosity, where 1 $barn = 10^{-24} cm^2$, and 1 $pb = 10^{-12}$ *barn*.

Chapter 3

The Events

The data used in this analysis is collected between 2002 to 2004 at $D\emptyset$. The raw data is skimmed to the single electron data to reduce the size. The size of skimmed data is more than one Tera byte. It is further skimmed down to about 100GB for purpose of fast processing. Various selection cuts are applied on data skimming and events selection to reduce the size. This chapter focuses on how the events are selected.

3.1 Electron ID cuts

3.1.1 EM ID, EM fraction and EM isolation

EM ID number is fitted from multiple inputs. $ID = 10$ indicates an electromagnetic particle without track match, $ID = \pm 11$ refers to an electromagnetic particle with track match, where sign represents the charge of the particle.

In this analysis, All particles in CC must have $ID = \pm 11$, and $ID = 10$ in EC to increase signal as well as reduce the background.

EM fraction is defined as the following:

$$f_{em} = \frac{\sum_{towers} E_{EM}}{\sum_{towers}(E_{EM} + E_{Had})} \tag{3.1}$$

where E_{EM} is energy deposited on EM calorimeter, E_{Had} is the energy deposited on hadron calorimeter. Most of electrons and photons deposit at least 90% of cluster energy on EM calorimeter. The requirement of $f_{em} > 90\%$ is used in events selection.

EM isolation is a variable to distinguish electrons from the background events. EM isolation is defined as the following:

	Input variables	H-Matrix 7	H-Matrix 8
1.	EM fraction in EM Cal layer 1	yes	yes
2.	EM fraction in EM Cal layer 2	yes	yes
3.	EM fraction in EM Cal layer 3	yes	yes
4.	EM fraction in EM Cal layer 4	yes	yes
5.	vertex z position and vertex width	yes	yes
6.	$\log_{10}$(Energy)	yes	yes
7.	Area of the cluster at EM third floor (2-D)	yes	yes
8.	Transverse width of shower (1-D)	no	yes

Table 3.1: Input variables of H Matrix 7 and H Matrix 8

$$f_{iso} = \frac{E_{0.4}^{tot} - E_{0.2}^{EM}}{E_{0.2}^{EM}} \tag{3.2}$$

where $E_{0.4}^{tot}$ is the total energy in $\eta \times \phi$ cone with size $R = 0.4$. $E_{0.2}^{EM}$ is the electromagnetic energy in $\eta \times \phi$ cone with size $R = 0.2$. Here $R = \sqrt{\Delta\phi^2 + \Delta\eta^2}$. $f_{iso} < 0.15$ is required in this analysis to separate electrons from other non-isolating particles.

3.1.2 H Matrix

There are two types of H Matrix variables used in this analysis: H Matrix 7 and H Matrix 8. Both two variables compare the shower shape between Monte Carlo simulation and calorimeter cluster. H Matrix 7 has all inputs that H Matrix 8 uses except the transverse width of the shower. Detailed variables inputted to H Matrix determination are listed on Table 3.1.

In order to compare the shapes of shower, we define correlation M_{ij} between two variables x_i and x_j:

$$M_{ij} = \frac{1}{N}(x_i^n - \bar{x}_i)(x_j^n - \bar{x}_j) \tag{3.3}$$

where N is the number of Monte Carlo events, x_i^n is the value of ith variable of nth event. $\bar{x}_i^n$ is the mean value of ith variable of nth event. H Matrix is defined as the following:

$$\chi_{hmx}^2 = \sum_{i,j=1} (x_i^{'} - \bar{x}_i) M_{ij}^{-1} (x_j^{'} - \bar{x}_j) \tag{3.4}$$

H Matrix measures how calorimeter cluster and Monte Carlo simulation match together. It is used to reject backgrounds. In this analysis, all events are required to pass H Matrix 7 < 12 in CC and H Matrix 8 < 20 in EC. More detailed discussion is present in Section 4.5.

3.1.3 Track match

This analysis requires at least one of the electron has track match in EC. In CC, both of the electrons must have track match. The track match refers to spatial match between cluster and track. It is defined in the following way:

$$\chi^2 = (\frac{\Delta z}{\sigma(z)})^2 + (\frac{\Delta \phi}{\sigma(\phi)})^2; \tag{3.5}$$

where Δz and $\Delta \phi$ are differences between track and electromagnetic cluster position in calorimeter. If the track match probability $P(\chi^2) > 0.01$ between the electromagnetic cluster and track, we call this electromagnetic cluster has *track match*.

3.2 Online trigger requirement

Since the data covers wide run range, from run 161973 (at August 2002) to run 196584 (at June 2005). There are various trigger lists applied on data taking at these runs. Different trigger lists may have different Level 1, Level 2 and Level 3 requirements. We can group those trigger lists into four unique groups. Triggers in each unique group share the same trigger requirements. Those groups are: Trigger list version 8 to 10 (run 161973 - 174807). Trigger list version 11 (run 174896 - 177312, 177315 - 177684, 177744 - 178096, and 178104 - 178721). Trigger list version 12 (run 178098 - 178103, 177689 - 177690, 177314, and 178722 - 194597). Trigger list version 13 (run 194567 - 196584).

There are various triggers in each version of trigger list. Only part of triggers in each version are used in this analysis. Table 3.2 shows names of the trigger used in each version.

Triggers listed on Table 3.2 are either prescaled or un-prescaled. But only un-prescaled single EM triggers are used in this analysis. Since DØ trigger efficiency is high enough, only using

Trigger list version 8-11	Trigger list version 12	Trigger list version 13
EM_HI_SH	E1_SHT20	E1_SHT22
EM_HI_2EM5_SH	E2_SHT20	E2_SHT22
EM_HI	E3_SHT20	E3_SHT22
EM_MX_SH	E1_SH30	E1_SH30
EM_MX		

Table 3.2: EM trigger names used in each version of trigger list

un-prescaled single EM triggers would not significantly reduce number of events in this analysis. However, using un-prescaled single EM triggers can simplify the luminosity calculation. For this reason, we only use the following trigger combinations per event, with higher priority on the trigger combinations listed above than those lower ones on the list.

For trigger list version 8 to 11, check triggers:

- If EM_HI_SH and EM_HI_2EM5_SH un-prescaled, otherwise
- If EM_HI_SH un-prescaled, otherwise
- If EM_HI un-prescaled, otherwise
- If EM_MX_SH un-prescaled, otherwise
- If EM_MX un-prescaled

For trigger list version 12, check triggers:

- If E1_SHT20 and E2_SHT20 and E3_SHT20 and E1_SH30 un-prescaled, otherwise
- If E1_SHT20 and E2_SHT20 and E1_SH30 un-prescaled, otherwise
- If E1_SHT20 and E1_SH30 un-prescaled, otherwise
- If E1_SHT20 un-prescaled

For trigger list version 13, check triggers:

- If E1_SHT22 and E2_SHT22 and E3_SHT22 and E1_SH30 un-prescaled, otherwise
- If E1_SHT22 and E2_SHT22 and E1_SH30 un-prescaled, otherwise

Trigger	Level 1	Level 2	Level 3
EM_HI_SH	CEM(1,10)	EM(1,12) for runs > 169523	ELE_LOOSE_SH_T(1,20)
EM_HI_2EM5_SH	CEM(2,5)	EM(1,12) for runs > 169523	ELE_LOOSE_SH_T(1,20)
EM_HI	CEM(1,10)	EM(1,12) for runs > 169523	ELE_LOOSE(1,30)
EM_MX_SH	CEM(1,15)	none	ELE_LOOSE_SH_T(1,20)
EM_MX	CEM(1,15)	none	ELE_LOOSE(1,30)
E1_SHT20	CEM(1,11)	none	ELE_NLV_SHT(1,20)
E2_SHT20	CEM(2,6)	none	ELE_NLV_SHT(1,20)
E3_SHT20	CEM(1,9)CEM(2,3)	none	ELE_NLV_SHT(1,20)
E1_SH30	CEM(1,11)	EM(1,15)	ELE_NLV_SH(1,30)
E1_SHT22	CEM(1,11)	EM(1,15)	ELE_NLV_SHT(1,22)
E2_SHT22	CEM(2,6)	EM(1,15)	ELE_NLV_SHT(1,22)
E3_SHT22	CEM(1,9)CEM(2,3)	EM(1,15)	ELE_NLV_SHT(1,22)
E1_SH30_v13	CEM(1,11)	EM(1,15)	ELE_NLV_SH(1,30)

Table 3.3: Level 1, Level 2 and Level 3 trigger conditions

- If E1_SHT22 and E1_SH30 un-prescaled, otherwise
- If E1_SHT22 un-prescaled

Every event fires any single EM trigger listed on Table 3.2 must pass Level 1, Level 2, and Level 3 conditions. Those conditions are listed on Table 3.3. Table 3.4 is the detailed cuts associated with the respective Level 1, Level 2 and Level 3 conditions listed on Table 3.3.

3.3 Electron kinematic cuts

The Z boson cross section for regions with invariant mass less than 60 GeV is quite small. However, multi-jets background is very large at those low mass regions. The basic strategy to reduce the background events from multi-jets is to apply a minimum P_T cut on electron candidates. But applying a minimum P_T cut on electrons also rejects number of Z bosons by reducing the acceptance. To balance background reduction but still keep high acceptance of Z boson, two electrons candidates in each pair are required to satisfy different P_T cuts: one with $P_T > 15$ GeV, and another must have $P_T > 25$ GeV.

Besides P_T cut on the electrons, there is also an requirement of Z boson invariant mass to be within window of 71 GeV $< M_{ee} <$ 110 GeV.

Level 1 triggers

CEM(1,10)	one EM trigger tower with $E_T > 10GeV$
CEM(1,11)	one EM trigger tower with $E_T > 11GeV$
CEM(1,15)	one EM trigger tower with $E_T > 15GeV$
CEM(2,5)	two EM trigger tower with $E_T > 5GeV$
CEM(2,6)	two EM trigger tower with $E_T > 6GeV$
CEM(1,9)CEM(2,3)	one EM trigger tower with $E_T > 9GeV$, and two with $E_T > 3GeV$
Level 2 triggers	
EM(1,12)	one EM candidate with $E_T > 12GeV$
EM(1,15)	one EM candidate with $E_T > 15GeV$
Level 3 triggers	
ELE_LOOSE_SH_T(1,20)	one electron with $\|\eta_D\| < 3.0$ *and* $E_T > 20$ GeV passing loose requirements including shower shape cuts
ELE_LOOSE(1,30)	one electron with $\|\eta_D\| < 3.0$ *and* $E_T > 20$ GeV passing loose requirements
ELE_NLV_SHT(1,20)	one electron with $\|\eta_D\| < 3.6$ *and* $E_T > 20$ GeV passing tight shower shape cuts
ELE_NLV_SHT(1,22)	one electron with $\|\eta_D\| < 3.6$ *and* $E_T > 22$ GeV passing tight shower shape cuts
ELE_LOOSE_SH_T(1,20)	one electron with $\|\eta_D\| < 3.6$ *and* $E_T > 30$ GeV passing loose shower shape cuts

Table 3.4: Detailed cuts applied on each Level 1, Level 2 and Level 3 conditions

3.4 Detector fiducial cuts

Due to the edge effect of ϕ modular of central EM calorimeter is not well understood and also not well modeled in Monte Carlo simulation. Bias in acceptance determination is found if the events collected by those edge regions are included. Those events has to be removed. In more specific, any events within 15% of central EM calorimeter ϕ modular edge regions are discarded. That is, only events satisfy the following equation are kept:

$$0.15 < mod(\phi_D, 2\pi/32) < 0.85 \tag{3.6}$$

The regions within $1.1 < |\eta_D| < 1.5$ are inter cryostat detectors (ICD) which has no EM layer. Electrons cannot establish EM identification information in ICD regions. Although CC EM calorimeter covers up to 1.2 and EC EM calorimeter starts from 1.4 in η_D, H Matrix information is still not well established near those edges due to calorimeter edge effect. To avoid the above problems, events within $1.1 < |\eta_D| < 1.5$ are not included in analysis. Due to additional unknown problem, $0.9 < |\eta_D| < 1.1$ regions are further cut off. The actual CC region used in analysis is within $|\eta_D| < 0.9$.

The $D\O$ calorimeter covers up to 4.2 in η_D. But far forward electron ID is not well understood. The maximum coverage of electron triggers used in current data is only up to 3.2 in η_D. The events with η_D larger than 3.2 are not included in this analysis too.

In summary, CC events within $|\eta_D| < 0.9$ passed ϕ modular cuts (equation 3.6), and EC events within $1.5 < |\eta_D| < 3.2$ are kept for analysis.

3.5 Data quality cut

The analysis data contains bad events due to hardware problems. Those bad events include bad run, bad LBN, coherent noise and bad calorimeter regions. Bad events may appear in the whole or part of the run. Although all those bad events are removed from the analysis, they are treated in different ways in order to simplify luminosity calculation: Removing events marked under bad run or bad LBN are normalized in luminosity calculation. Coherent noise events removal is treated as one efficiency cut. Removing events within bad calorimeter regions is considered as one of the acceptance cuts.

3.5.1 Bad EM calorimeter regions

Bad EM calorimeter regions are the regions with various kinds of problems at the EM readout towers. Those areas usually have unstable efficiencies during data taking. In the analysis, each of the bad EM calorimeter region is marked individually in η_D, ϕ_D for any run contains bad EM calorimeter regions. A list of the bad EM calorimeter regions is made and all events listed are removed.

3.5.2 Bad runs and bad LBN

Bad run refers to the run that the most events in this run have data quality problem. Bad LBN refers to the most events in this LBN have data quality problem. If the most events in a run are found to be bad, all events in this run are not used. If only fewer events in one run have problem, we only mark the individual LBN that contains bad events as bad LBN. The rest of LBNs in this run are still kept.

List of bad runs used in this analysis are based on study by *DØ* Jet/MET group [19]. List of bad LBNs contains all LBNs that marked with bad CFT, bad SMT or bad CAL from *DØ* run quality database [20].

3.5.3 Data with bad Level 1 EM tower problem

In very rare cases events have Level 1 EM tower problem. When the problem occurs, all or the most of the Level 1 EM towers have the same energy. FIG 3.1 shows the number of Level 1 EM tower with most towers have the same energy versus the run number. The problem is from Level 1 hardware and cannot be fixed at offline data. As a result, any run contain events with Level 1 EM tower problem is removed from analysis, the correspondent integrated luminosity for those runs is also taken into account.

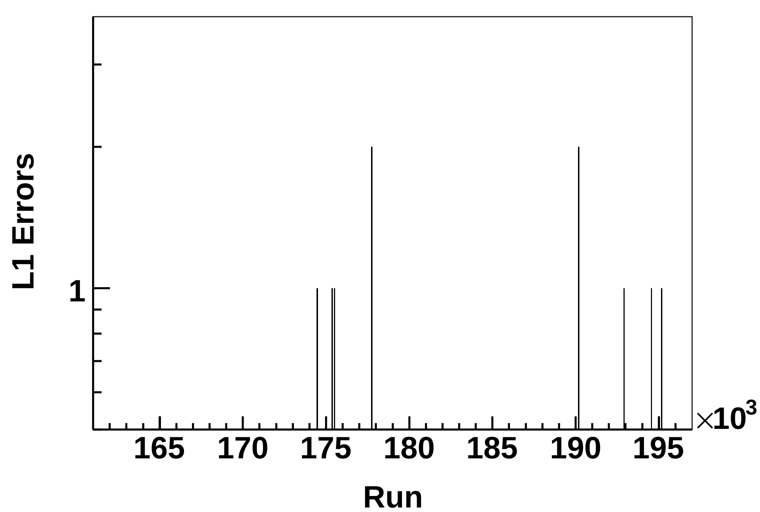

Figure 3.1: Number of L1 EM tower problem in the run versus run number

3.5.4 Coherent noise and ring-of-fire noise

There are two types of noisy events found in the data: coherent noise events and ring-of-fire noise events. Ring-of-fire noise events have been included in current bad LBN list. However, events with coherent noise usually are not marked as bad events and are not included in current bad LBN list. But the coherent noise events can bias efficiency measurement and are thus not used in this analysis. Since the coherent noise events contribute to luminosity, integrated luminosity information have to be corrected after removing the coherent noise events. In order to correct luminosity due to removing of coherent noise events, the coherent noise cut is estimated as part of efficiency that applies on the data selection. The efficiency of removing coherent noise events is estimated by using Zero-Bias data.

Event with coherent noise refers to one has an increased occupancy of an ADC crate. The exact reason of what causes coherent noise is still not well understood. In order to determine which event has coherent noise, we need define the following quantities per ADC after 2.5 *zero suppression*:

ADC occupancy:

$$Occupancy = n/N; \tag{3.7}$$

ADC mean value:

$$\bar{E} = \sum_{i=1}^{N} E_i/N; \tag{3.8}$$

and RMS of ADC:

$$RMS = \sqrt{\frac{\sum_{i=1}^{N}(E_i - \bar{E})^2}{N-1}} \tag{3.9}$$

If one event is found to have at least one ADC with occupancy more or equal to 40%, ADC RMS value is less or equal to 10 ADC counts or at least 2 ADCs with occupancy more or equal to 20%, ADC RMS is less or equal to 5 ADC counts, this event is coherent noise event by definition. Here ADC mean value and RMS are calculated after rejecting 10% of the cells with the highest absolute signal value.

Coherent noise is found to correlate with luminosity and certain trigger combinations. FIG 3.2 shows the ratio of events with coherent noise from Zero-bias and Min-bias data.

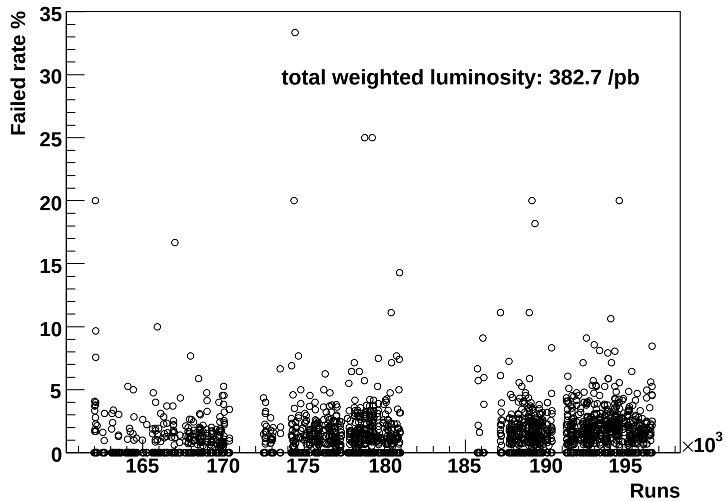

Figure 3.2: Events marked as coherent noise versus run number

It is possible that skimming process on the current data can throw away the LBN that has zero number of electron but no zero luminosity. Removing the events with coherent noise could change the integrated luminosity. In order to correct integrated luminosity due to removing the coherent noise events, a weight is applied to luminosity per run, where the weight is determined by the following equation:

$$W = \frac{n}{N} \tag{3.10}$$

where N is the number of total events and n is the number of events without coherent noise per run. The corrected luminosity after removing events with coherent noise is:

$$\mathscr{L}_{corr} = \sum_{run} W_{run} \mathscr{L}_{run} \tag{3.11}$$

Total integrated luminosity for data in this analysis is 388.6 pb^{-1}, after removing the events with coherent noise, the corrected luminosity is 382.7 pb^{-1}.

3.6 Luminosity

3.6.1 Method

Integrated luminosity calculation should take the bad events removed from analysis into account. These events include the events listed on the list of bad runs and bad LBNs. Due to the limit of the Level 1 trigger rates, not all EM triggers are un-prescaled during data taking. ORing the instantaneous luminosity is necessary if data is collected with prescaled Level 1 triggers. Otherwise, the same luminosity blocks will be counted more than once. Because trigger efficiency is generally high. Basically more than 95% of events can pass the un-prescaled Level 1 triggers. ORing method is not necessary in this analysis. As a result, only the un-prescaled Level 1 triggers is used.

3.6.2 Luminosity quality cuts and trigger rules

To ensure a good luminosity quality, status of all detectors during data taking is required in either *GOOD* or *REASONABLE* status, except CTT, and MUON. Quality of CTT and MUON can not affect this analysis. In addition to the above requirements, if the most of the events are found bad in a run, the whole run is marked as bad run. If only few events are found bad in certain LBN, only this LBN is marked as bad LBN and removed. After removing bad events, the correspondent instantaneous luminosity is also subtracted.

Ring-of-fire events and events have been marked as empty crate are also removed from luminosity calculation based on the discussion in section 3.5.4.

The same trigger rules are used to calculate integrated luminosity. They are described in Section 3.2.

3.6.3 Integrated luminosity of the data

The total integrated luminosity for the data in this analysis is 388.5 pb^{-1}, before removing coherent noise events.

3.7 Vertex correction and cuts

The direction of electron is determined in the following way: If electron has track match, the direction of electron is obtained from the direction of track. If electron has no track match, the calculation of η and ϕ is based on the primary vertex position and electron's calorimeter cluster position. The primary vertex is determined by the highest $\sum logp_T^{Trk}$ in a two-pass algorithm, where it first calculates the vertices with a loose selection and then uses the found vertex position and errors to do track selection and vertex fitting. It is fitted with multiple tracks, include the tracks from the background events. If the electron has no track match, and the background track and electron are not originated from the same vertex, η and ϕ calculation is biased. FIG 3.3 shows distance along z axis between the primary vertex and the vertex of electron track. Although most primary vertices fall within 3 cm in distance away from track vertices, there are about 1.8% primary vertices are found that their positions are 3 cm or more away from the respective track vertices. Using the primary vertex position to determine the direction of electron without track match cannot always give the accurate η and ϕ.

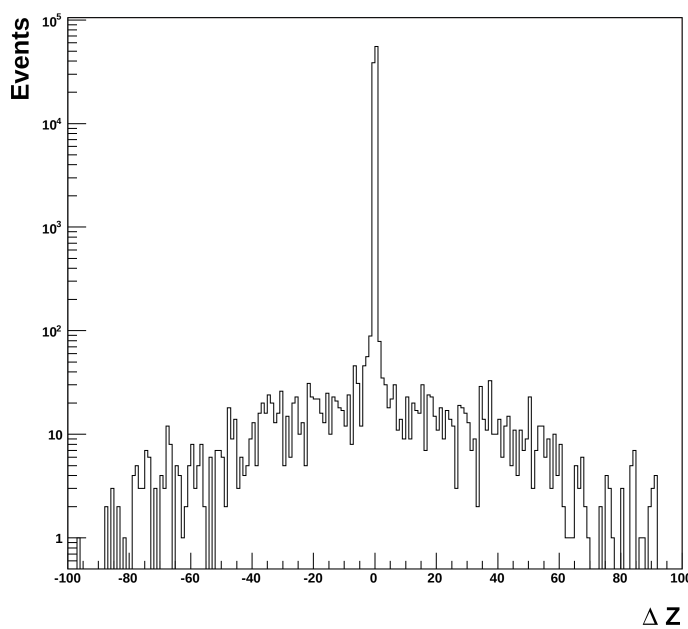

Figure 3.3: Distance between the primary vertex and track vertex along z axis

This analysis requires at least one of the electrons in each pair has track match. That means, at least one electron will have η and ϕ from the matched track. If another electron has no matched track, instead of using primary vertex, we can use vertex of electron with track match to determine the direction of electron without track match. This process is called *re-vertexing* in this thesis.

3.7.1 Determine η and ϕ

To illustrate curvature of an electron track in 2T magnetic field of $D\O$ central tracker, we define track direction parameter α:

$$\begin{aligned} \alpha &= \phi - \phi^0 \\ &= arcsin(k\frac{q}{P_T}r) \end{aligned} \tag{3.12}$$

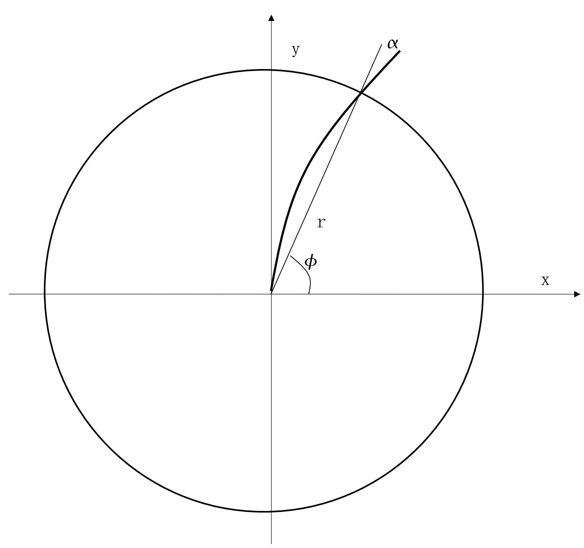

Figure 3.4: Definition of α in x-y plane

where $\phi = atan(y/x)$ is the track direction at radius r, ϕ^0 is the direction of track at beam line. $k = 0.003$ for $D\O$ tracker. FIG 3.4 shows α in a x-y plane. Considering charge of electron is -1, and maximum radius of $D\O$ tracker is about $r = 75$ cm, when $P_T = 15$ GeV, $\alpha = 0.86^o$, when P_T $= 10$ GeV, $\alpha = 1.29^o$. $\alpha < 0.5^o$ if $P_T > 15$. In general, the curvature of high P_T electron track is very small and can be ignored.

Define electron cluster position at the third floor of EM layer: ($x_{Cal3f}, y_{Cal3f}, z_{Cal3f}$). If the true vertex position is $(x_{vxt}, y_{vxt}, z_{vxt})$, and the electron P_T is high enough ($P_T > 10GeV$) so that curvature of track can be ignored. Define:

$$\Delta x = x_{Cal3f} - x_{vxt},$$

$$\Delta y = y_{Cal3f} - y_{vxt},$$

$$\Delta z = z_{Cal3f} - z_{vxt}, \tag{3.13}$$

Using vertex and cluster position at the third floor of EM layer, we can get:

$$\eta_{new} = \frac{1}{2} log(\frac{\sqrt{\Delta x^2 + \Delta y^2 + \Delta z^2} + \Delta z}{\sqrt{\Delta x^2 + \Delta y^2 + \Delta z^2} - \Delta z}); \tag{3.14}$$

and:

$$\phi_{new} = arctan\frac{\Delta y}{\Delta x}; \tag{3.15}$$

Momentum and transverse momentum are calculated using η_{new}, ϕ_{new} and EM energy deposits on calorimeter E.

3.7.2 Vertex distributions

There are three types of vertices based on different method used:

- A primary vertex is fitted from multiple tracks of one event, including the background tracks. Since background tracks are also included in the fitting, we can get primary vertex even if the electron under study has no track match.

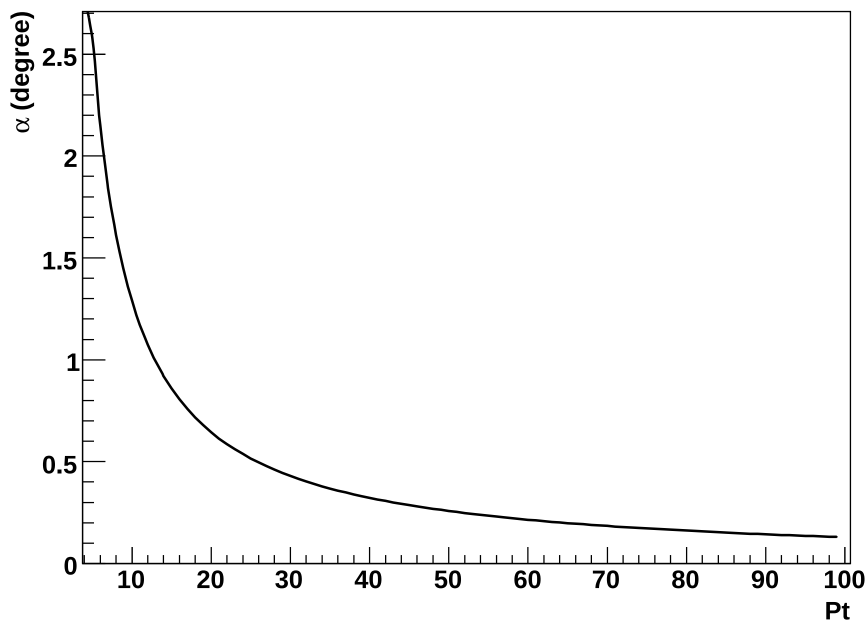

Figure 3.5: α value as function of electron P_T at $r = 75$ cm

- A track vertex is vertex fitted from the track of an electron under study. Because it is a one-track fitting, position resolution along z axis is worse than those fitted with multiple tracks.

- A primary vertex attached to the electron track is primary vertex fitted from this electron track together with other tracks. It represents the actual electron vertex position and has better position resolution.

All events under vertex study must pass the same cuts used in events selection. FIG 3.6 is distribution of z_{vtx} of primary vertex after cuts. All events pass cuts have valid primary vertex. The width of the primary vertex distribution is 22.6 ± 0.1 cm.

By definition, the track vertex or primary vertex attached to electron track must have at least two SMT hits to have a valid vertex. Since primary vertex attached to electron track is vertex fitted from multi-track. It has better the shape and narrower width. In this analysis, the width of primary vertex attached to electron track is 19.1 ± 0.06 cm. The width of track vertex is 19.2 ± 0.06 cm.

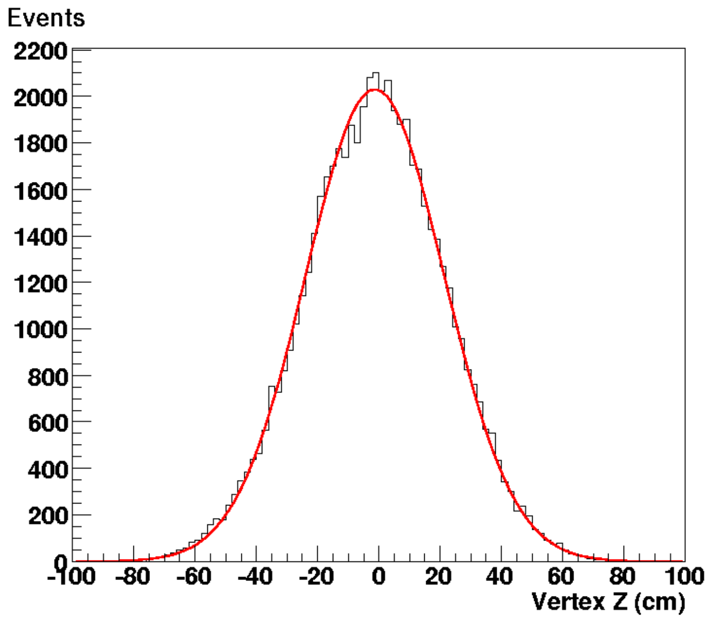

Figure 3.6: Distribution of primary vertex position along z axis. The width of this distribution is 22.6 cm

3.7.3 Re-vertexing algorithm

The re-vertexing algorithm applies to the events with at least one electron has track match:

- If both of two electrons have track match, no correction is made.
- If only one electron has track match, and with more than two SMT hits. The attached primary vertex is used to correct the vertex position of electron without track match.
- If only one electron has track, but SMT hits is less than two. We cannot find event vertex associated with the electron. Primary vertex with the shortest distance to the electron along z axis is used in the re-vertexing.

For the third case, we can define d_i, the distance along z axis between i-th primary vertex to the nearby electron:

$$d_i = z_{trk} + z^0_{pvtx} - z^i_{pvtx} \tag{3.16}$$

Two tracks case	One track case	
All types of SMT hits	SMT hits ≥ 2	SMT hits < 2
19911 ± 14 (829 ± 29 events have no SMT hits)	6651 ± 87	1527 ± 52

Table 3.5: Number of events in each configuration with re-vertexing

where z_{trk} is z position of electron track, z_{pvtx} is z position of attached primary vertex. i is the index of matched primary vertex which gives the minimum value of d_i. By using this method, we can find the most of matched vertices with the shortest distance are the primary vertex with distance less than 3 cm (FIG 3.7).

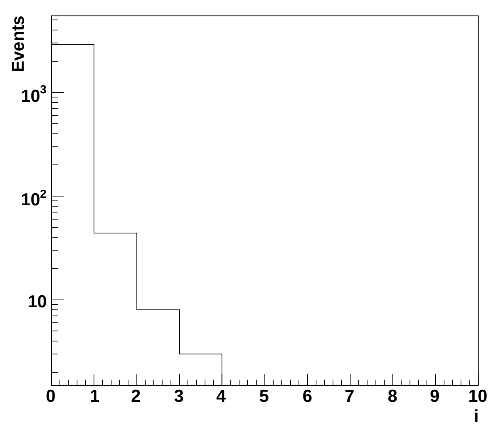

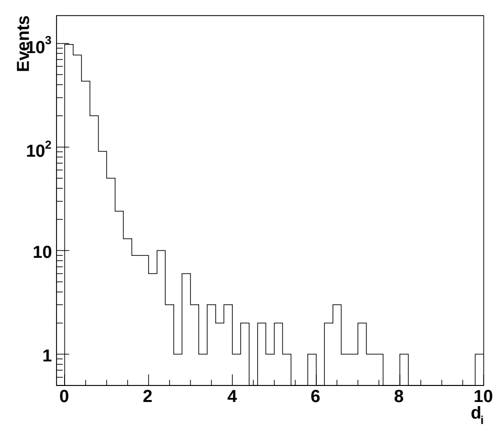

Figure 3.7: Match primary vertex index (left plot, $i = 0$ means primary vertex) and distance between primary vertex and electron track vertex along z axis (right plot)

About 15 thousand electron vertices are corrected with re-vertexing method. Number of events in each configuration are shown on Table 3.5.

Re-vertexing gives the best vertex z position for efficiency measurement. The new vertex is based on the following method:

- If both electrons do not have the matched track, primary vertex of event is used;
- If only one of two electrons has matched track, and the matched track has two or more SMT hits, the primary vertex attached to this track is used;
- If only one of two electrons has matched track, but SMT hits less than two, the primary vertex with the closest distance along z axis to the track is used;

- If both electrons have tracks, each of track has at least two SMT hits, the primary vertex attached to the track with the best χ^2 is used;
- If both of electrons have matched tracks, but only one track with two or more SMT hits, the primary vertex attached to the track with more than two SMT hits is used;
- If both of electrons have tracks, but none track has two or more SMT hits, the primary vertex is used in this case.

3.7.4 Discussions

Background ratio for Z events with only one matched track and number of SMT hits less than 2 is significantly larger than the background of the rest configurations (FIG 3.9). Distribution of primary vertex z of the above events is plotted on FIG 3.8. We can find two dips around $\pm$ 40 cm on the distribution. These dips are due to the end of the SMT barrel section.

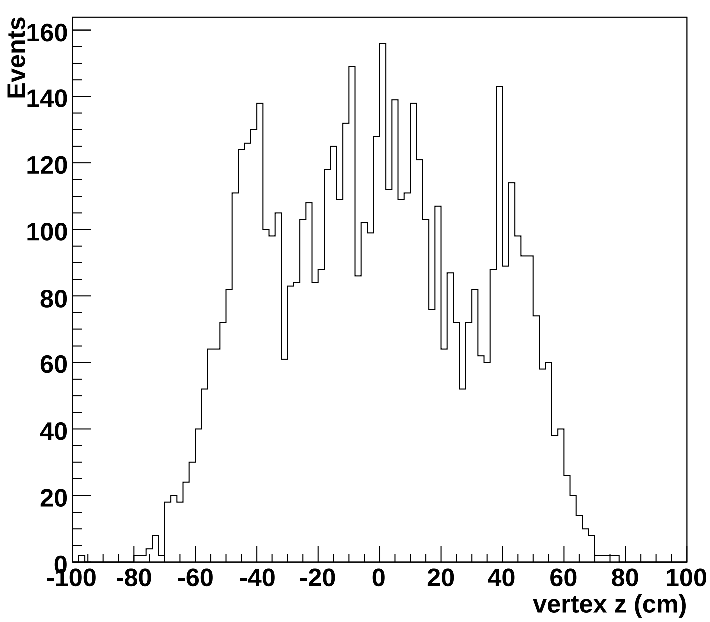

Figure 3.8: Vertex z distribution of events with one track matching and number of SMT hits less than 2

If the above events are separated into two categories: one with $|z| > 40$ cm and another with $|z| < 40$ cm. We can find events with $|z| > 40$ cm have higher signal to background ratio,

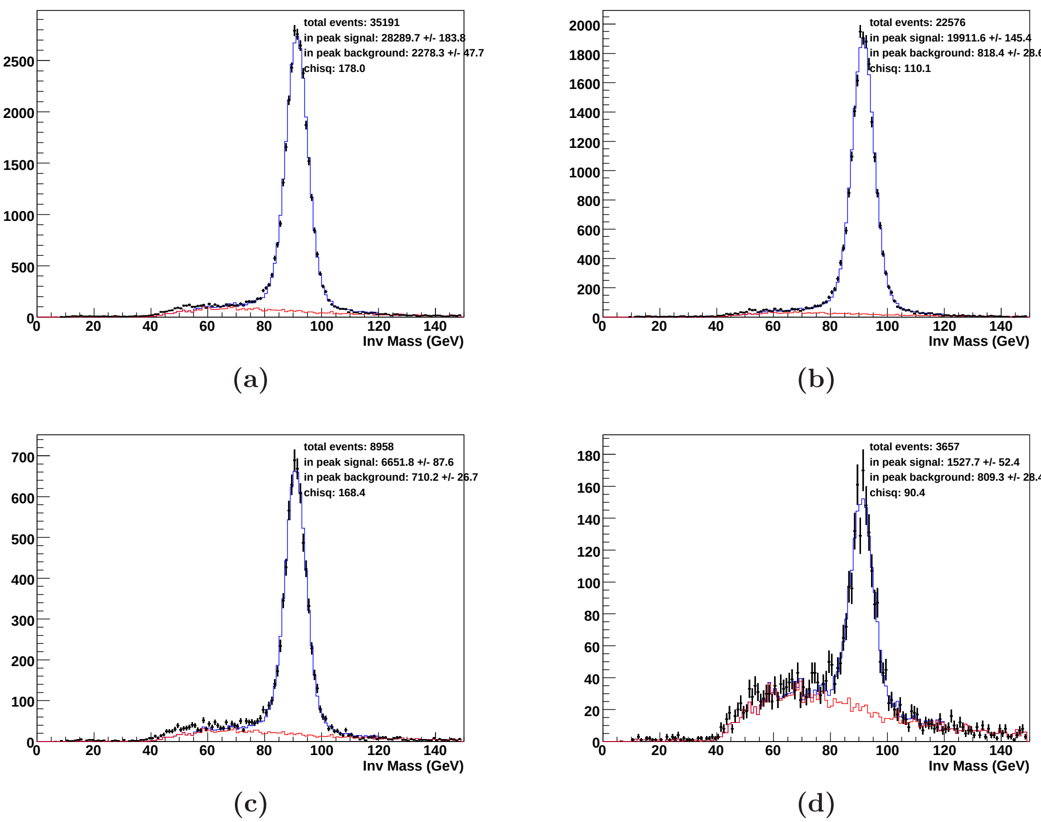

Figure 3.9: Z boson invariant mass plots: (a) invariant mass plot of all events that have at least one track (b) invariant mass plot of events with two tracks. (c) invariant mass plot of the events with only one track, and each track has number of SMT hits ≥ 2 (d) invariant mass plot of events that has only one track, and each track has number of SMT hits less than 2

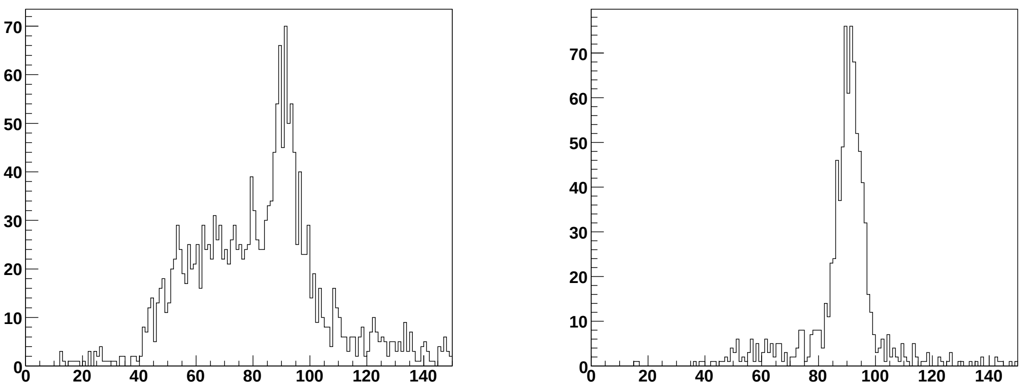

when $|z| < 40$ cm　　　　when $|z| > 40$ cm

Figure 3.10: Z boson invariant mass plot of the events with one track and number of SMT hits less than 2

however, events with $|z| < 40$ cm shows relative large amount of background (FIG 3.10). This is mainly due to inefficiency of the SMT detector when $|z| < 40$ cm.

Since the most events with only one track, SMT hits less than two, and $|z| < 40$ cm are the backgrounds. When $|z| > 40$, number of events is about 900. Those numbers are negligible compare to the total number of events in this analysis. To simplify the analysis, events with only one matched track and number of SMT hits less than two are removed from analysis to clean large amount of background events due to inefficiency of the SMT detector.

Re-vertexing correction to electron η and ϕ is small. Averaged correction rate is less than 3% (FIG 3.11).

It can be concluded that re-vertexing corrects bias due to using primary vertex for the electrons without track match. Because of the big difference in signal to background ratio for the electrons with only one track matching but SMT hits less than two, those events are not used in this analysis.

3.8 Summary

In summary, events are required to pass the following *standard* cuts:

- EM ID = 10, or $\pm$ 11 in EC, and EM ID = ± 11 in CC;

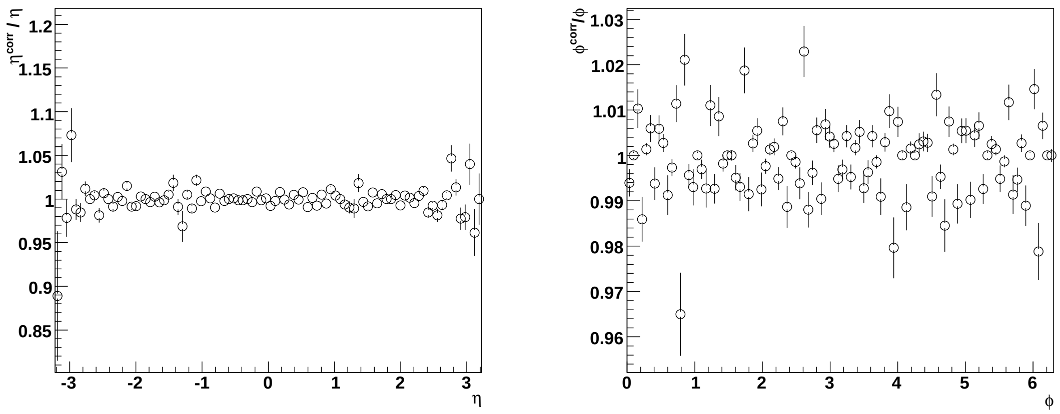

Figure 3.11: Correction rate to electron η (left plot) and ϕ (right plot) due to re-vertexing

- $f_{iso} < 0.15$ and $f_{em} > 0.9$;
- H Matrix $7 < 12$ in CC and H Matrix $8 < 20$ in EC;
- $P_T > 15$ GeV for one electron, $P_T > 25$ GeV for another electron;
- At least one electron has track match;
- At least one electron passes un-prescaled trigger combinations;
- Pass ϕ_{mod} cut;
- Pass various data quality cuts;
- If the electron pair has only one track match, number of SMT hit must greater than two.

There are more specific cuts applied on events selection in efficiency measurement. Detail of those cuts are discussed in Chapter 4.

Rapidity of Z boson is determined by E and p_z of electrons using the following equation:

$$y = \frac{1}{2} ln(\frac{E^{e1} + p_z^{e1} + E^{e2} + p_z^{e2}}{E^{e1} - p_z^{e1} + E^{e2} - p_z^{e2}}) \tag{3.17}$$

Number of events passed selection cuts per rapidity y bin is listed on Table 3.8.

Table 3.6: Events passed selection cuts per rapidity bin of Z boson

y bin	Total events	y bin	Total events
-2.95	0.00	0.05	486.00
-2.85	0.00	0.15	462.00
-2.75	3.00	0.25	468.00
-2.65	14.00	0.35	410.00
-2.55	24.00	0.45	469.00
-2.45	64.00	0.55	433.00
-2.35	92.00	0.65	471.00
-2.25	136.00	0.75	484.00
-2.15	187.00	0.85	491.00
-2.05	227.00	0.95	530.00
-1.95	208.00	1.05	624.00
-1.85	251.00	1.15	595.00
-1.75	308.00	1.25	581.00
-1.65	275.00	1.35	534.00
-1.55	318.00	1.45	445.00
-1.45	350.00	1.55	376.00
-1.35	431.00	1.65	369.00
-1.25	480.00	1.75	383.00
-1.15	515.00	1.85	366.00
-1.05	474.00	1.95	352.00
-0.95	460.00	2.05	325.00
-0.85	405.00	2.15	272.00
-0.75	485.00	2.25	217.00
-0.65	411.00	2.35	140.00
-0.55	437.00	2.45	98.00
-0.45	431.00	2.55	37.00
-0.35	469.00	2.65	21.00
-0.25	456.00	2.75	7.00
-0.15	501.00	2.85	0.00
-0.05	475.00	2.95	0.00

Chapter 4

Electron Efficiencies

In this chapter, the author present the measurement of the electron cut efficiencies: pre-selection efficiency, trigger efficiency, H Matrix efficiency, and track match efficiency. Systematic and statistical uncertainties for each efficiency are also discussed.

4.1 Method

If there are total N electrons under test, n out of N electrons pass the test cut. The efficiency of the test cut is defined as:

$$\varepsilon = \frac{n}{N} \tag{4.1}$$

If the probability distribution of number of passed or failed events follows binomial distribution:

$$P(n|N, \varepsilon) = \frac{N!}{n!(N-n)!}\varepsilon^n (1-\varepsilon)^{N-n} \tag{4.2}$$

Uncertainty of this measurement is:

$$\sigma_\varepsilon = \sqrt{\frac{\varepsilon(1-\varepsilon)}{N}} \tag{4.3}$$

If the number of events pass the test n is larger enough but not close to the total number N, *Gaussian* distribution is good enough to describe the distribution. However, when n is close to zero or the total number N, *Poisson* distribution is more appropriate to describe the distribution. For example, in electron pre-selection efficiency measurement, number of failed same sign and opposite sign pairs are very small. In this case, the distribution is the *Poisson* distribution.

The *Tag-and-Probe* method is the method to determine electron selection efficiency based

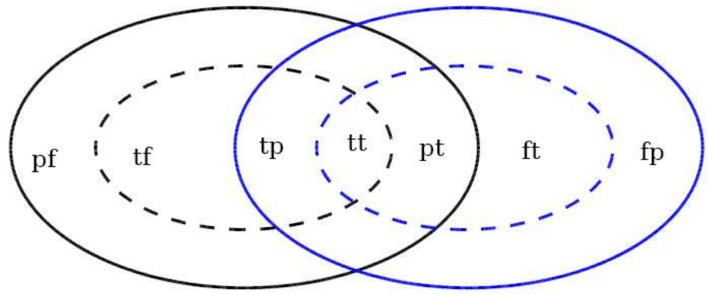

Figure 4.1: Tag-and-probe method: $Vinne$ diagram

on pair of Z electrons. In the *Tag-and-Probe* method, define:

- tag (t) : particle passes all tight electron cuts;
- probe (p) : particle passes loose electron ID cuts and also passes the cut under efficiency measurement;
- fail (f) : particle passes loose electron ID cuts but also fails the cut under efficiency measurement.

The loose cuts normally include EM ID, EM fraction and EM isolation cuts. The tight cuts normally include the loose cuts and track match cut to ensure *tag* is a good electron. FIG 4.1 is *Vinne* diagram of electron pairs with combination of pass or fail.

For the left part of *Vinne* diagram on FIG 4.1, the total number of electrons pass cuts are $N_{tt} + N_{tp}$ out of total number of electrons under test $N_{tt} + N_{tp} + N_{tf}$. Similarly, total number of electrons passing cuts on right side of the *Vinne* diagram is $N_{tt} + N_{pt}$ out of $N_{tt} + N_{pt} + N_{ft}$. Considering $tp = pt$, and $ft = tf$, using equation 4.1, the efficiency of the cut under testing is:

$$\varepsilon = \frac{2N_{tt} + N_{tp}}{2N_{tt} + N_{tp} + N_{tf}} \tag{4.4}$$

The above method to determine cut efficiency is also called *Tag-and-Probe* method in this dissertation.

4.2 Background fitting method

Most of the background events in this analysis come from multi-jet events with two jets pass the selection cuts or from W+jet events where the jet is misidentified as an electron. Background in efficiency study is fitted and removed in bin-by-bin base using multi-jet background shape obtained from the data (or the exponential curve) and the invariant mass peak from Monte Carlo simulation. The multi-jet background shape and invariant mass peak from the Monte Carlo simulation are scaled and added together to fit the invariant mass distribution. A one parameter fitting is used to determine relative contributions from the signal and the background. There are two variables used in the fitting: amplitudes applied to the signal and the background histograms. But those two variables are constrained by the total number of events in the fitting. Once the parameter is determined, the background in each bin is subtracted from the invariant mass distribution plot.

When statistics in a bin is low, using a *goodness-of-fit* based on *Gaussian* distribution fails because the distribution tends to follow *Poisson* distribution. For this reason, the log likelihood ratio of *Poisson* distribution in equation 4.5 is used to evaluate *goodness-of-fit*:

$$-2ln\lambda = 2\sum_i [N_i^{th} - N_i^{obs} + N_i^{obs} ln(\frac{N_i^{obs}}{N_i^{th}})] \tag{4.5}$$

In equation 4.5 N_i^{th} and N_i^{obs} are number of the Monte Carlo and data events at the ith invariant mass bin, respectively.

The background shapes used in fitting are from the events pass the most of the selection cuts described in Chapter 3, but without applying track match requirement and the H Matrix value for each EM object is inverted to H-Matrix 8 greater than 35. Signal shapes are obtained from $Z/\gamma^* \to ee$ Monte Carlo simulation. The Monte Carlo events are generated with $ResBos$ [21] and with QED final state radiation correction from $PHOTOS$ [22]. Detector effects, efficiencies and acceptance cuts are applied by $PMCS$. To investigate the correlation between H Matrix cut and other cuts, an exponential curve is also used as background shape.

4.3 Pre-Selection Efficiency

4.3.1 Method

Pre-selection efficiency is the efficiency of electrons pass the following pre-selection cuts:

- ID = 10, ±11 in EC and ID = ± 11 in CC;
- $f_{iso} < 0.15$;
- $f_{em} > 0.9$.

When applying *tag-and-probe* method to determine pre-selection efficiency, tag needs to be an electron and probe is a track back-to-back to the tag electron. The pre-selection efficiency is determined by counting how many probe tracks pass pre-selection cuts listed above:

$$\varepsilon_{presel} = \frac{N^{pass}}{N^{tot}} \tag{4.6}$$

where N^{pass} is the number of tracks pass pre-selection cuts listed above. N^{tot} is the total number of tracks under test. Tag electron and probe track must originate from the same vertex.

4.3.1.1 Selection cuts

In pre-selection efficiency measurement, *Tag-and-probe* are electron and a back to back track. The tag and probe are required to pass various selection cuts. In specific, tag electron is an electron passes the tight selection cuts listed below:

- $P_T > 25$ GeV;
- EM ID = 10, ± 11;
- $f_{em} > 0.9$;
- $f_{iso} < 0.15$;
- H Matrix 7 < 12 (in CC), and H Matrix 8 < 20 (in EC);

- Has matched spatial track;
- $P_T^{Trk}/\sigma_{P_T}^{Trk} > 1$;
- Has at least two SMT hits on the matched track;
- $|\eta_D| < 1.1$ in CC and $1.5 < |\eta_D| < 2.0$ in EC;
- No electron in bad calorimeter regions.

The probe electron is an electronic track back-to-back to the tag electron with the following identities:

- back to back in ϕ to the tag electron;
- $P_T^{Trk} > 12$ GeV;
- $\chi^2_{Trk} < 0.8$;
- $|dca^{Trk}| < 1.0$ cm[1];
- ΔR between muon track and electron track is greater than 0.2;
- $0.6 < \phi_{mod}^{Trk} < 0.9$ in CC;
- The total $P_T^{Trk} < 3$ GeV in 0.4 cone around electronic track;
- The electron track has at least two SMT hits;
- $|\eta_D| < 1.1$ in CC and $1.5 < |\eta_D| < 3.2$ in EC;
- Not in bad calorimeter regions.

Invariant mass of electron-track pairs must larger than 65 GeV to reduce the multi-jet background. The distance between the electron vertex and the track vertex along z axis should less than 2 cm to ensure those two are originated from the same Z boson.

Events selection in pre-selection efficiency measurement requires opening angle between track and electron to be greater than 2 in ϕ to ensure electron and track pair is from Z boson

[1]dca refers to the distance of the point of closest approach from the primary vertex in the transverse plane

in geometry. However, the opening angle between the electron and track might not always be back-to-back in ϕ due to no zero momentum the Z boson carries. By requiring back-to-back in ϕ actually removes part of Z bosons from pre-selection efficiency measurement. Monte Carlo simulation is used to verify possible bias due to the back-to-back requirement and indicates this effect is negligible.

4.3.1.2 Determine pre-selection efficiency

Define the following electron pairs when using *Tag-and-probe* method in pre-efficiency measurement:

- P_S^{SS}: Number of electron pairs have the same sign and probe ones pass the cuts,
- P_S^{OS}: Number of electron pairs have the opposite sign and probe ones pass the cuts,
- F_S^{SS}: Number of electron pairs have the same sign and probe ones fail the cuts,
- F_S^{OS}: Number of electron pairs have the opposite sign and probe ones fail the cuts,

Since the charge of electron is not always identified correctly. Let M_p (M_t) be charge mis-identification rate of probe electrons (tag tracks). Due to the charge mis-identification, electron pairs with opposite sign of charge pass the the pre-selection cuts have the following combinations:

- Signal pair with opposite sign of charge, passes the cuts and with both charges identified correctly;
- Signal pair with opposite sign of charge, passes the cuts but with both charges mis-identified;
- Background pair with opposite sign of charge, passes the cuts and with both charges identified correctly;
- Background pair with opposite sign of charge, passes the cuts but with both charges mis-identified;

- Background pair with same sign of charge passes the cuts but either back-to-back track or electron charge mis-identified.

The above combinations have the following relation:

$$
\begin{aligned}
N^{os}_{pass} &= P^{os}_{s}(1-M_t)(1-M_p) + P^{os}_{s}M_tM_p + P^{os}_{bg}(1-M_t)(1-M_p) + P^{os}_{bg}M_tM_p + \\
&\quad P^{ss}_{bg}\{M_t(1-M_p) + M_p(1-M_t)\}
\end{aligned}
$$

Using the same approach, we can find the expressions of number of pairs N^{ss}_{pass} (N^{os}_{fail}) with the same (opposite) sign of charge pass (fail) the cuts, or number pairs N^{ss}_{fail} with the same sign of charge also fail the cuts:

$$
\begin{aligned}
N^{ss}_{pass} &= P^{ss}_{bg}(1-M_t)(1-M_p) + P^{ss}_{bg}M_tM_p + P^{os}_{bg}\{M_t(1-M_p) + M_p(1-M_T)\} + \\
&\quad P^{os}_{s}\{M_t(1-M_p) + M_p(1-M_t)\},
\end{aligned}
$$

$$
\begin{aligned}
N^{os}_{fail} &= F^{os}_{s}(1-M_t)(1-M_p) + F^{os}_{s}M_tM_p + F^{os}_{bg}(1-M_t)(1-M_p) + F^{os}_{bg}M_tM_p + \\
&\quad F^{ss}_{bg}\{M_t(1-M_p) + M_p(1-M_t)\},
\end{aligned}
$$

$$
\begin{aligned}
N^{ss}_{fail} &= F^{ss}_{bg}(1-M_t)(1-M_p) + F^{ss}_{bg}M_tM_p + F^{os}_{bg}\{M_t(1-M_p) + M_p(1-M_T)\} + \\
&\quad F^{os}_{s}\{M_t(1-M_p) + M_p(1-M_t)\}.
\end{aligned}
$$

With simple calculation, we have:

$$
\begin{aligned}
N^{os}_{pass} + N^{ss}_{pass} &= (P^{ss}_{bg} + P^{os}_{bg})(1 - M_t)(1 - M_p) + (P^{ss}_{bg} + P^{os}_{bg})M_t M_p + (P^{os}_{bg} + P^{ss}_{bg})\{M_t(1 - M_p) \\
&\quad + M_p(1 - M_T)\} + (P^{os}_s + P^{ss}_s)\{M_t(1 - M_p) + M_p(1 - M_t)\} \\
&= P^{ss}_{bg} + P^{os}_{bg} + P^{os}_s;
\end{aligned}
$$

and

$$
\begin{aligned}
N^{os}_{fail} - N^{ss}_{fail} &= F^{os}_s\{(1 - M_t)(1 - M_p) + M_t M_p - \{M_t(1 - M_p) + M_p(1 - M_t)\}\} \\
&+ F^{os}_{bg}\{(1 - M_t)(1 - M_p) + M_t M_p - \{M_t(1 - M_p) + M_p(1 - M_T)\}\} \\
&+ F^{ss}_{bg}\{\{M_t(1 - M_p) + M_p(1 - M_t)\} - (1 - M_t)(1 - M_p) - M_t M_p\} \\
&= [F^{os}_s + F^{os}_{bg} - F^{ss}_{bg}][(1 - 2M_t)(1 - 2M_p)];
\end{aligned}
$$

Since correct identified electron pairs carry opposite charges. The main background source in this analysis is the mis-identified jet. The mis-identified jet events carry the same sign charges. Consider the mis-identified charge, we have:

$$
F^{os}_s = \frac{N^{os}_{fail} - N^{ss}_{fail}}{(1 - 2M_t)(1 - 2M_p)} \tag{4.7}
$$

$$
P^{os}_s = N^{os}_{pass} + N^{ss}_{pass} - 2P_{bg}. \tag{4.8}
$$

Under similar assumption, pre-selection efficiency is:

$$
\varepsilon_{presel} = \frac{N^{os}_{pass} + N^{ss}_{pass} - 2P_{bg}}{N^{os}_{pass} + N^{ss}_{pass} - 2P_{bg} + \frac{N^{os}_{fail} - N^{ss}_{fail}}{(1-2M_t)(1-2M_p)}} \tag{4.9}
$$

4.3.1.3 Determine charge mis-identification rate

Charge of electron is determined by curvature of track matched to this electron. The charge mis-identification mainly comes from two sources. One is due to matched track has high transverse momentum which looks like a *straight* track. This effect can be illustrated using equation 3.12. When P_T is larger, value of q/P_T is getting smaller and the track looks more straight and the charge of electron is harder to judge based on the curvature of the track.

Another source of the charge mis-identification is from multiple scattering and soft radiation during charged particles flying through $D\O$ tracking system. This type of charge mis-identification is related to which part of tracking system that the electron passing through.

Charge mis-identification rate is a ratio of number of electron pairs with the same sign charge out of total number of electron pairs. Both electrons must have matched spatial tracks:

$$\varepsilon_{charge\ misID} = \frac{N^{same\ sign}}{N^{total}} \tag{4.10}$$

Since all electron pairs in pre-selection efficiency measurement are required to have track match, background contamination rate is low and can be neglected. Charge mis-identification measurement and pre-selection measurement use the same sample to ensure consistency.

Cuts on tag and probe electrons in charge mis-identification measurement are similar to those used in pre-selection efficiency measurement, except the cuts on electron identification is little loose and have additional track requirements: Minimum P_T of electron is 15 GeV instead of 25 GeV. η_D coverage in EC is extended to 3.2. *dca* of track is less than 1.0. Track P_T is larger than 12 GeV. χ^2 of track is less than 8.0, and total track P_T around 0.4 cone of probe track is less than 3 GeV. But track P_T/σ_{P_T} cut is not required.

Charge mis-identification results are showed in the following figures: Fig 4.2 shows the measured charge mis-identification rate as function of η_D. Fig 4.3 shows the measured charge mis-identification rate as function of electron P_T. Fig 4.4 shows the measured charge mis-identification rate as function of ϕ_D. Fig 4.4 shows the measured charge mis-identification rate as a function of

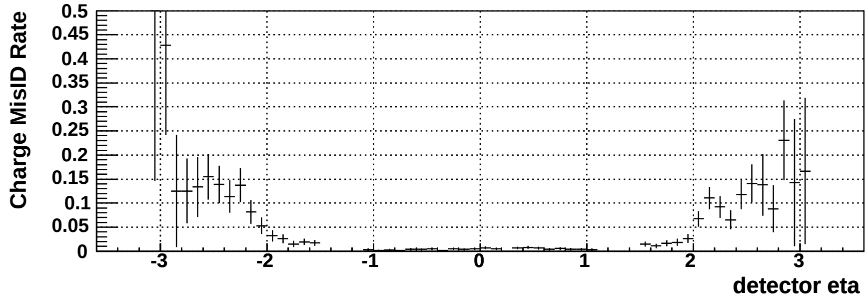

Figure 4.2: Charge mis-identification rate as a function of η_D

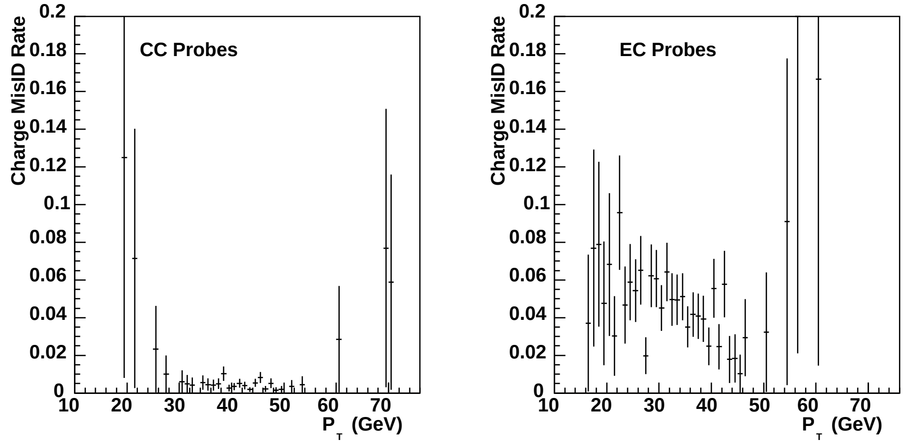

Figure 4.3: Charge mis-identification rate as a function of P_T

run number.

4.3.2 Results

Pre-selection efficiency is not only an η_D dependable variable. It is also correlated to P_T of probe electron. When studying P_T dependable pre-selection efficiency, we use electron P_T if the track has a matched electron. Otherwise, the calorimeter cluster energy within 0.5 cone in radius is used. This configuration reduces *bremsstrahlung* radiation loss than those only uses the track P_T. FIG 4.6 shows the pre-selection efficiency as a function of P_T. Both CC and EC plots on FIG 4.6 show pre-selection efficiency is P_T dependable for probe electron below 25 GeV. In CC there are two P_T bins: $P_T > 25$ GeV and $P_T < 25$ GeV. Due to limited number of events below 25 GeV in EC, the pre-selection efficiency in EC is only plotted in η_D.

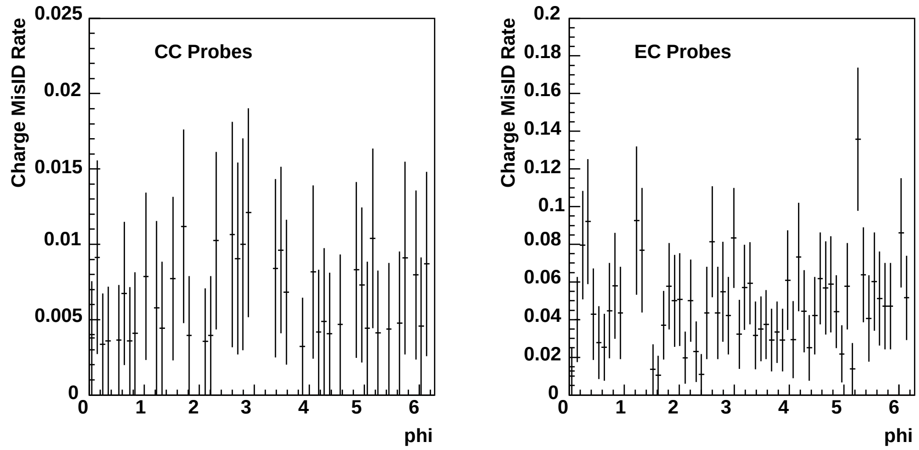

Figure 4.4: Charge mis-identification rate as a function of detector ϕ_D

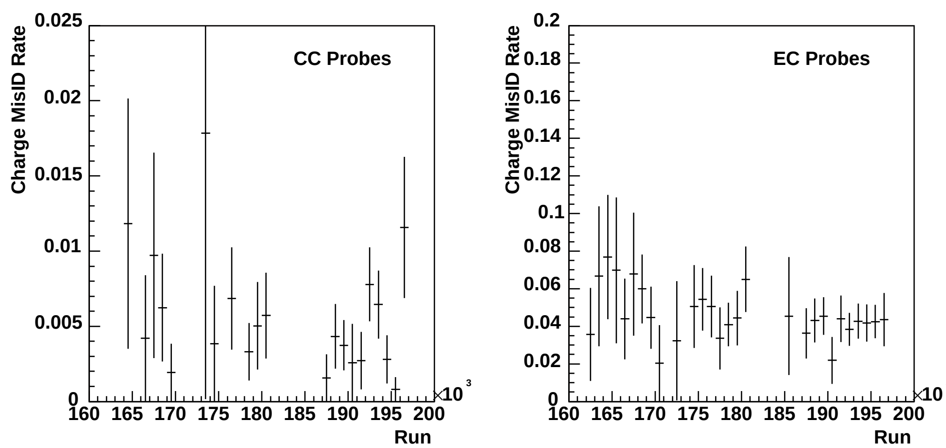

Figure 4.5: Charge mis-identification rate as a function of Run

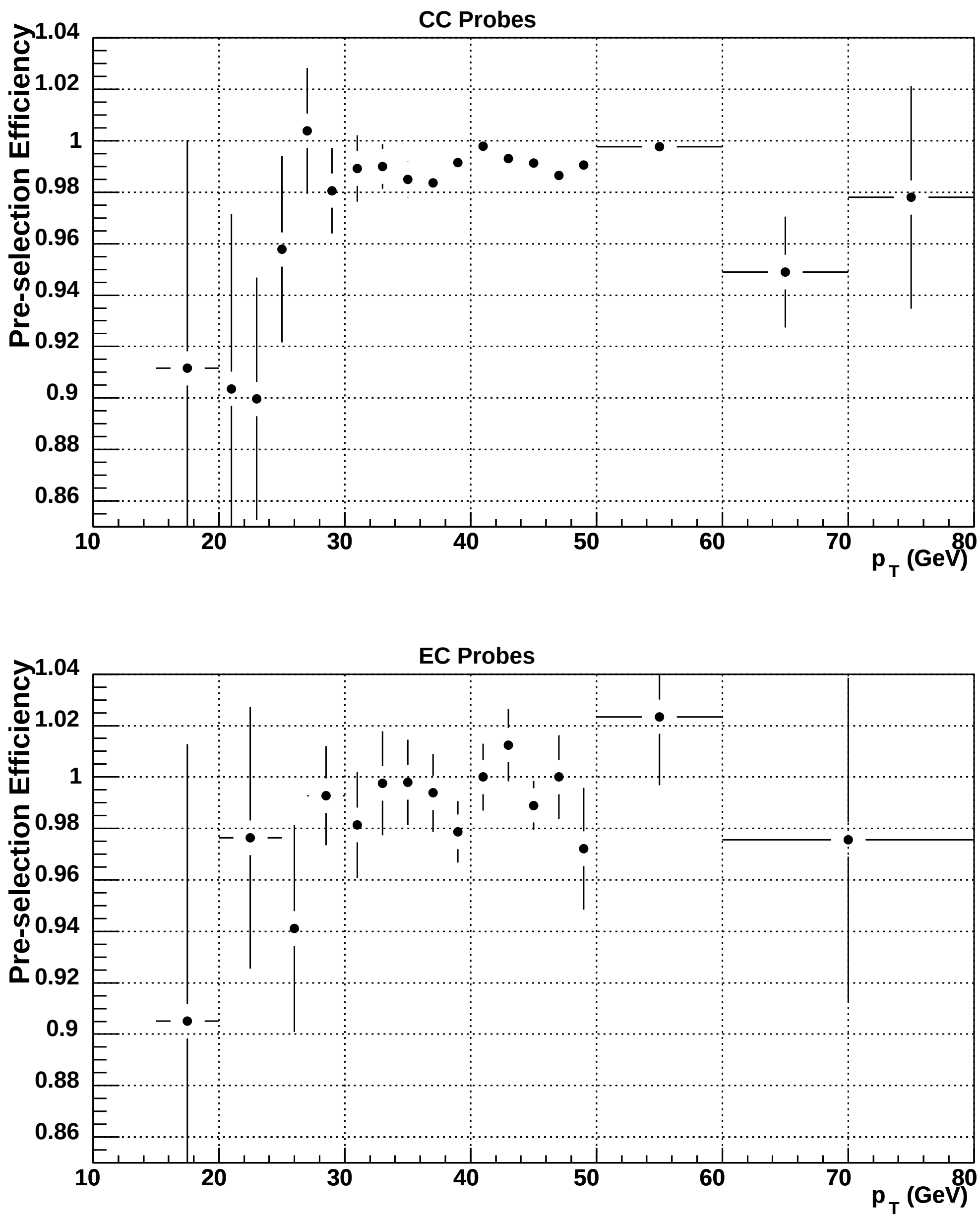

Figure 4.6: Preselection efficiency as a function of P_T in CC (top) and EC (bottom).

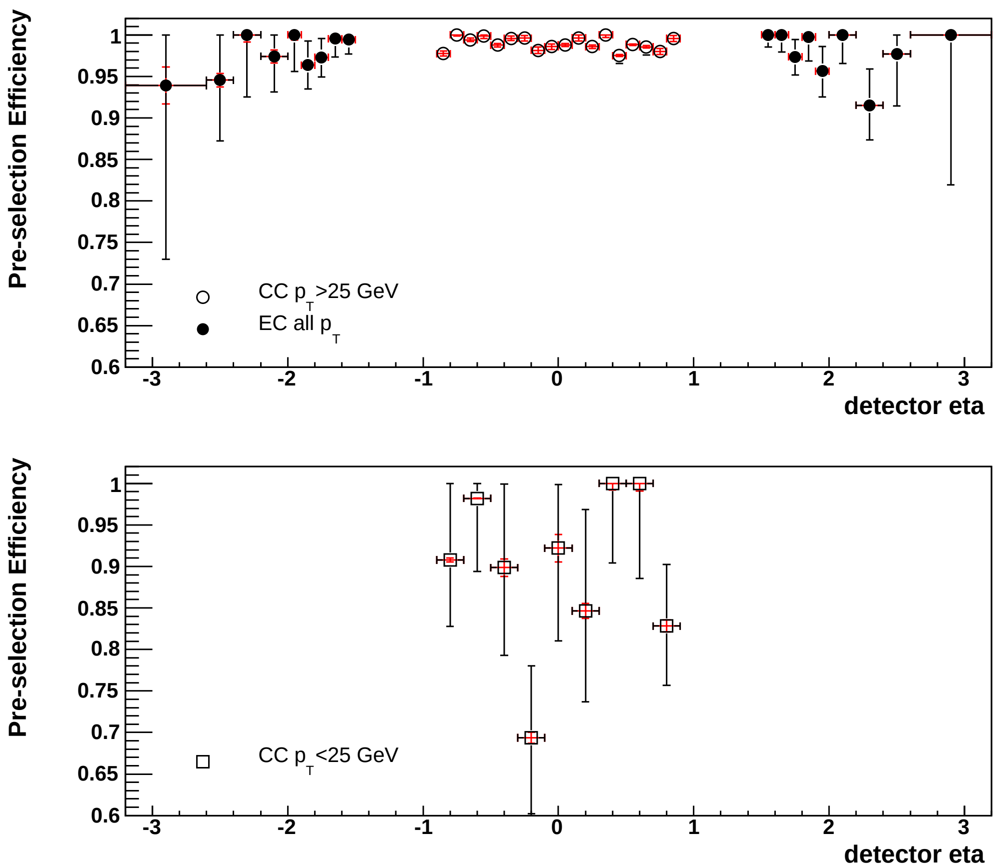

Figure 4.7: Preselection efficiency as a function of η_D and P_T in CC (top) and as a function of η_D in EC (bottom). Black error bars are statistical uncertainty, red ones are systematic uncertainty

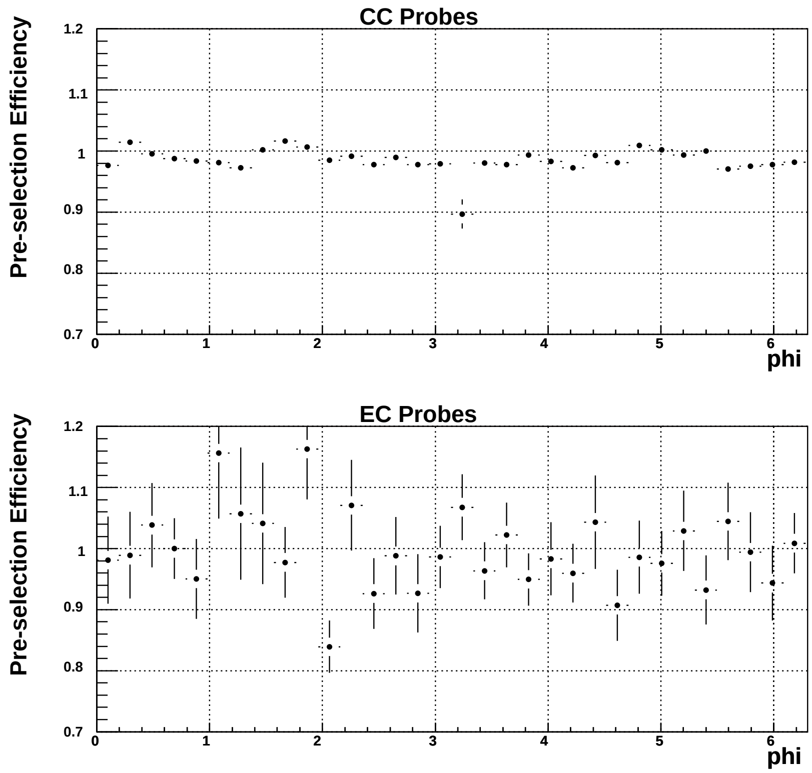

Figure 4.8: Preselection efficiency as a function of ϕ

Pre-selection efficiency ϕ, z_{vtx} and run dependency are also checked. FIG 4.8 shows the pre-selection efficiency as a function of ϕ, FIG 4.9 shows the pre-selection efficiency as a function of event z_{vtx}, and FIG 4.10 shows the pre-selection efficiency stability versus run period. In CC ϕ plot, due to hardware problem, module 17 is removed. A drop of pre-selection efficiency can be found on FIG 4.8. The data collected from this module is not used in analysis.

Systematic uncertainties from *tag-and-probe* method is estimated by comparing pre-selection efficiency from Monte Carlo events using *tag-and-probe* and Monte Carlo true value. Those results are plotted on FIG 4.11. Red error bars on FIG 4.8 are from systematics and black error bars are statistical uncertainty.

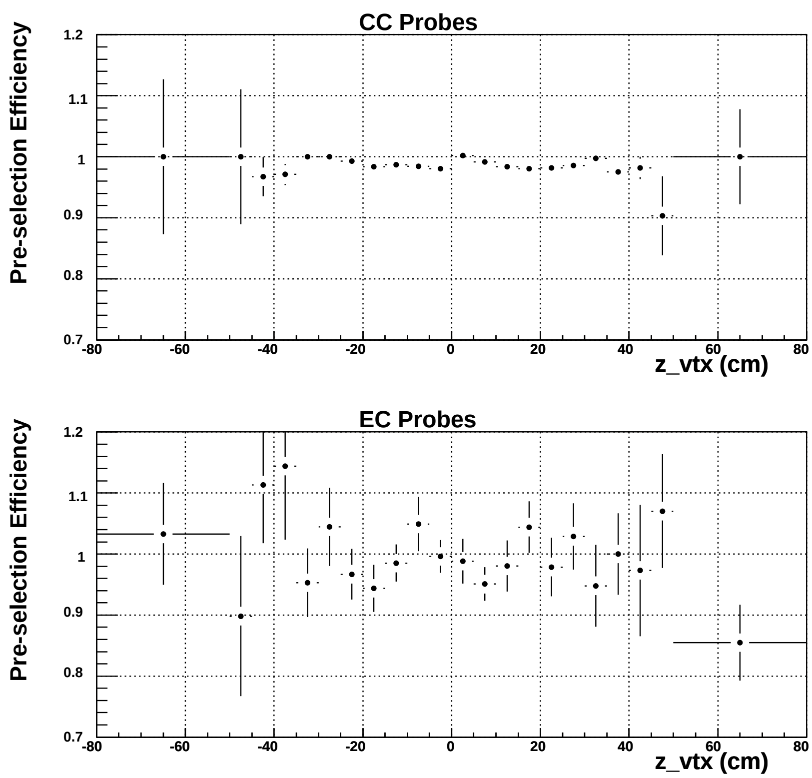

Figure 4.9: Preselection efficiency as a function of z_{vtx}

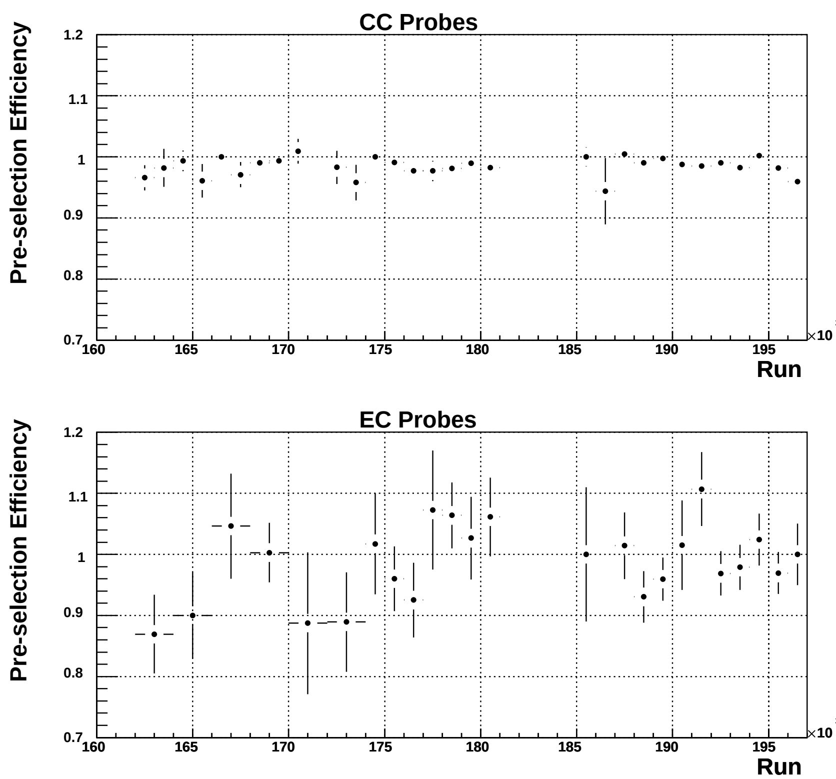

Figure 4.10: Preselection efficiency as a function of *Run*

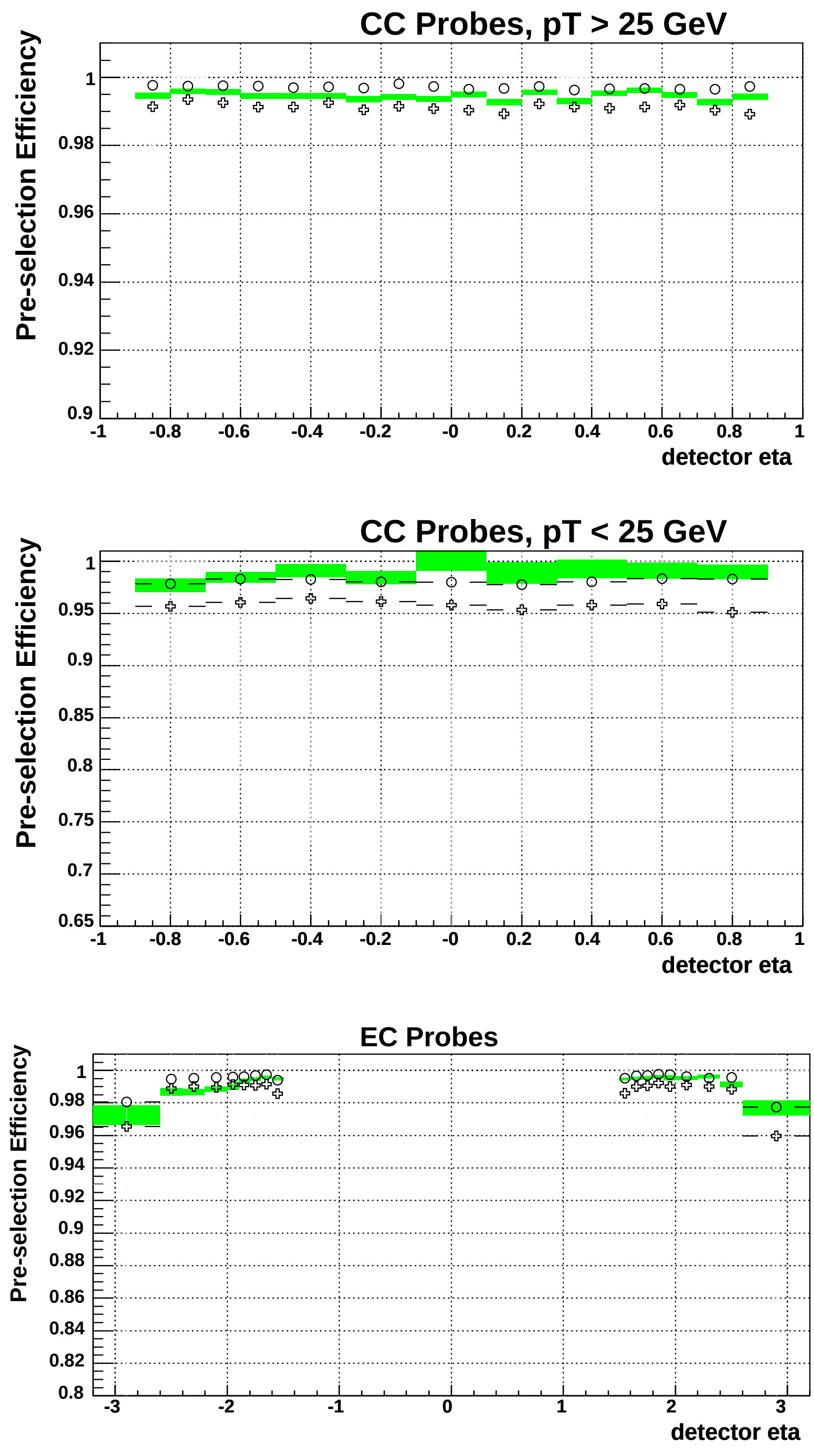

Figure 4.11: Pre-selection efficiency in CC and EC, from Monte Carlo tag-and-probe (green band), Monte Carlo true value with track match (circle) and Monte Carlo true value without track match (cross)

4.4 Trigger Efficiency

4.4.1 Method

The events used in trigger efficiency measurement must pass the cuts described in Section 3.8, except the track match requirement. There is also a 86 to 96 GeV mass window cut on invariant mass of electron pairs to reduce the background contamination. The tag is an electron with matched track and also passes electron ID cuts. P_T of electron is greater than 25 GeV to avoid trigger turn-on effect and background bias at low P_T region. Tag is also required to pass Level 1, Level 2, and Level 3 trigger conditions. Due to lower track match efficiency, probe electrons are not required to have the matched tracks. This configuration can increase number of events pass the cuts. Since efficiency is determined based on the tag electron, the result is not sensitive to whether there is a track match requirement applied on the probe electron.

Background is estimated by fitting 71 to 81 GeV and 101 to 111 GeV side band of Z boson invariant mass peak using the method described in Section 4.2. Signal to background ratio within Z boson invariant mass window is calculated based on the fitting results. It is found that background ratio of events with both electrons have track match is lower than those with at least one electron has the track match case. FIG 4.12 shows invariant mass plots with fitted background. Background to signal ratio within 71 to 111 GeV mass window is 1.4% for electron pairs with two track match. In the case with at least one track match, a noticeable amount of background is presented. Background to signal ratio increases to 1.6%.

In order to show whether background affect on the trigger efficiency measurement, a more broader invariant mass window cut is used. In this case, events with invariant mass larger than 110 GeV or less than 70 GeV are also included. FIG 4.13 shows the events with broader invariant mass window cut have even lower trigger efficiency. Because trigger efficiency is lower when more background is included, and background to signal ratio under wider mass window cuts is also higher for the same reason. This indicates, the lower trigger efficiency for the events with only one track match is due to the background. The similar effect can also be found on trigger efficiency

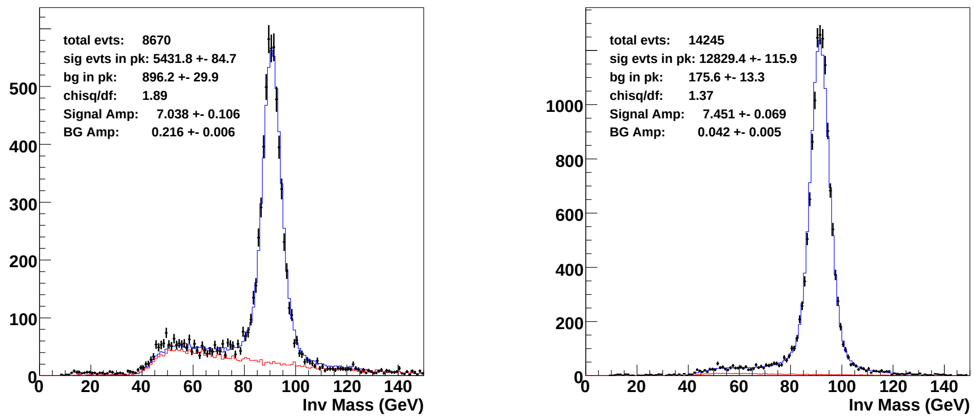

Figure 4.12: Background of events with at least one track (left) and two tracks (right)

versus η_D plots shown on FIG 4.16.

Besides background effect, electrons with track match have narrower shower, and trigger conditions use certain cuts related to electron shower shape. This can also contribute to the trigger efficiency measurement. This means the electron pairs with two track match and with one track match should be studied separately in trigger efficiency measurement.

4.4.2 Results

The trigger efficiency is plotted in η_D and P_T. Due to change of trigger conditions and hardware during different run period, the trigger efficiency is also run dependent. FIG 4.14 shows trigger efficiency P_T turn-on curve for both electrons with track match, overlapped with P_T turn-on curve with only one electron has track match, for the trigger combination version 8-10, version 11, version 12 and version 13. Both curves have 71 to 111 GeV invariant mass cut. Difference can be found from the trigger turn-on curves with or without track match.

Trigger version 8 to 10, version 11, 12, and 13 have different trigger conditions. Trigger P_T turn-on efficiency is also different due to those different conditions. FIG 4.15 shows the P_T turn-on curves of different trigger versions. Red points are from events with only one track match. Black points are from events with two track match.

The trigger efficiency versus η_D is also plotted for the different versions of trigger list.

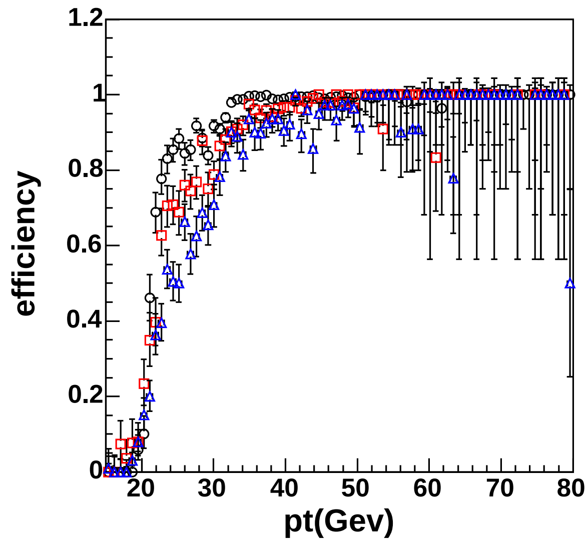

Figure 4.13: Compare trigger efficiencies with different invariant mass windows, broad mass window cut have lower trigger efficiency. Circle: with 2 track match; Square: with one track match; Triangle: with one track match and broader invariant mass window

FIG 4.16 show the trigger efficiency of different trigger versions as function of η_D of the probe electrons.

FIG 4.17 shows trigger efficiency versus z_{vtx}, track z_{vtx} of different versions of trigger list.

Trigger efficiency at different run range is also studied in order to show the stability of trigger efficiency over time (FIG 4.18). The final trigger efficiency used in the analysis is measured in a multi-dimension phase space of η_D, P_T and z_{vtx} for each trigger version used.

4.5 H Matrix Efficiencies

4.5.1 Method

Events in H Matrix efficiencies study must pass the standard quality cuts listed on Section 3.8. Probe electrons have to pass the H Matrix cut at specific value under study. Background is removed at bin-by-bin base using the background fitting method described in Section 4.2. When background is present, the *tag-and-probe* method from equation 4.4 for H Matrix study is modified to:

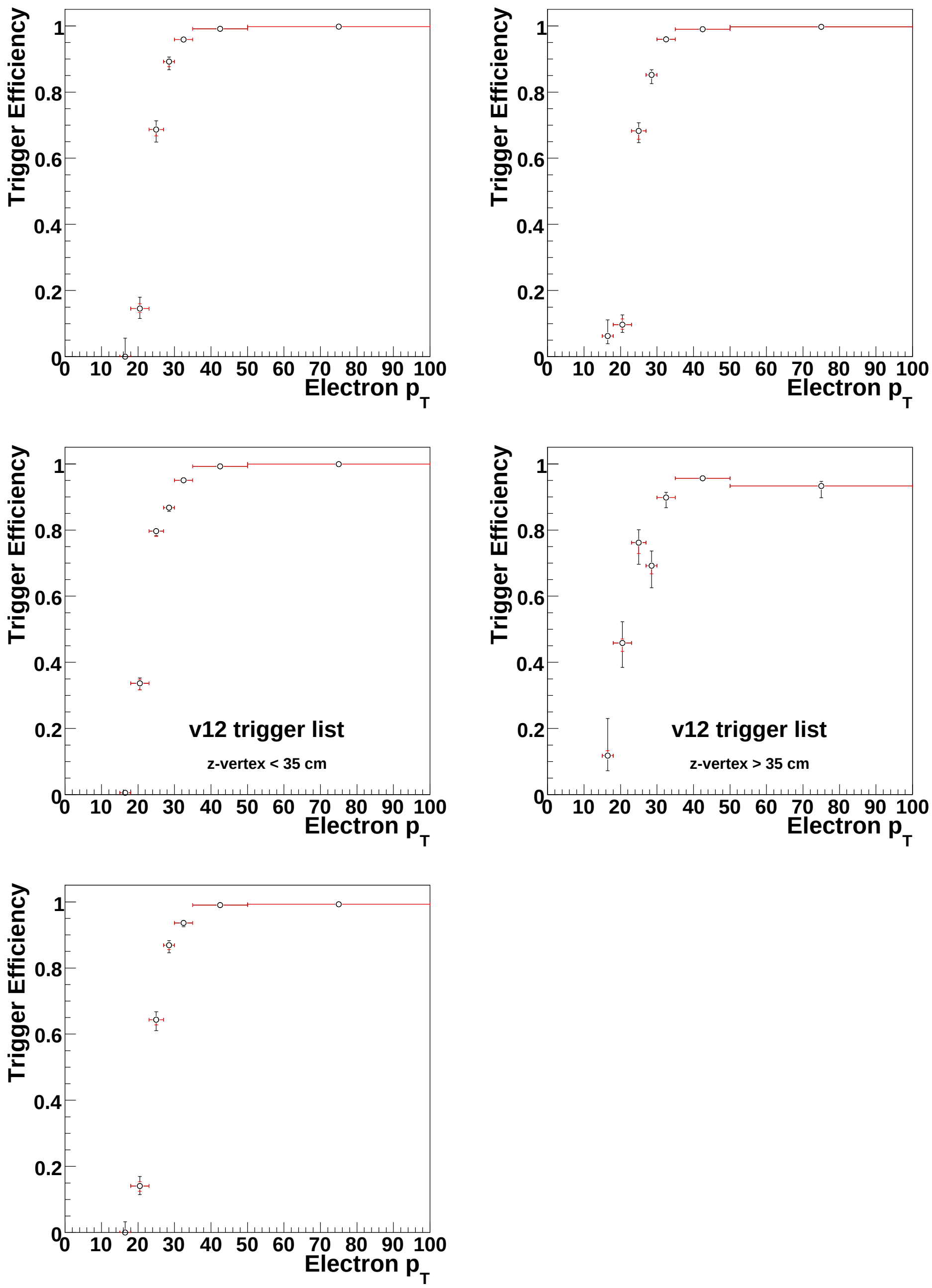

Figure 4.14: Trigger efficiencies as a function of P_T averaged over η_D for v8–10, v11, v12 for vertex $z < 35$ cm, and v12 for vertex $z > 35$ cm, and for v13.

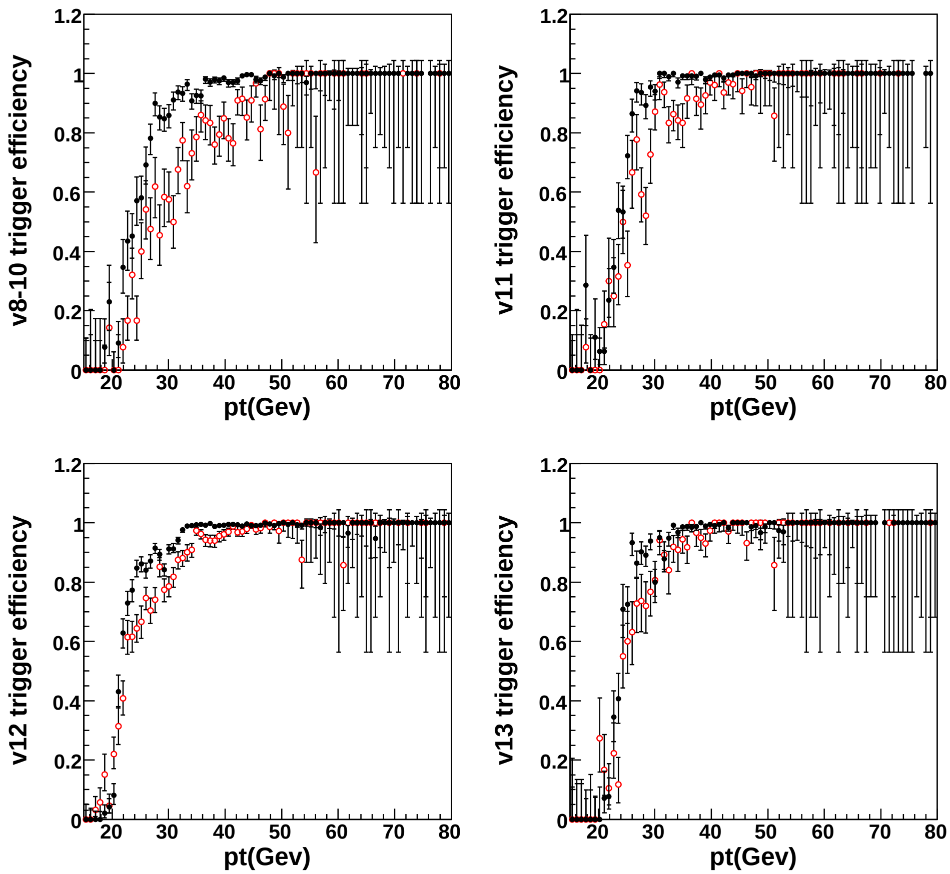

Figure 4.15: Trigger efficiencies vs P_T for v8, v11, v12, and v13. Filled circles are for track-track data and open circles for for track–no-track data.

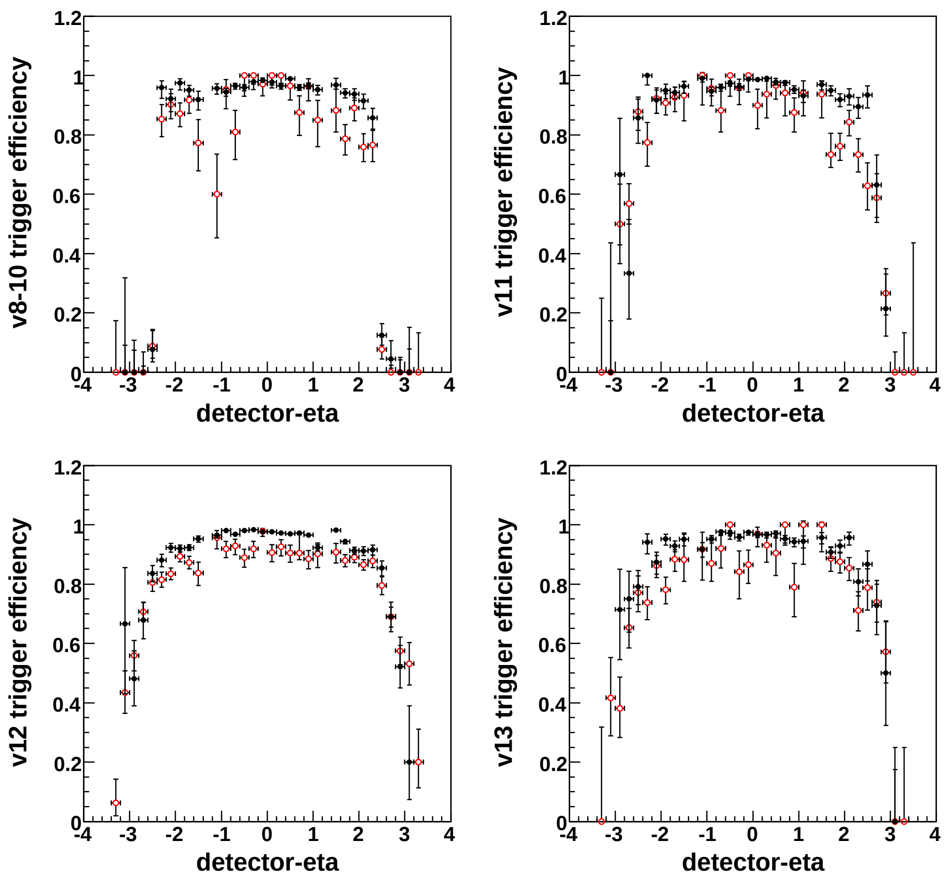

Figure 4.16: Trigger efficiencies at different range of η_D of probe electron

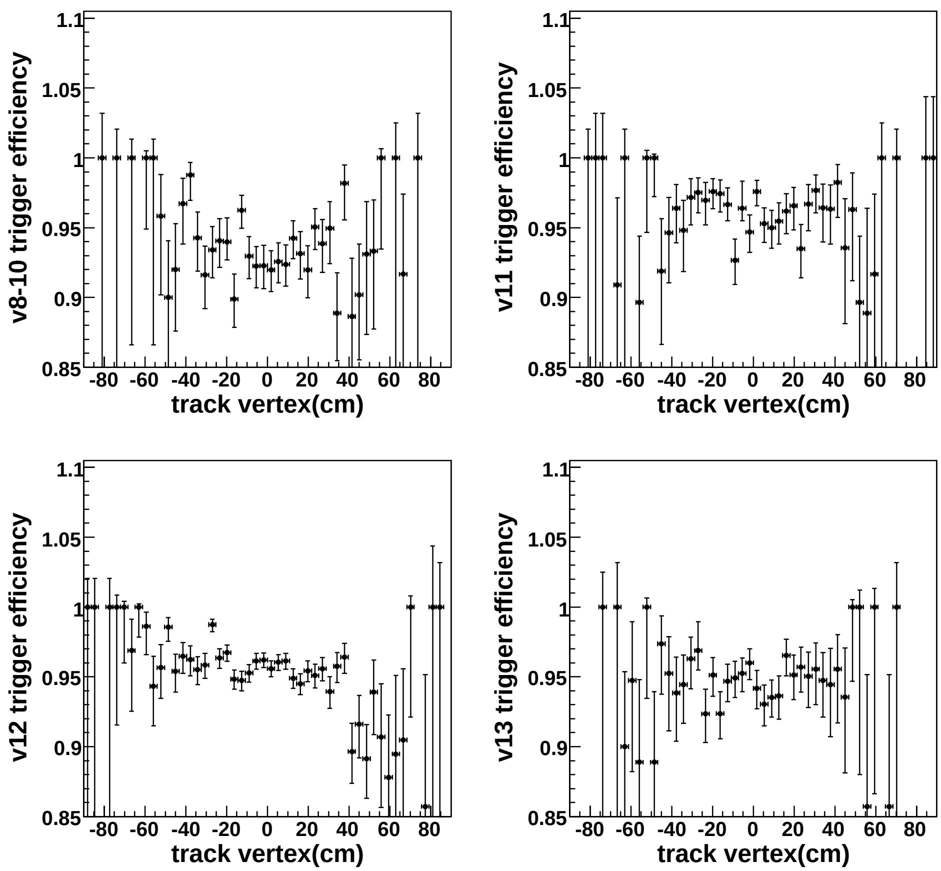

Figure 4.17: Trigger efficiency at different track vertex position along z axis of probe electron

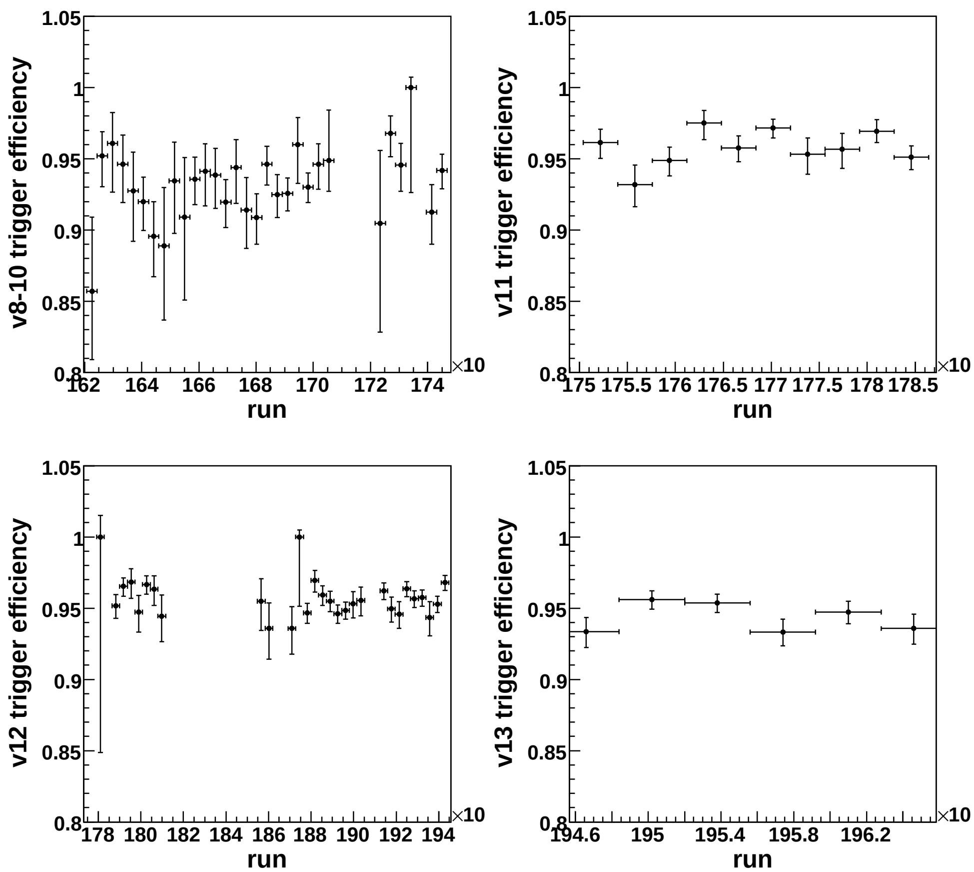

Figure 4.18: Trigger efficiencies vs run number for v8-10, v11, v12, and v13.

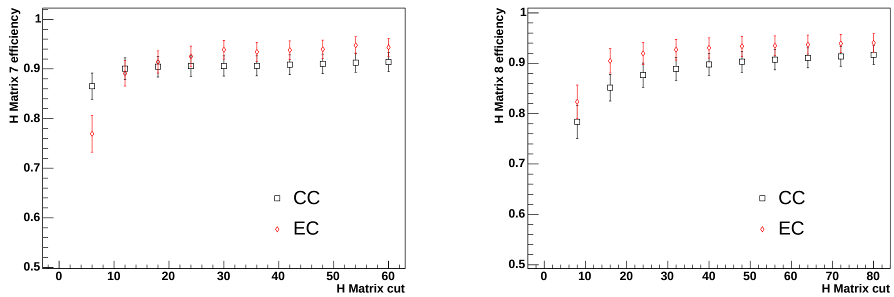

Figure 4.19: The turn on of H matrix cut efficiency at different cut value

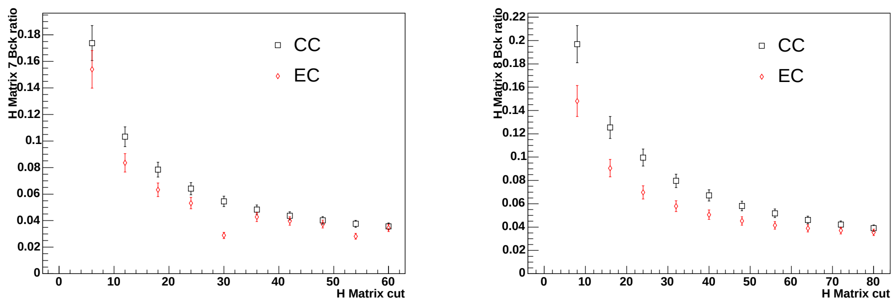

Figure 4.20: Relative signal to background ratio at different cut value, plot at arbitrary vertical scale

$$\varepsilon = \frac{2N_{tt} + N_{tp} - BG_{num}}{2N_{tt} + N_{tp} + N_{tf} - BG_{den}} \tag{4.11}$$

where BG_{num} is fitted background number from numerator $2N_{tt} + N_{tp}$, and BG_{den} is the fitted background from denominator $2N_{tt} + N_{tp} + N_{tf}$. Due to ϕ crack in CC EM calorimeter is not well modeled in Monte Carlo, using H Matrix 8 cut can not yield good results in CC region because of the additional requirement on transverse width of shower. As a result, H Matrix 7 in CC, and in EC region, H Matrix 8 is selected since there is no ϕ crack problem.

In order to determine H Matrix cut value with high efficiency and low background, H Matrix turn-on curves are plotted (FIG 4.19). Fig 4.20 shows the background ratio at different H Matrix cut values. H Matrix cut is selected in a way that maintains relative flat and high efficiency over η_D, but with low background. Based on these arguments, H Matrix 7 used in CC is cut at 12 and H Matrix 8 in EC is cut at 20.

4.5.2 Results

The H Matrix efficiency is plotted in η_D, ϕ_D, and P_T. Average value of H Matrix efficiency is measured first as a cross check: in CC region, H Matrix 7 efficiency is 96.7 ± 0.2 for probe electron with track match. H Matrix 8 efficiency in EC is 96.4 ± 0.2 when the probe electron with track match and is 88.8 ± 0.7 if the probe electron without track match. Both H Matrix 7 and H Matrix 8 efficiencies are relative flat over all η_D for the probe electron with or without track match. Since most of the bad calorimeter areas are located within negative η_D region, H Matrix 8 efficiency in negative EC drops to 96.0 ± 0.4 and positive EC is 97.0 ± 0.3 for the probe electron without track match. When the probe electron has track match, H Matrix 8 efficiency is 90.0 ± 1.0 for negative EC and 88.0 ± 1.0 for the positive EC.

Both H Matrix 7 and 8 efficiency curves have a small P_T dependable slope. To demonstrate this slope, H Matrix 7 (in CC) and H Matrix 8 (in EC) efficiencies are plotted in P_T in 15 to 25 GeV, 25 to 35 GeV, 35 to 45 GeV and $P_T > 45$ GeV bins, as shown on right column of FIG 4.21. Background in each bin has been subtracted. Since H Matrix efficiencies are P_T dependable, a P_T dependable effect on H Matrix efficiencies is applied in the analysis.

H Matrix efficiencies as a function of η_D is shown on the left column of FIG 4.21. Monte Carlo results are also shown on the plots for reference. Since H Matrix compares shower shape between data and Monte Carlo result, and the electrons with track match have narrower shower. As results electrons without track match have lower H Matrix efficiency due to their relative broader shower. The last plot on the left column of FIG 4.21 shows this effect.

H Matrix 7 and 8 efficiencies are plotted as a function of run number in right column of FIG 4.22. These plots show efficiencies are relative stable over the whole run ranges, except for the efficiencies of the electrons without track match and run number less than 183,000, which have relative lower values. Left column of FIG 4.22 shows H Matrix efficiencies as a function of ϕ_D. No ϕ_D dependence is found.

The final H Matrix efficiencies in the analysis are measured in (P_T, η_D) for electrons with track match and without track match. FIG 4.23 shows the distributions.

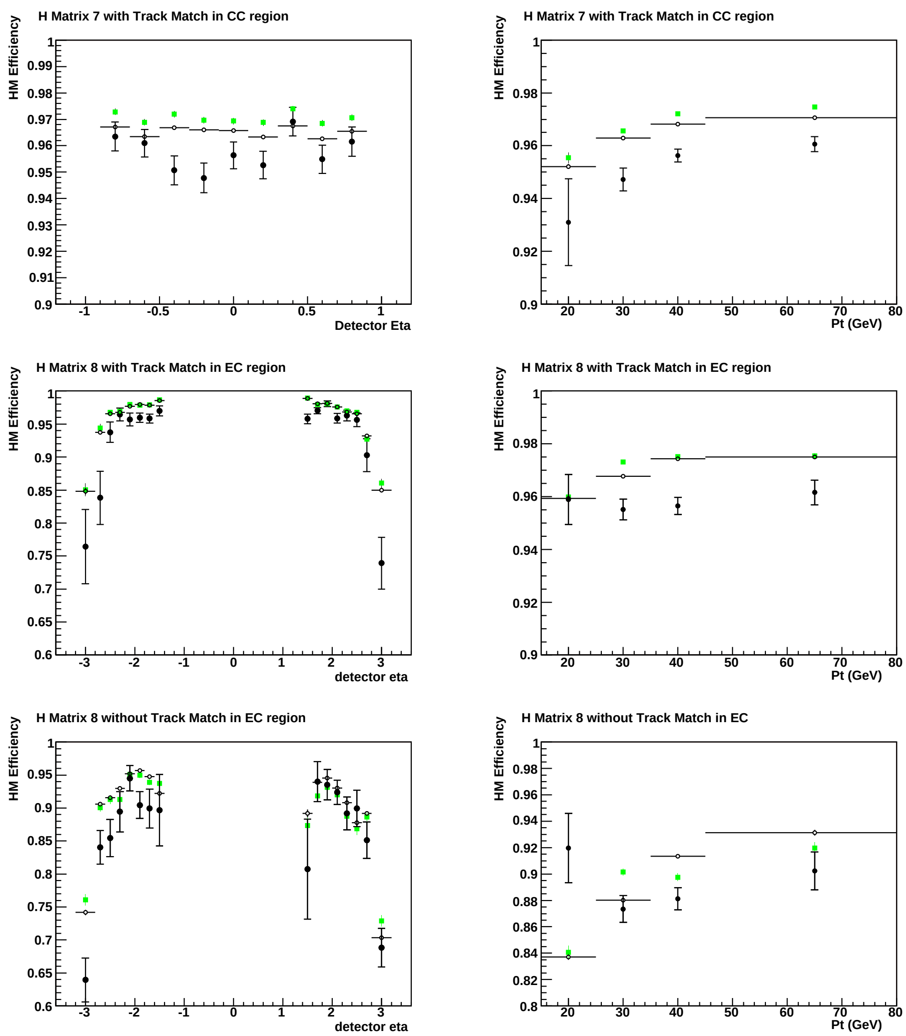

Figure 4.21: H Matrix efficiencies versus η_D in the left column and versus P_T in the right column. Solid circles: data, open circles: Monte Carlo true value, square: Monte Carlo tag-and-probe

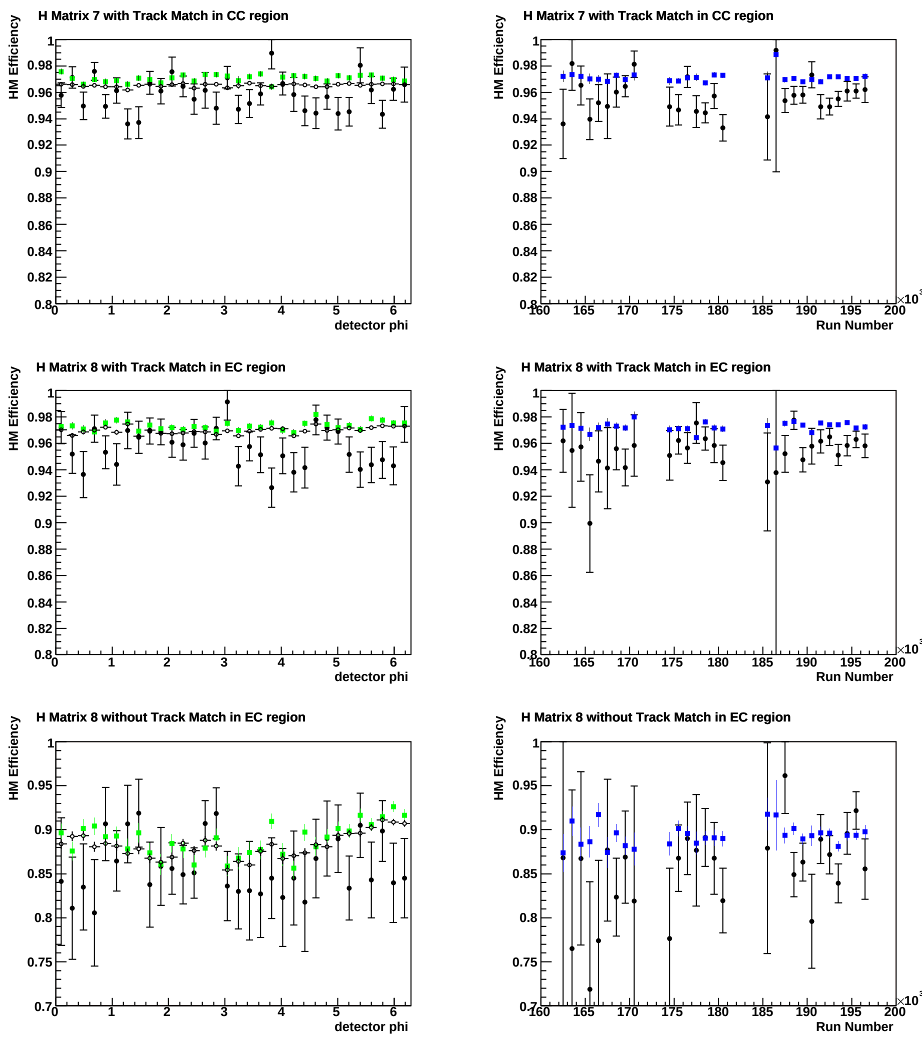

Figure 4.22: H Matrix efficiencies as functions of ϕ_D (left) and run number (right). Solid circles: data, open circles: Monte Carlo true value, square: Monte Carlo tag-and-probe

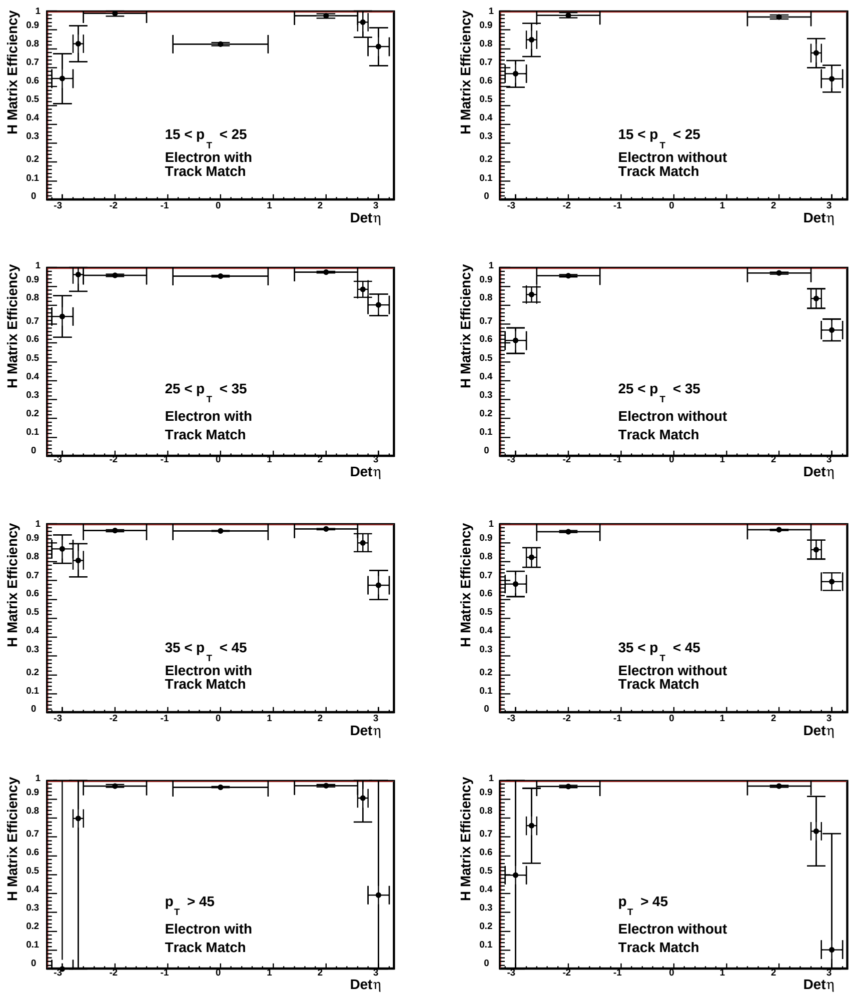

Figure 4.23: H Matrix efficiencies in (P_T, η_D), with track match (left column) and without track match (right column)

The systematic uncertainties of H Matrix efficiencies measurement come from two sources: from *tag-and-probe* method and from background subtraction. For uncertainty from the *tag-and-probe* method, H Matrix efficiencies from Monte Carlo events using *tag-and-probe* method and true Monte Carlo value are compared, under the same conditions used in data. The absolute value of this difference is treated as systematic uncertainty from the *tag-and-probe* method. Since Monte Carlo efficiencies are relative higher than the data's, the systematic uncertainty from the *tag-and-probe* method is scaled by ratio of efficiency from data over the efficiency from the Monte Carlo events .

To estimate uncertainty from background subtraction method, tighten H Matrix cuts (H Matrix 7 < 6 in CC and H Matrix 8 < 10 in EC) are used. The difference is taken as part of uncertainties.

4.6 Track Match Efficiency

4.6.1 Method

The track match efficiency determines efficiency of track match requirement applied on the electron selection. When using the *tag-and-probe* method to determine track match efficiency, tag is an electron which has a matched track. P_T of the electron is greater than 25 GeV and the electron also fires a single EM trigger listed on Section 3.2. Probe is an EM cluster with P_T greater than 15 GeV. But it is not required to have a matched track. Both tag and probe clusters are required to pass the following additional cuts: f_{iso} is less than 0.15, f_{em} is greater then 90% and H Matrix $7 < 12$ in CC or H Matrix $8 < 20$ if in EC.

The track matching efficiency is plotted in η_D, z_{vtx} and the boson rapidity. Background is removed in each bin by fitting invariant mass peak of data with the shape of mass peak from Monte Carlo simulation or exponential curve, as described in Section 4.2. The fitting is done between 81 to 101 GeV invariant mass range. The reason to use exponential background curve is to avoid possible correlation between spatial track match and the shape of cluster shower.

4.6.2 Results

The track match efficiency depends on the amount of tracking material that charged particles can travel through. The shortest length of tacking material that particles can travel through is at $\eta_D = 0$. Corespondent track match efficiency is relative lower. FIG 4.24, FIG 4.25 and FIG 4.26 show the track match efficiency in η_D, a dip on efficiency curve around $\eta_D = 0$ can be observed due to this reason. For the same reason, track match efficiency is highly correlated to z_{vtx}. When z_{vtx} moves to positive side, the central dip also shifts to the positive side of η_D due to the change in the total amount of tracking material that electrons can pass through. Electrons with negative z_{vtx} have the similar result. Since $D\O$ tracking system has no CFT in EC, a lower track match efficiency is observed in that region.

The track match efficiency is plotted as functions of vertex z position and η_D in three Z boson rapidity regions: $|y| < 0.5$, $0.5 < |y| < 2$ and $2 < |y| < 3$. The results are shown on FIG 4.24, FIG 4.25, and FIG 4.26.

Monte Carlo simulation is used to cross check the results from data. FIG 4.27 shows the track match efficiency in CC (left) and EC (right). In EC region it is relative flat over electron P_T. But in EC, the track match efficiency is highly correlated with P_T. Since track momentum is related with momentum of Z boson. Low P_T tracks are more tend to be in EC region, and are lower in track match efficiency due to no CFT in this area. FIG 4.28 shows how the track P_T correlated with η_D.

Track match efficiency as a function of ϕ or run number is also checked (FIG 4.29). The slightly changes in efficiency on those plots are not found to affect Z boson rapidity distribution.

Systematic uncertainties of the track match efficiency are from two sources: from the *tag-and-probe* method, and from the background subtraction. The first source of uncertainty is estimated by comparing Monte Carlo events efficiency using the *tag-and-probe* method and true Monte Carlo information. Although full simulation Monte Carlo does not model data very precisely, it is still good enough to estimate systematic uncertainties. This uncertainty is also measured in η_D, z_{vtx} and boson rapidity. In CC, the difference between Monte Carlo events efficiency from

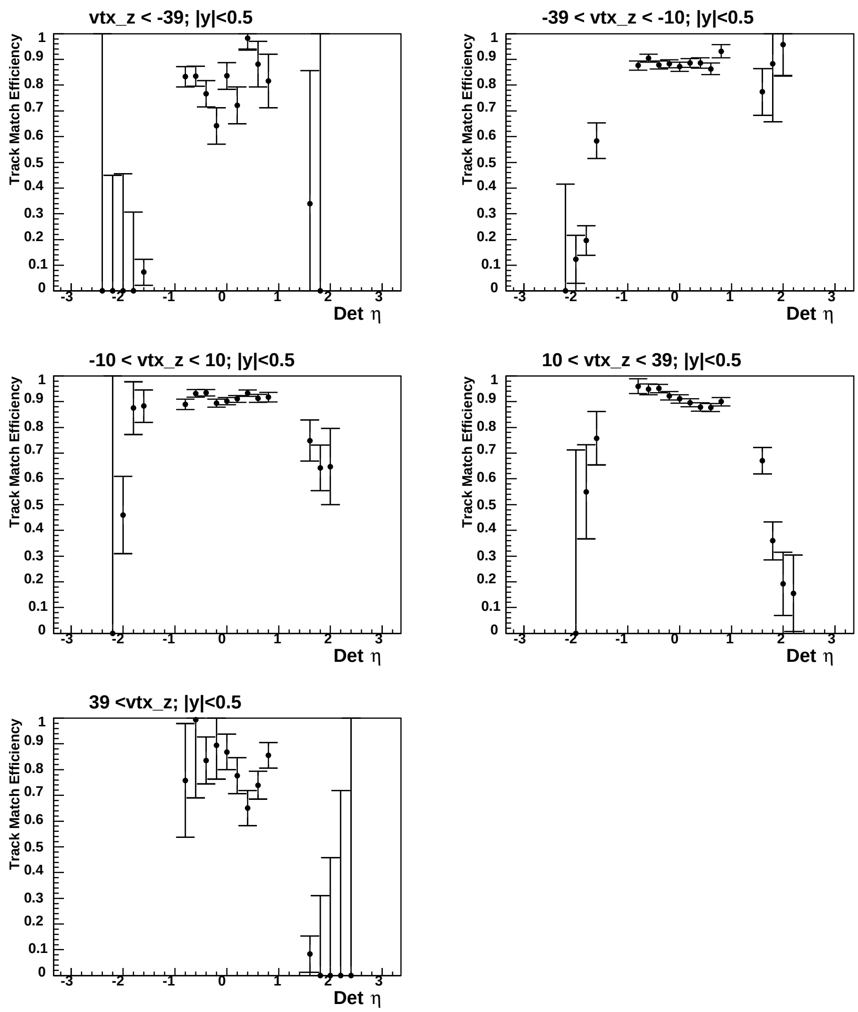

Figure 4.24: Track match efficiency plotted in η_D at five vertex z bins, and $|y| < 0.5$

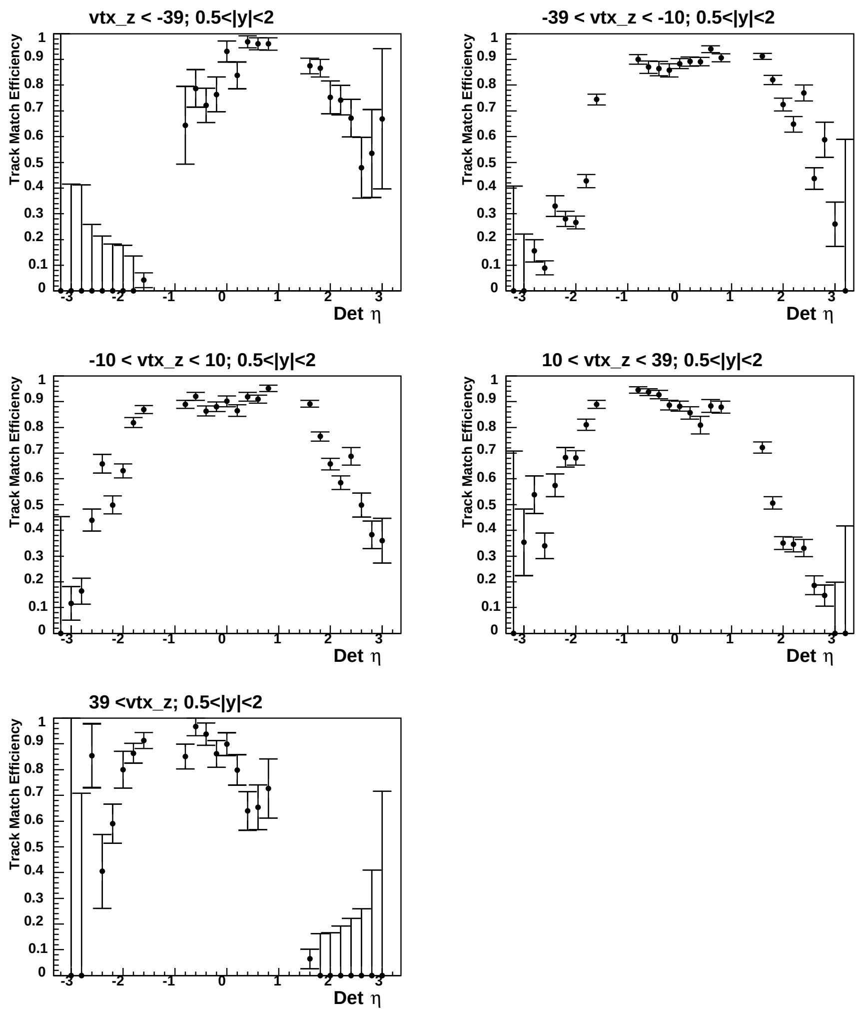

Figure 4.25: Track match efficiency plotted in η_D at five vertex z bins, and $0.5 < |y| < 2.0$.

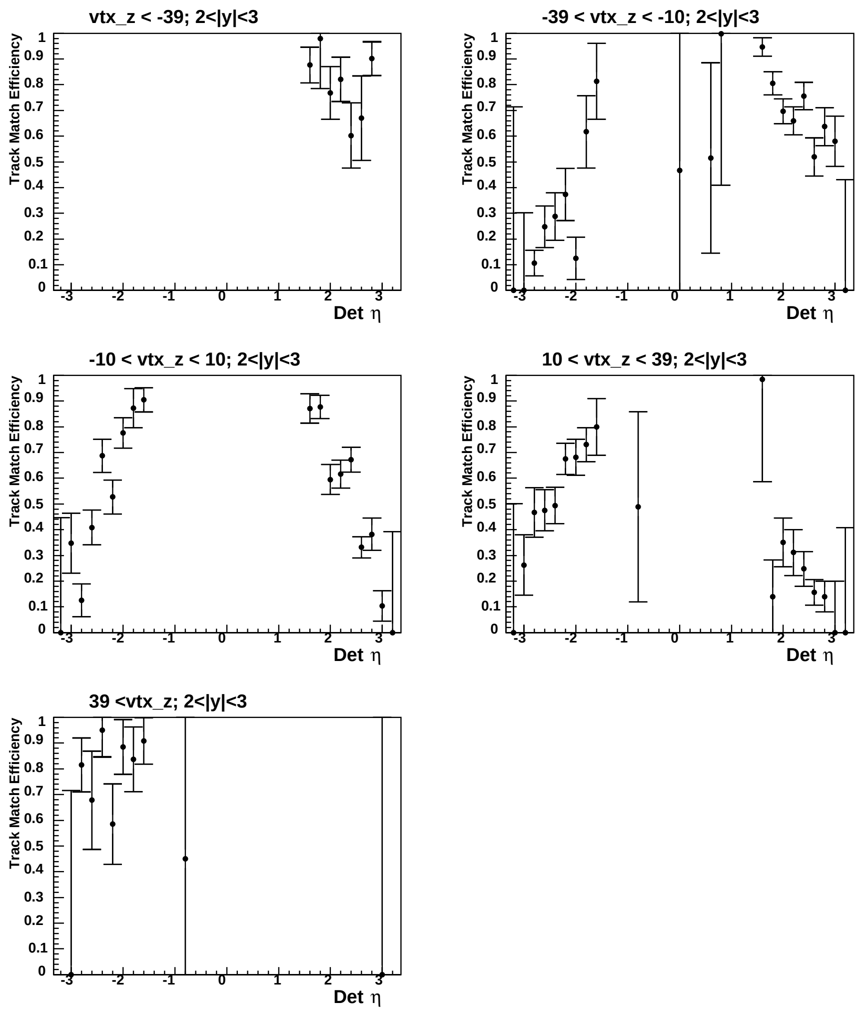

Figure 4.26: Track match efficiency plotted in η_D at five vertex z bins, and $2.0 < |y| < 3.0$.

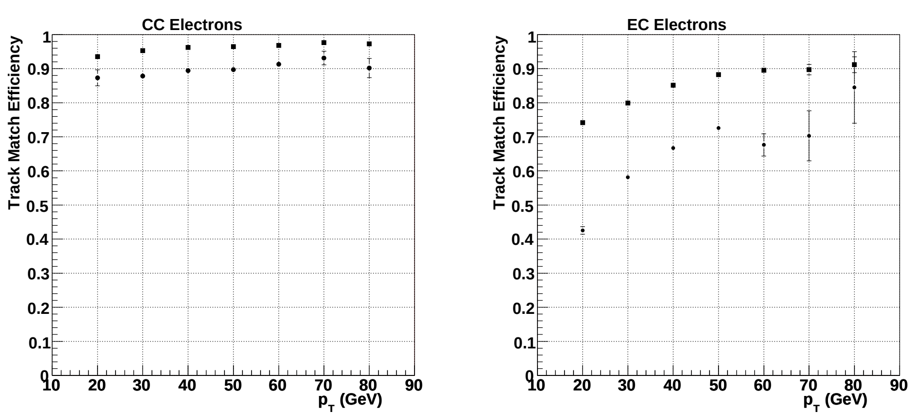

(a) (b)

Figure 4.27: Track match efficiency as a function of electron P_T in the CC and EC region, solid square: Monte Carlo, solid circle: data

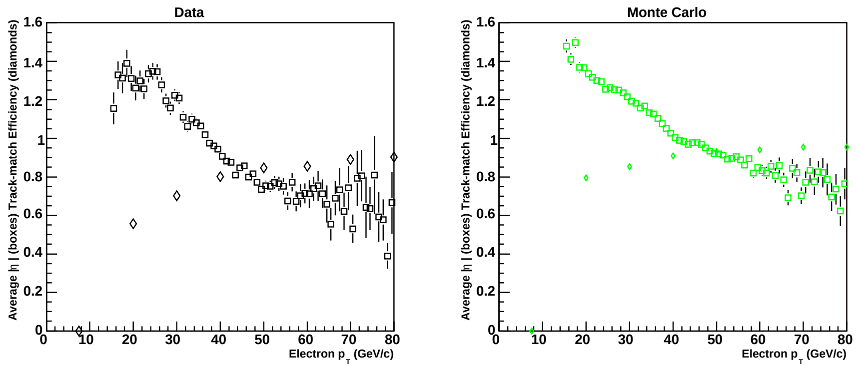

(a) (b)

Figure 4.28: Track match efficiency (diamond) and Track $|\eta_D|$ (box) as function of P_T from data (left) and Monte Carlo (right).

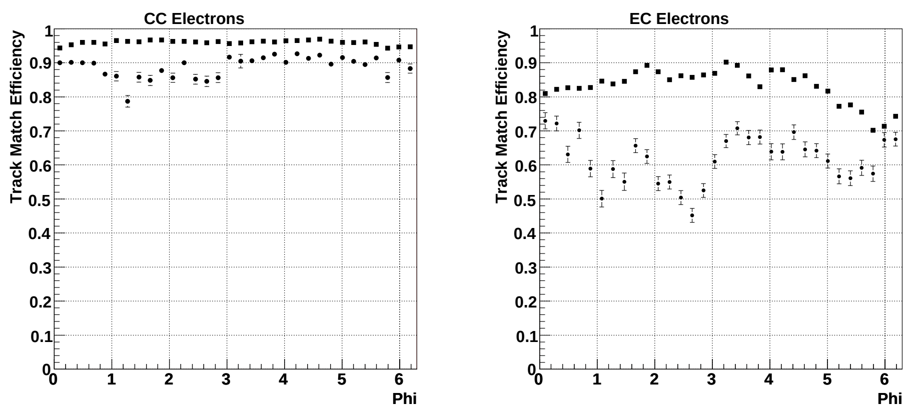

(a) (b)

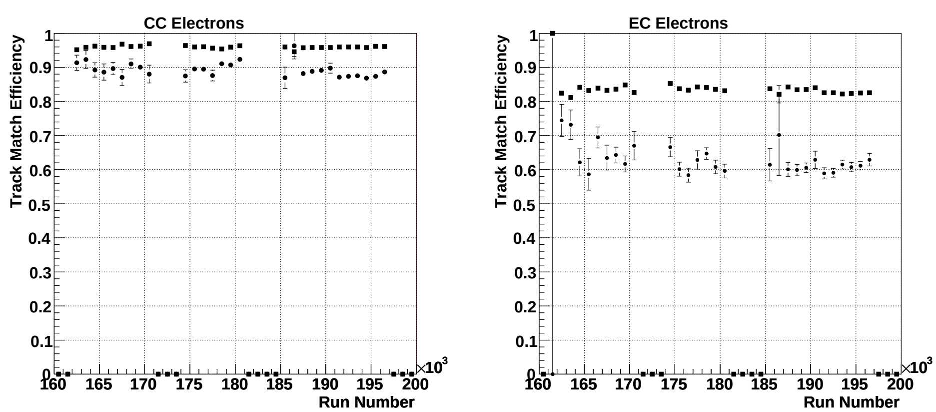

(c) (d)

Figure 4.29: Track match efficiency as a function of electron ϕ and in CC and EC region, solid square: Monte Carlo, solid circle: data

the *tag-and-probe* method and the true values are treated as systematic uncertainty. FIG 4.30 indicates this part of uncertainty is smaller in CC region. For the EC region, ratio of Monte Carlo true efficiency versus Monte Carlo *tag-and-probe* efficiency is applied as a scale factor on the measured track match efficiency. This avoids possible bias due to the track match requirement on tag electron when it is in EC region.

Systematic uncertainties from background subtraction is estimated by tighten H Matrix cut value. By tighten H Matrix cut on the tag electron to half, the track efficiency is reduced 0.79% for CC electron if $|y| < 0.5$, 0.46% for CC electron if $|y| > 0.5$, and 0.79% for all EC electrons.

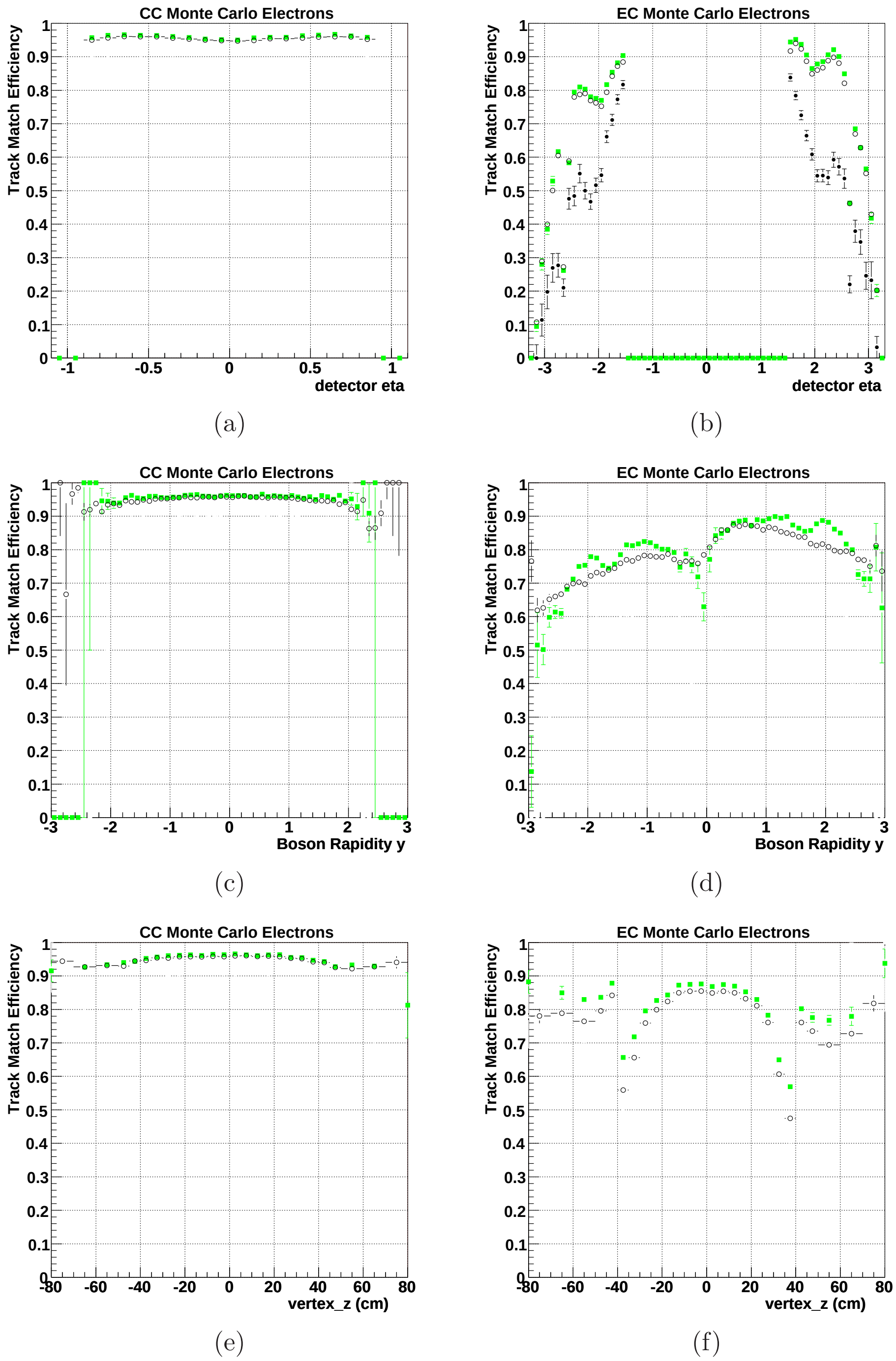

Figure 4.30: Monte Carlo Track match efficiency from tag-and-probe method and true efficiency. Green solid square: Monte Carlo tag-and-probe, black circle: Monte Carlo true efficiency

Chapter 5

Efficiency and Acceptance of Z boson

In this chapter the author focus on the method to determine efficiency of Z boson based on the measured efficiencies of electron. Monte Carlo simulation and how to use Monte Carlo simulation in determining acceptance is also presented.

5.1 Theory

Electron efficiencies are measured at a multi-dimensional phase space: η_D, ϕ_D, z_{vtx}, and P_T, etc. Suppose a Z boson with (P_T, η, ϕ) decays to an pair of electrons: e_1, and e_2. Define ε_Z: the efficiency to re-construct a Z boson at rapidity y. ε_Z can be calculated if we know exactly where are the two electrons located at calorimeter, and what are the measured efficiencies of those two electrons in multi-dimensional phase space at these locations:

$$\varepsilon_Z(P_T, \eta, \phi) = \varepsilon_{e1}(P_T^1, \eta^1, \phi^1) \times \varepsilon_{e2}(P_T^2, \eta^2, \phi^2) \tag{5.1}$$

where ε_{e1} and ε_{e2} are the measured electron efficiency. In the experiment, we have more than 10,000 of Z bosons with background at various energy and rapidity y. But we can not separate background from Z boson and exactly determine which electron decays from this Z boson at regions of η_D. Statistically, the efficiency of re-constructing a Z boson at rapidity y is a weighted summation of efficiencies of all possible observed electrons from this Z boson:

$$\varepsilon_Z(y) = \sum_{i,j}^{all} \sigma(e_1^i, e_2^j)\varepsilon_{e1}^i \times \varepsilon_{e2}^j \tag{5.2}$$

where $\sigma(e_1^i, e_2^j)$ is a possibility density function to find electron pair (e_1^i, e_2^j) from Z boson at location i, j of detector, respectively. If we know how to write $\sigma(e_1^i, e_2^j)$ analytically for all possible pairs of electrons, it is easy to calculate efficiency of Z boson due to selection cuts applied on its decay products: electrons. However, there is no such analytical expression for $\sigma(e_1^i, e_2^j)$.

In order to determine $\varepsilon_Z(y)$, a Monte Carlo algorithm is developed. Suppose we have a function of electron efficiency $\varepsilon_e(x_i)$. x_i are a set of multiple dimensional observables in which efficiency function $\varepsilon_e(x_i)$ is measured. In this analysis, $x_i \in (\eta_D, \phi, P_T, z_{vtx}, ...)$. If these observables are independent and the probability distribution function ρ $(0 \le \rho \le 1)$ of the measurement is well understood. We can define a *Heaviside* function $H(\rho)$, which is a functional of x_i:

$$H(\rho_{xi}) = \begin{cases} 1 & \text{if } \rho_{xi} \le \varepsilon_e(x_i), \\ 0 & \text{if } \rho_{xi} > \varepsilon_e(x_i). \end{cases} \tag{5.3}$$

If the total number of Z bosons N is generated by a well modeled $Z/\gamma^* \to e^+e^-$ Monte Carlo simulation. Since we already know the relationship between Z boson and its decay products electron. The efficiency of Z boson $\varepsilon_Z(y)$ at rapidity y can be calculated by:

$$\varepsilon_Z(y) = \frac{1}{N} \int_{xi=1}^{N} \int_{xj=1}^{N} H(\rho_{xi}) H(\rho_{xj}) dx_i dx_j; \tag{5.4}$$

where $H(\rho_{xi})$ is a functional of set of observables of electron i. The distribution of ρ $(0 \le \rho \le 1)$ is determined by how the electron efficiencies $\varepsilon_e(x_i)$ are measured.

5.2 Experiment technique

In the measurement, the efficiency of Z boson ϵ_Z is determined by the efficiencies of electron:

$$\begin{aligned} \epsilon_Z \quad = \quad & \epsilon_{\rm pre}(\eta_{D1}, P_{T1}, z_{vtx}) * \epsilon_{\rm pre}(\eta_{D2}, P_{T2}, z_{vtx}) * \\ & \epsilon_{\rm lt}(\eta_{D1}, z_{vtx}) * \epsilon_{\rm lt}(\eta_{D2}, z_{vtx}) * \\ & \epsilon_{\rm hmx}(\eta_{D1}, P_{T1}, \text{track}_1) * \epsilon_{\rm hmx}(\eta_{D2}, P_{T2}, \text{track}_2) * \\ & [1 - (1 - \epsilon_{\rm tt}(\eta_{D1}, z_{vtx})) * (1 - \epsilon_{\rm tt}(\eta_{D2}, z_{vtx}))] * \\ & [1 - (1 - \epsilon_{\rm trig}(\eta_{D1}, P_{T1}, \text{run})) * (1 - \epsilon_{\rm trig}(\eta_{D2}, P_{T2}, \text{run}))] \end{aligned} \tag{5.5}$$

In the analysis, Monte Carlo simulation generates $Z/\gamma^* \rightarrow e^+e^-$ events with proper $D\O$ detector simulation. The events are applied with the same acceptance cuts as those used in data. Then equation 5.4 is used to determine efficiency of Z boson.

RESBOS is the Monte Carlo generator used in this analysis. It is a W/Z events generator generating the leading order W/Z events with the next to leading order QCD correction. QED radiative photon correction is done by *PHOTOS*. The latest next to leading order CTEQ6M PDF sets is used. The Monte Carlo generator generates a table of $Z/\gamma^* \rightarrow e^+e^-$ events. These events are fed into *PMCS* [23] for detector simulation. Detector geometry cuts, resolution and response smearing are applied to the generated events at this stage. Then a set of *Homogeneous* distributed random numbers is generated between (0,1). These generated random numbers are compared with the measured electron efficiencies: pre-selection efficiency, H Matrix efficiency, trigger efficiency, and track match efficiency at phase space where electron generated. If the value of random number is larger than the specific efficiency in the phase space where generated electron located, this electron is discarded. By re-constructing the survived electrons to Z boson and comparing the re-constructed distribution to the distribution of generated Z boson, one can obtain a distribution of acceptance×efficiency of Z boson based on equation 5.4.

5.2.1 Vertex distribution

Since track match efficiency is correlated to z_{vtx}, z_{vtx} distribution needs to implement in the Monte Carlo simulation to get the accurate electron and track information. z_{vtx} distribution is also correlated to instantaneous luminosity. Since a lower instantaneous luminosity events have broader z_{vtx} distribution. The narrower z_{vtx} distribution is expected at high instantaneous luminosity events. FIG 5.1 indicates how the width of z_{vtx} changes as a function of the instantaneous luminosity. In the analysis, z_{vtx} distribution and z_{vtx} dependable track information with luminosity weight factor are implemented in the Monte Carlo simulation.

In the Monte Carlo simulation, the generated events are grouped into five subgroups of instantaneous luminosity. These subgroups are grouped in the following instantaneous luminosity:

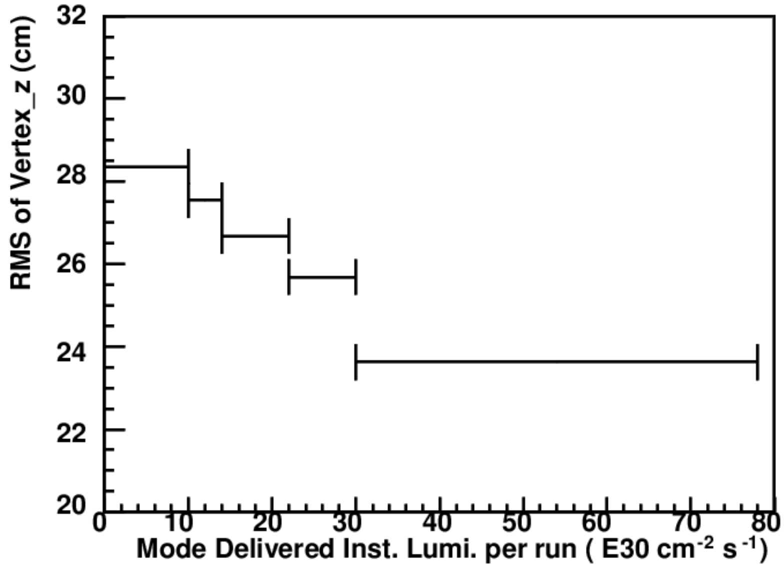

Figure 5.1: Width of vertex z distribution at 5 different groups of instantaneous luminosity.

- $0 < \mathcal{L}^{inst} < 10$ ($10^{30} cm^{-2} s^{-1}$);
- $10 < \mathcal{L}^{inst} < 14$ ($10^{30} cm^{-2} s^{-1}$);
- $14 < \mathcal{L}^{inst} < 22$ ($10^{30} cm^{-2} s^{-1}$);
- $22 < \mathcal{L}^{inst} < 30$ ($10^{30} cm^{-2} s^{-1}$);
- $30 < \mathcal{L}^{inst} < 78$ ($10^{30} cm^{-2} s^{-1}$);

Each subgroup accounts for about 90 pb^{-1} of events.

5.2.2 ϕ modular in central EM calorimeter

As described in Chapter 2, there are 50 ϕ modules in the central EM calorimeter. Electrons collected at boundaries of ϕ modules are to be shifted to center of the modules. Amount of boundary events shifted to central of module is corrected by *PMCS* based on the value measured from the data. As discussed in Section 3.4, the data collected within 15% of ϕ modular edge is cut off in Monte Carlo and the data. Those regions are added to acceptance cuts.

5.2.3 Electron energy re-construction

Electron energy re-construction used in the Monte Carlo simulation is based on the measured results from the same data used in this analysis. Electron energy leakage in electron shower, calorimeter energy response and energy resolution are the main considerations in the Monte Carlo simulation of the electron energy re-construction.

Electron energy response is determined by using a linear model together with earlier test beam data:

$$E^{reconstruct} = \alpha E^{measure} + \beta \tag{5.6}$$

where $E^{reconstruct}$ is the true electron energy. It depends on energy scale constant α and offset β.

Electron energy resolution is determined by measuring the width of Z mass peak obtained from the data. Resolution variables applied in the Monte Carlo simulation include a constant term c, a sampling term s and a noise term c, in the following format:

$$\sigma/E = \sqrt{c^2 + s^2/E + n^2/E^2} \tag{5.7}$$

Since invariant mass distribution of Z boson is not sensitive to the sampling term s and the noise term c, only scale, offset and constant terms are considered in this analysis. Difference between scale, offset and constant terms between data and the Monte Carlo simulation results are compared using a log likelihood method:

$$-2\Sigma[x_i ln(y_i) - y_i - ln(x_i!)] \tag{5.8}$$

to make sure the smeared Monte Carlo events match the data. In above equation, y_i is the i-th bin value from the Monte Carlo simulation and x_i is i-th bin value from the data. Only events within mass bins between 81 to 101 GeV are used in the fitting. Smearing processes start with CC region by requiring both electrons in CC. Events in EC1 and EC2 have the similar requirements,

	CC	*EC1*	*EC2*	*EC3*
α	1.00053 ± 0.00006	1.0205 ± 0.0003	1.0061 ± 0.0001	0.99252 ± 0.0001
β	0.419 ± 0.003	-1.4 ± 0.2	-0.80 ± 0.04	-0.8 ± 0.4
c	0.040 ± 0.003	0.039 ± 0.007	0.024 ± 0.006	0.026 ± 0.008

Table 5.1: Smearing parameters for Monte Carlo simulation at CC($0 < |\eta_D| < 0.9$), EC1($1.50 < |\eta_D| < 1.68$), EC2($1.68 < |\eta_D| < 2.50$) and EC3($2.50 < |\eta_D| < 3.20$)

except for those in EC3 region, which requires only one electron in EC3, another electron can be anywhere within EC due to only fewer events in EC3. After this step is done, further fine tune is performed for CC-EC events, and sub regions of EC. The final smearing constants are shown on Table 5.1.

5.2.4 Events purity

DØ detector has finite energy and angular resolution. Re-constructed Z boson in one rapidity bin could migrate to the neighboring bins due to the finite resolution. Events purity in given rapidity bin can help us understand this bin migration effect. Define purity:

$$Purity = \frac{n}{N}; \tag{5.9}$$

where n is number of Z bosons measured and generated in the bin. N is number of Z bosons measured in the bin. Events purity per rapidity bin is calculated as the following: Z/$\gamma^* \rightarrow e^+e^-$ events are generated with the Monte Carlo simulation. These electrons are applied with detector simulation and re-constructed to Z bosons. Events purity is calculated by comparing numbers between re-constructed Z boson and generated Z boson per rapidity bin.

FIG 5.2 shows the purity value per rapidity bin. Overall effect of events migrate to the neighboring bins is very small. There is about 5% of net events mirgate to the neighouring bins in average. The biggest effect is about 9%.

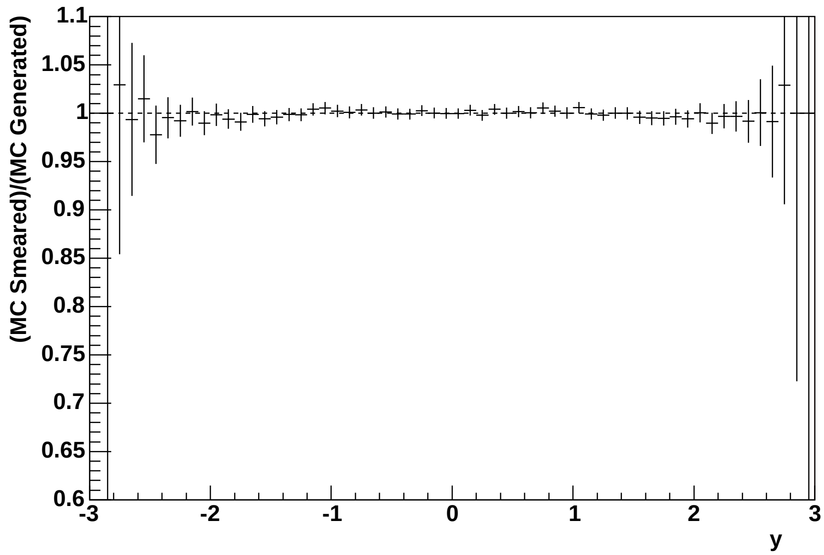

Figure 5.2: Ratio of re-constructed Monte Carlo events to generated Monte Carlo events

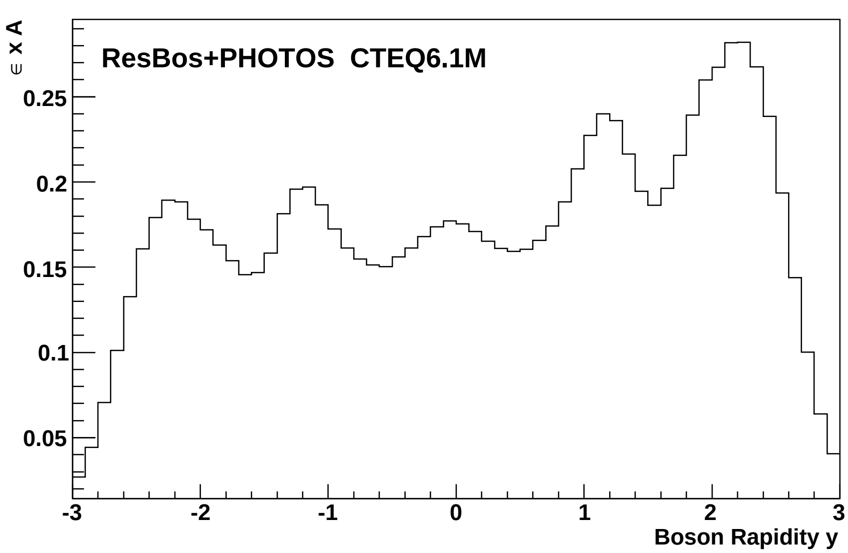

Figure 5.3: Efficiency×acceptance as function of rapidity of Z boson

5.3 Efficiency×acceptance

Based on equation 5.4, with proper Monte Carlo events generator and detector simulation, Z boson efficiency×acceptance is determined based on the measured electron efficiencies and acceptance cuts. The re-constructed Z events and generated Z events are plotted in 60 rapidity bins at bin width of 0.1. The ratio of Z events re-constructed to generated is the efficiency×acceptance of Z boson. This ratio is shown on FIG 5.3 as function of rapidity. Since most of bad calorimeter regions are located at negative η_D region, on FIG 5.3 we can see negative rapidity events have lower efficiency×acceptance than the positive rapidity events. There are also dips and valleys on the plot, these are due to inefficiency of ICD regions between $1.1 < |\eta_D| < 1.5$.

5.4 Data and Monte Carlo Comparison

The Monte Carlo simulation is critical in determining Z boson efficiency×acceptance. In order get precision result of rapidity analysis, it is necessary to verify the Monte Carlo events with the data.

First comparison is invariant mass distribution of Z boson. The electrons are separated to these from all η_D region, from CC-CC, CC-EC, and EC-EC regions. FIG 5.4 shows the invariant mass peak comparison plots. On the plots, the background is added to the Monte Carlo events instead of removing background events from data. The shapes of background used on these plots are obtained from di-jet events.

Invariant mass peaks of data and Monte Carlo simulated events from CC-CC, CC-EC and EC-EC match very well: CC-CC configuration has $\chi^2/ndf = 1.24$, which is the smallest, EC-EC configuration has $\chi^2/ndf = 2.00$, which is the highest. For CC-EC configuration, $\chi^2/ndf = 1.58$. Since all the electrons in CC are required to have track match but in EC region, events are only required to have at least one track match. Different amount of background is presented due to the different track requirement on data. This causes slight difference in data and Monte Carlo invariant mass peaks.

RESBOS with photon radiative correction from *PHOTOS* does a lot of improvement on Z boson P_T spectrum, especially for the high rapidity events. FIG 5.5 shows Z boson P_T spectrum of

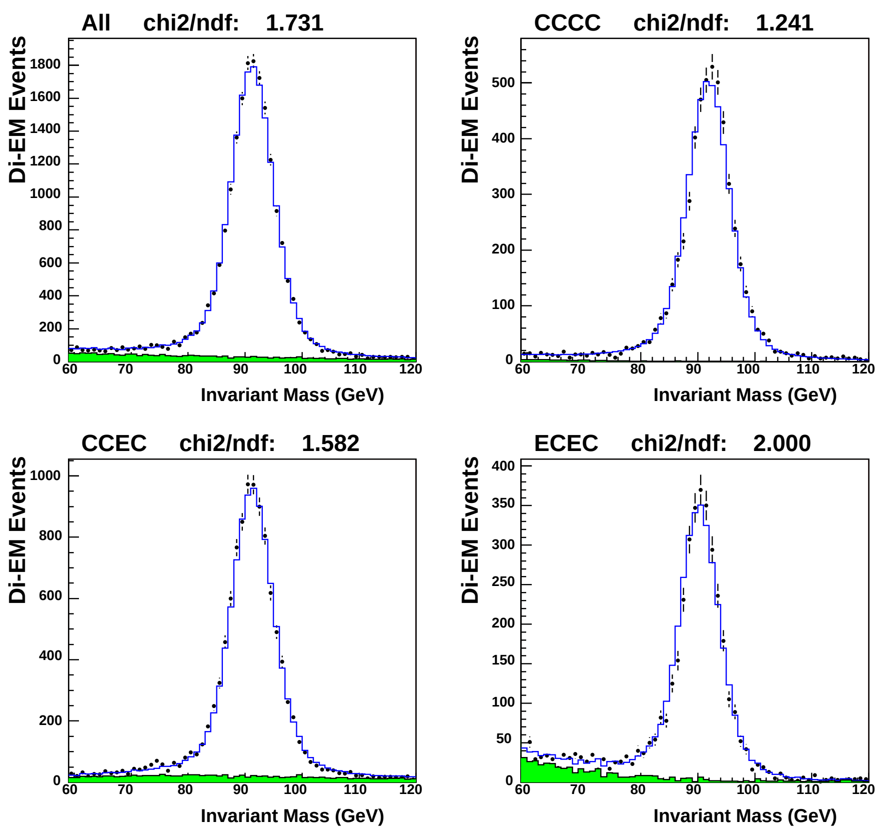

Figure 5.4: Data and Monte Carlo invariant mass comparison plots. Green: QCD background; Blue: Monte Carlo with QCD background added; Black: data

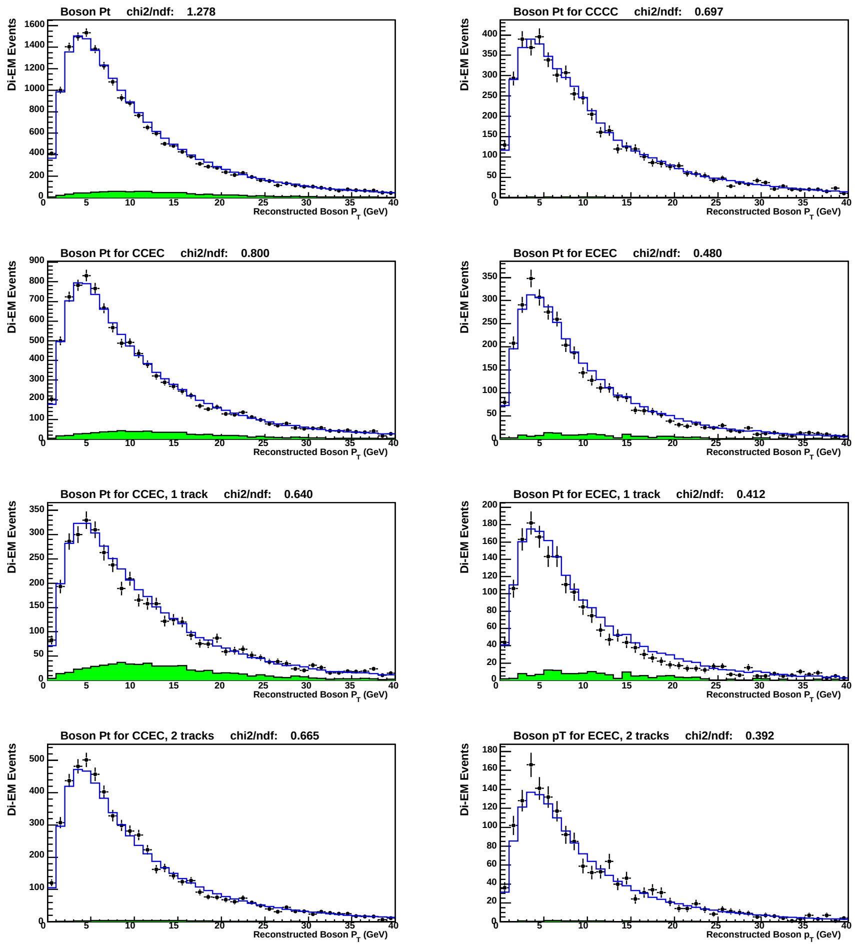

Figure 5.5: Data and Monte Carlo boson P_T comparison plots. Green: QCD background; Blue: Monte Carlo with QCD background added; Black: data

data and the Monte Carlo simulation, with different configurations: CCCC, CCEC, ECEC. Each event has at least one matched track. Those plots indicate data and Monte Carlo simulation in Z boson P_T spectrum match very well except P_T distribution for these events with only one track match. The difference is largely due to the background and low statistics. χ^2/ndf of data and Monte Carlo comparison of Z boson P_T spectrum distribution is also shown on each figure.

Electron energy E (FIG 5.6) and P_T (FIG 5.7) from data and Monte Carlo simulation are also compared at various configurations. Most of plots show data and Monte Carlo simulations are in good agreement, except for the electron E comparison at far forward region and electron P_T spectrum comparison for the electrons without track match. The reason of Monte Carlo simulation

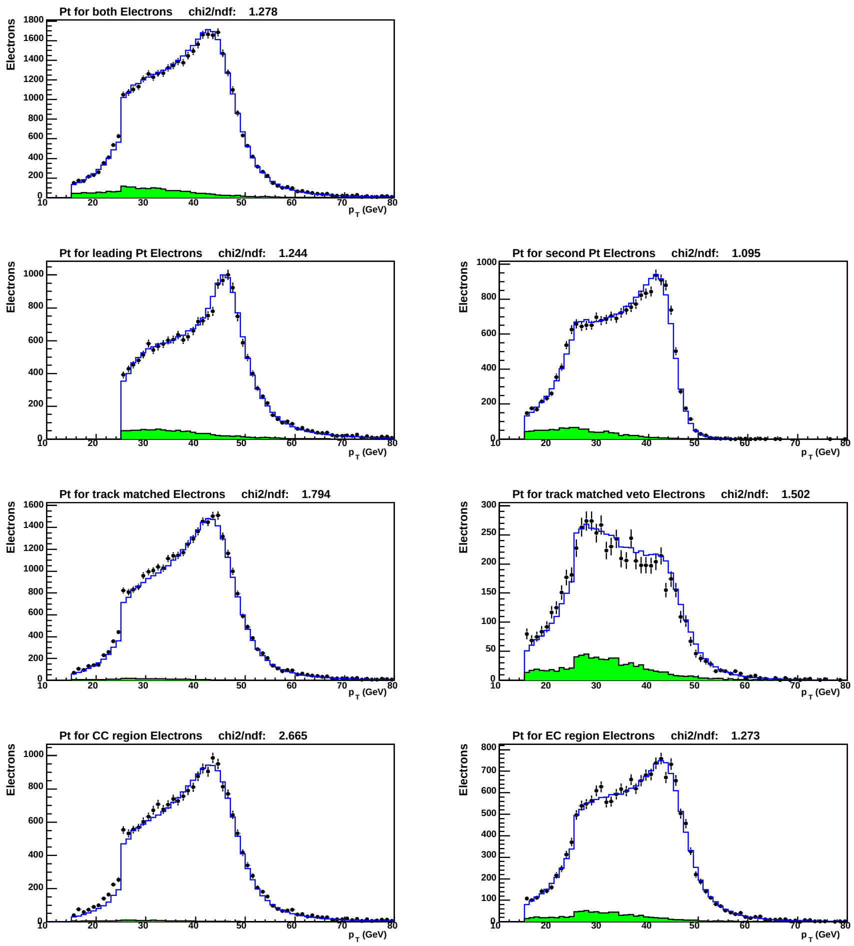

Figure 5.6: Data and Monte Carlo electron P_T comparison plots. Green: QCD background; Blue: Monte Carlo with QCD background added; Black: data

has slightly difference is mostly due to the background shape and low statistics in the data bins.

The data and Monte Carlo simulation also match very well in η_D comparison. FIG 5.8 shows η_D distribution of the leading and the secondary electrons with or without track match. Similar comparison plots are made in ϕ_D also. The electrons with track match match to Monte Carlo simulation very well. However, plot of electrons without track match shows there is excess events in data around $2/3\phi$. The reason of what causes this is not clear. Since only very small amount of events in this region, it is ignored in the analysis.

Since Monte Carlo simulation does not generate its own vertex distribution. the vertex distributions used in simulation are obtained from event vertex taken from data. Monte Carlo

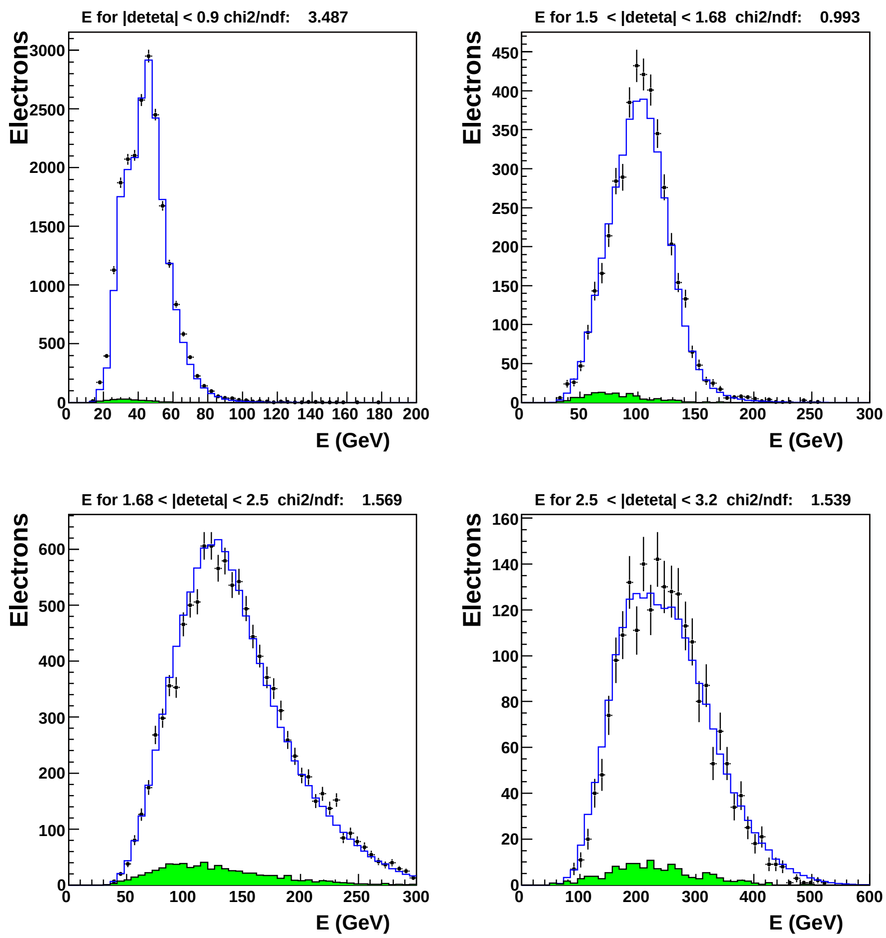

Figure 5.7: Data and Monte Carlo electron E comparison plots. Green: QCD background; Blue: Monte Carlo with QCD background added; Black: data

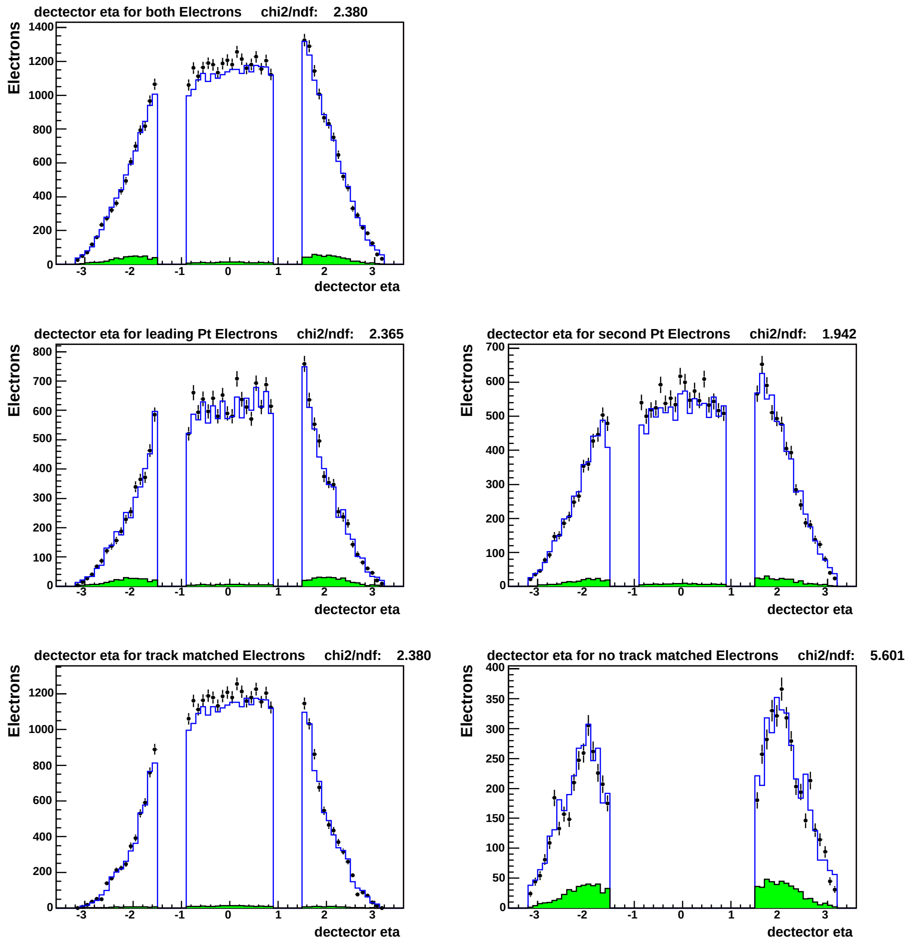

Figure 5.8: Data and Monte Carlo electron η_D comparison plots. Green: QCD background; Blue: Monte Carlo with QCD background added; Black: data

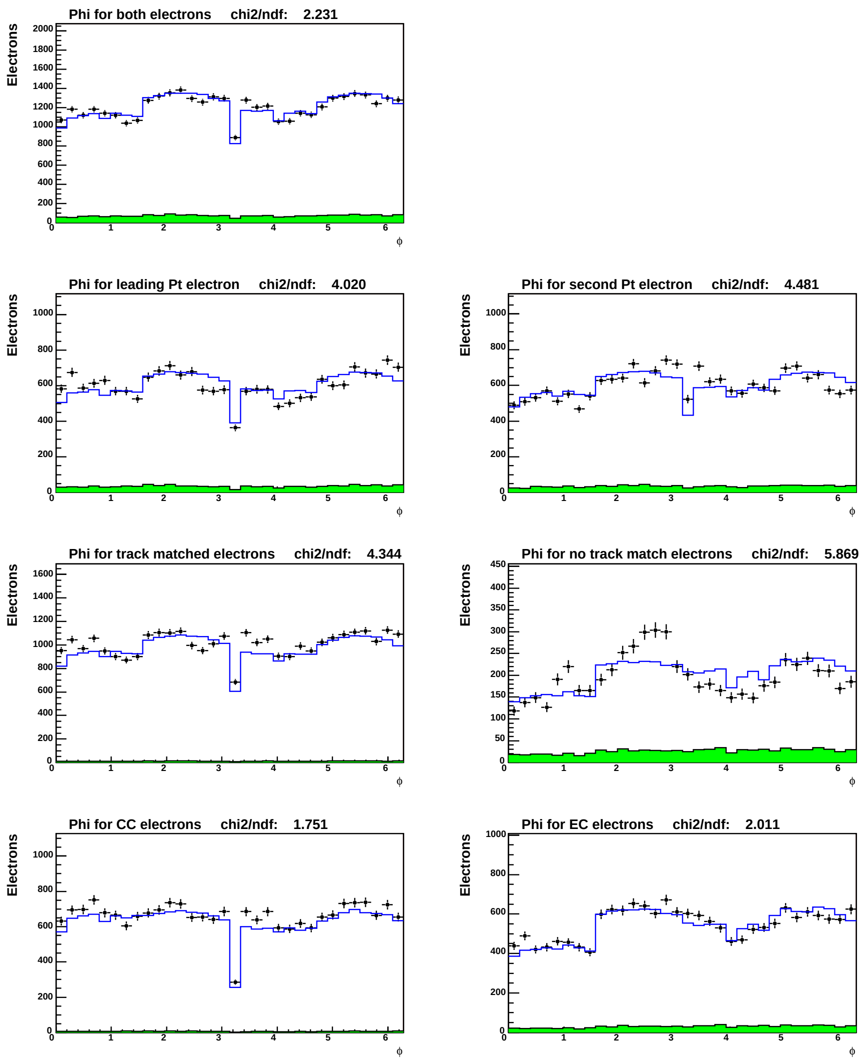

Figure 5.9: Data and Monte Carlo electron ϕ comparison plots. Green: QCD background; Blue: Monte Carlo with QCD background added; Black: data

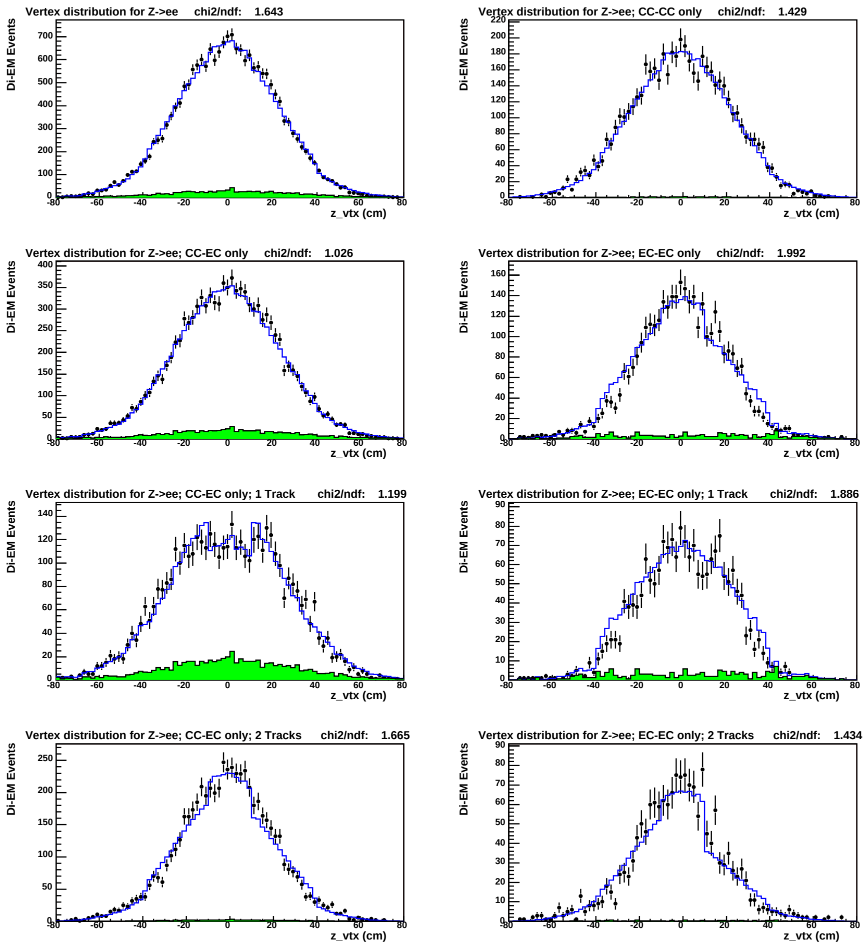

Figure 5.10: Data and Monte Carlo z_{vtx} comparison plots. Green: QCD background; Blue: Monte Carlo with QCD background added; Black: data

generated electrons are smeared with vertex distribution to determine η_D. FIG 5.10 shows the comparison between data and Monte Carlo simulation in vertex distribution.

χ^2 between the data and Monte Carlo simulation are shown on each plot.

5.5 Summary

This chapter the author discuss the method to determine Z boson efficiency due to selection cuts on the electrons. With the next to leading order *RESBOS* and radiative photon corrective from *PHOTOS*, the Monte Carlo simulations results match data very well. Z boson efficiency×acceptance as function of boson rapidity is determined by using the Monte Carlo simulation. Validity of the Monte Carlo simulation is also presented by comparing it to the data. Value of Z boson efficiency×acceptance per bin is listed on Table 5.5. Uncertainties of those value are addressed in Chapter 6.

Table 5.2: efficiency×acceptance per rapidity bin of Z boson

y bin	efficiency×acceptance	y bin	efficiency×acceptance
-2.95	0.0259	0.05	0.1757
-2.85	0.0439	0.15	0.1706
-2.75	0.0694	0.25	0.1651
-2.65	0.1019	0.35	0.1607
-2.55	0.1328	0.45	0.1591
-2.45	0.1608	0.55	0.1600
-2.35	0.1802	0.65	0.1660
-2.25	0.1891	0.75	0.1744
-2.15	0.1887	0.85	0.1881
-2.05	0.1781	0.95	0.2079
-1.95	0.1713	1.05	0.2276
-1.85	0.1624	1.15	0.2399
-1.75	0.1532	1.25	0.2362
-1.65	0.1462	1.35	0.2166
-1.55	0.1469	1.45	0.1947
-1.45	0.1590	1.55	0.1863
-1.35	0.1811	1.65	0.1967
-1.25	0.1963	1.75	0.2159
-1.15	0.1967	1.85	0.2382
-1.05	0.1867	1.95	0.2600
-0.95	0.1719	2.05	0.2675
-0.85	0.1614	2.15	0.2822
-0.75	0.1543	2.25	0.2821
-0.65	0.1512	2.35	0.2680
-0.55	0.1506	2.45	0.2376
-0.45	0.1562	2.55	0.1906
-0.35	0.1614	2.65	0.1437
-0.25	0.1678	2.75	0.0998
-0.15	0.1739	2.85	0.0641
-0.05	0.1772	2.95	0.0395

Chapter 6

Systematic Uncertainties

In this chapter the author focuses on sources of systematic uncertainties, and the method on how to estimate Z boson systematic uncertainties from those sources. Overall systematic uncertainties are presented at the end of this chapter.

6.1 Method

Systematic uncertainties of Z boson come from several sources: uncertainty from efficiency measurements, from parton distribution function used in Monte Carlo events generator, from Z boson P_T distribution due to difference between the next to leading order Monte Carlo model and the real data, from background removing method used in counting number of Z events, from vertex distribution and from calorimeter electromagnetic energy scale calibration.

Suppose ε_e is electron efficiency. If systematic uncertainty of ε_e is $\Delta\varepsilon_e$. To determine systematic uncertainty of efficiency×acceptance due to $\Delta\varepsilon_e$. Equation 5.3 is slightly modified to:

$$H^{upper}(\rho_{xi}) = \begin{cases} 1 & \text{if } \rho_{xi} \leq \varepsilon_e(x_i) + \Delta\varepsilon_e(x_i), \\ 0 & \text{if } \rho_{xi} > \varepsilon_e(x_i) + \Delta\varepsilon_e(x_i). \end{cases} \tag{6.1}$$

where $H^{upper}(\rho_{xi})$ is the upper bound of $H(\rho_{xi})$ due to systematic uncertainty on ε_e measurement. Similarly one can find the lower bound of $H(\rho_{xi})$:

$$H^{lower}(\rho_{xi}) = \begin{cases} 1 & \text{if } \rho_{xi} \leq \varepsilon_e(x_i) - \Delta\varepsilon_e(x_i), \\ 0 & \text{if } \rho_{xi} > \varepsilon_e(x_i) - \Delta\varepsilon_e(x_i). \end{cases} \tag{6.2}$$

The distribution of ρ_{xi} is based on method to measure uncertainties of each individual source. In this analysis, Binomial distribution is used in estimating systematic uncertainties from all efficiencies except the pre-selection efficiency. In determine uncertainty from the pre-selection efficiency, a combination of $Poisson$ distribution (on events counting) and $Gaussian$ distribution (on charge mis-identification) is used.

The systematic uncertainty of efficiency×acceptance propagated from $\Delta\varepsilon_e$ is determined by comparing how much efficiency×acceptance changed after using equation 6.1 for the upper bound and equation 6.2 for the lower bound in Monte Carlo simulation. Below is the steps used in Monte Carlo simulation:

- Get systematic uncertainties from each individual source;
- Randomly shift value of each individual source within its systematic uncertainties;
- Determine systematic uncertainty of efficiency×acceptance by comparing the change of efficiency×acceptance due to shifting of each individual source.

6.2 Results

6.2.1 From PDF uncertainty

Monte Carlo events generator uses central value of CTEQ6M PDF set. However, CTEQ6M PDF itself relies on the data from various experiments. It has 20 eigen values [9]. For each observable, define difference:

$$\Delta X = \frac{1}{2}(\sum_{i=1}^{N_p}[X(S_i^+) - X(S_i^-)]^2)^{1/2} \tag{6.3}$$

where X is the observable, $X(S_i^{\pm})$ is the predication for X based on the PDF set $S_i^{\pm}$. By shifting 1σ of these 20 eigen values, we have total 40 variations. Each variation corresponds to one variable shifted 1σ away from its central value. In order to determine PDF uncertainties in this analysis, the 40 variations of CTEQ6M PDF are used separately by the Monte Carlo generator. The relative difference of observable from different variation of PDF:

$$\delta X = \frac{X(S') - X(S^0)}{X(S^0)} \tag{6.4}$$

is calculated. Here $X(S')$ is one PDF variation to the central PDF and $X(S^0)$ is the central PDF. FIG 6.1 shows the uncertainties from 40 variations of PDF sets to central value of CTEQ6M PDF.

6.2.2 From Efficiency Measurement

Method to determine statistical and systematic uncertainties of efficiency×acceptance from the efficiency measurement is similar to those used in determining efficiency of Z boson. Each individual efficiency value ε is shifted to $\varepsilon \pm \delta\varepsilon$, as described in Section 6.1. $\delta\varepsilon$ is either statistical or systematic uncertainty of ε. The value of ε is shifted randomly between $\pm\delta\varepsilon$. The distribution of randomly shifted value between $\pm\delta\varepsilon$ is binomial except for the pre-selection efficiency, which is:

$$\rho(\varepsilon) = \frac{(d+1)!}{n!(d-n)!}\varepsilon^n (1-\varepsilon)^{d-n} \tag{6.5}$$

due to the different method used in determining pre-selection efficiency. Based on inputs to pre-selection efficiency, *Poisson* distribution is used in the same sign or opposite sign events counting and *Gaussian* distribution is used in charge mis-identification rate.

The statistical uncertainties from efficiency measurement is determined by counting how many events changed after shifting input efficiency within statistical uncertainties of each value. FIG 6.2 shows the distribution of statistical uncertainty of efficiency×acceptance due to each of measured electron efficiencies.

Background subtraction and *tag-and-probe* method are contributions to systematic uncertainties of efficiency×acceptance. FIG 6.3 shows the distribution of systematic uncertainties of efficiency×acceptance due to systematic uncertainties on each electron efficiency.

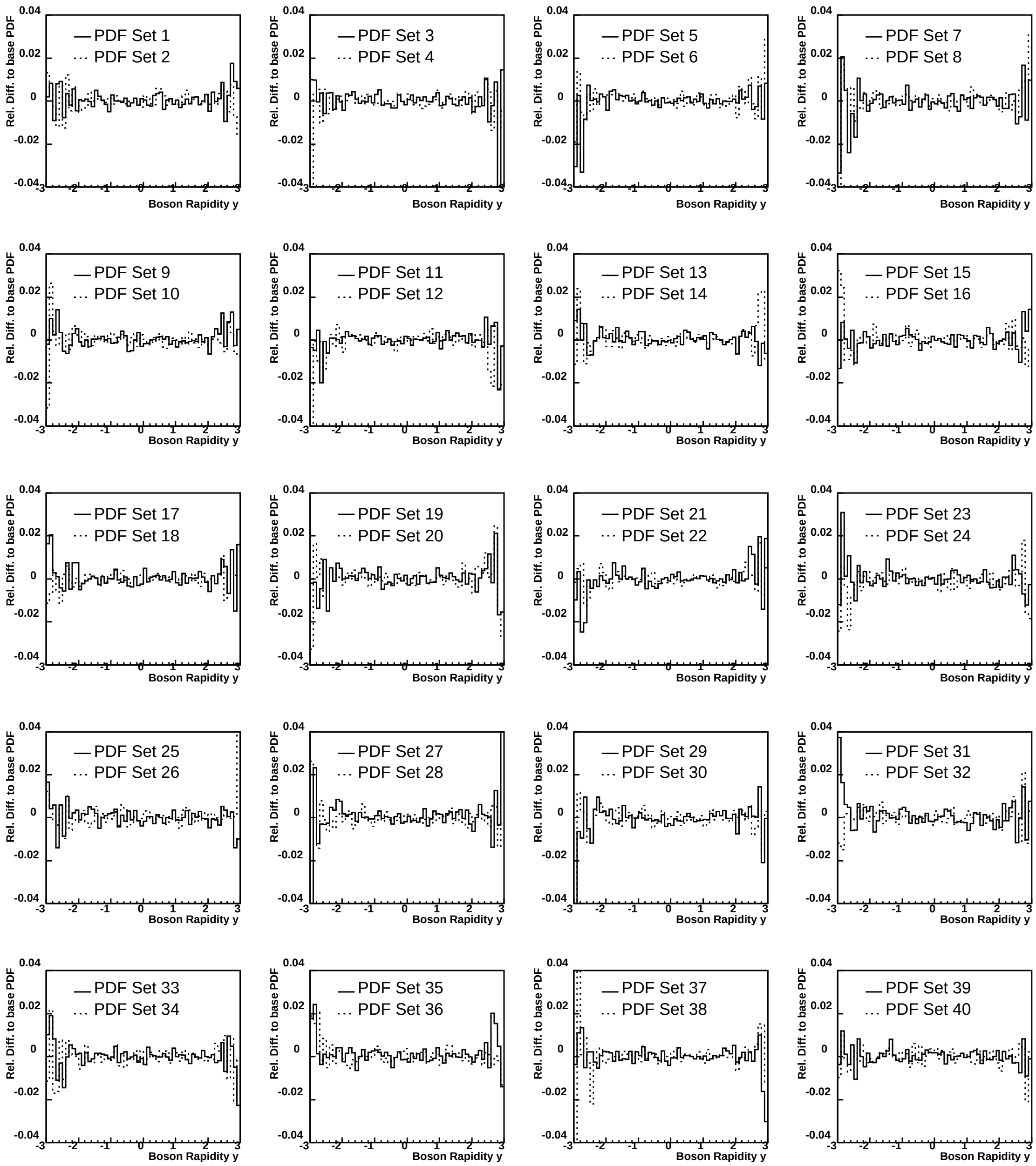

Figure 6.1: Contributions to the PDF uncertainty on the efficiency×acceptance of Z boson. Each plot shows the relative difference of efficiency×acceptance after the PDF shifted 1σ away from its central PDF.

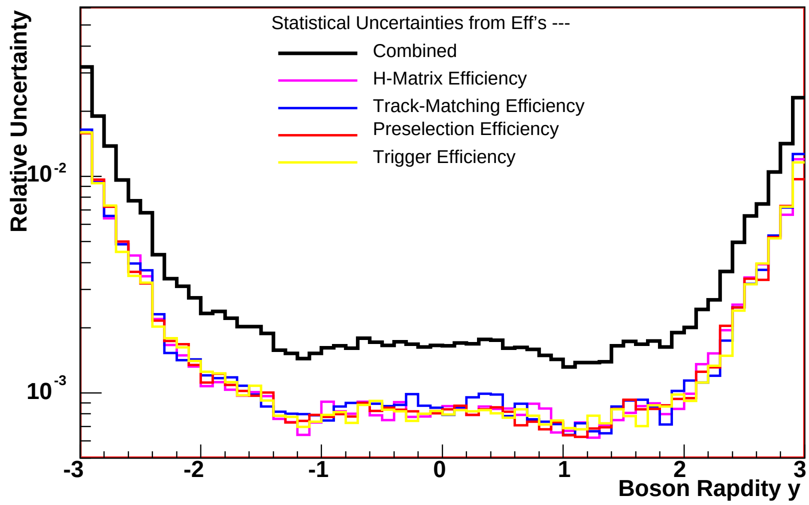

Figure 6.2: Statistical uncertainties on efficiency×acceptance due to statistical uncertainty in individual electron efficiencies.

6.2.3 From P_T distribution

Uncertainty from Z boson P_T distribution is mainly due to the Monte Carlo generator. It depends on how the Monte Carlo generator models the initial state radiation, parton process, and transverse momentum. Since $RESBOS$ provides better simulation on WZ physics, and the final state radiation is also corrected by $PHOTOS$. Uncertainty from P_T distribution is small enough that can be neglected.

6.2.4 From z_{vtx} distribution

Systematic uncertainty from z_{vtx} distribution is estimated by choosing different group of z_{vtx} distributions measured at different luminosity range. There are three groups of z_{vtx}: z_{vtx} obtained from two electrons passing loose ID cuts, from inclusive jet sample and from event vertex associated with two loose electrons both have H Matrix 8 less than 30. Different values of efficiency×acceptance are observed by choosing different z_{vtx} distributions. Systematic uncertainty from z_{vtx} distribution is determined by comparing the differences at efficiency×acceptance due to using different groups of z_{vtx} distribution.

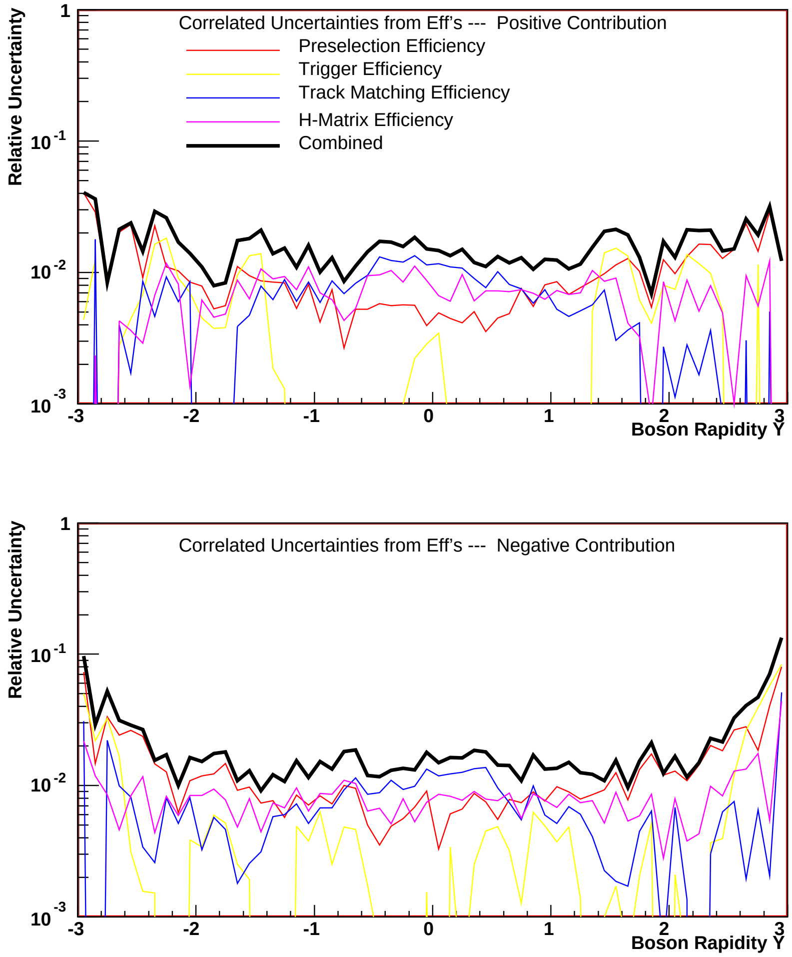

Figure 6.3: Systematic uncertainties on efficiency×acceptance due to systematic uncertainty in individual electron efficiencies.

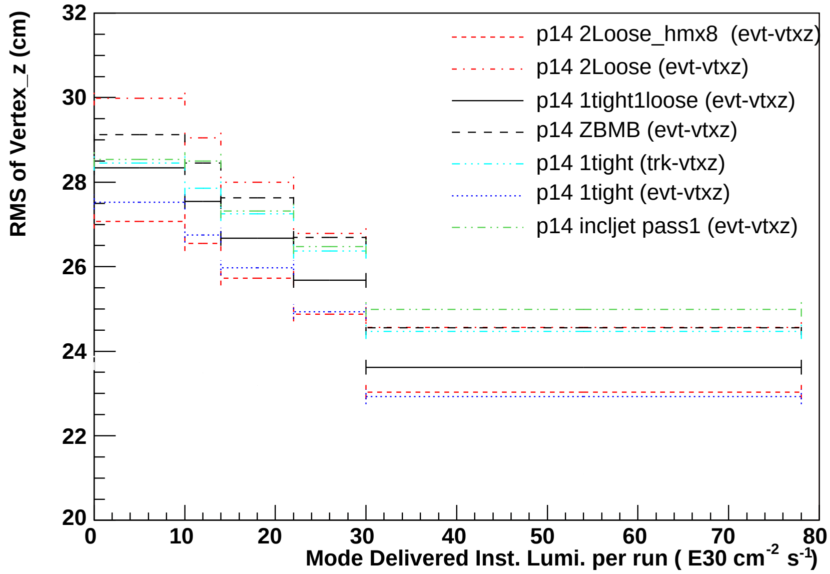

Figure 6.4: RMS value of vertex z distribution at different of instantaneous luminosity. Each instantaneous luminosity bin corresponds to about 90 pb $^{-1}$ delivered luminosity.

	CC	*EC1*	*EC2*	*EC3*
c	0.031 ± 0.001	0.028 ± 0.002	0.029 ± 0.002	0.022 ± 0.002
s	-	0.322 ± 0.002	0.293 ± 0.002	0.228 ± 0.006

Table 6.1: Alternative constant term c and sampling term s for Monte Carlo simulation at CC($0 < |\eta_D| < 0.9$), EC1($1.50 < |\eta_D| < 1.68$), EC2($1.68 < |\eta_D| < 2.50$) and EC3($2.50 < |\eta_D| < 3.20$)

6.2.5 From electromagnetic energy resolution and energy scale

In order to determine systematic uncertainty from electron energy resolution, an alternative constant c and sampling s terms (equation 5.7) are used [24]. New values based on alternative method are shown on Table 6.1. The difference on efficiency×acceptance between default Table 5.1 and alternative Table 6.1 is found very small and it does not contribute to systematic uncertainty of efficiency×acceptance. FIG 6.5 shows the difference.

To evaluate uncertainty from electron energy scale, in addition to the standard energy scale parameters on Table 5.1, an alternative α term (Table 6.2) is obtained by using electrons from both CC and EC regions. The difference at efficiency×acceptance due to using different α terms is shown on FIG 6.6.

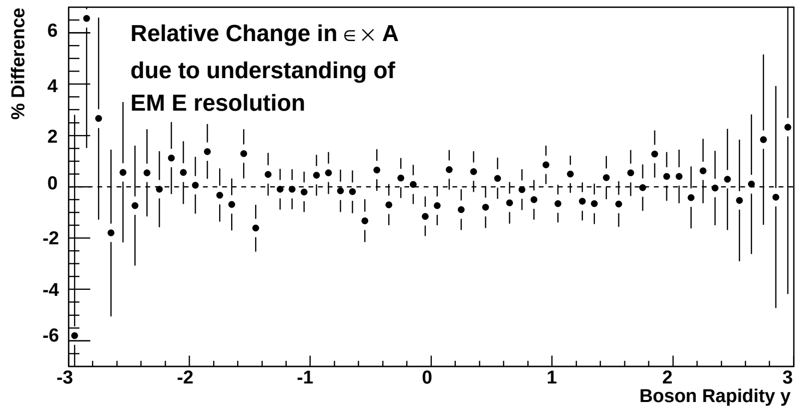

Figure 6.5: Difference at efficiency×acceptance due to alternative constant and sampling terms in the Monte Carlo.

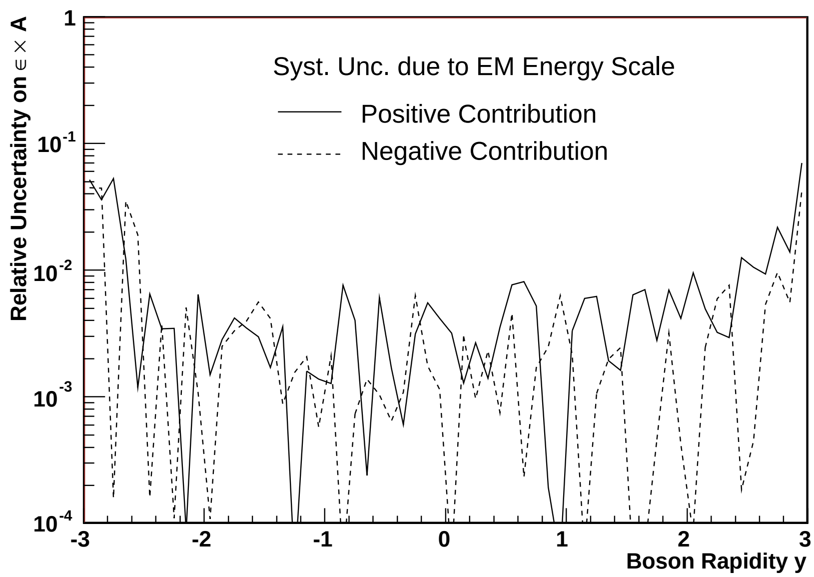

Figure 6.6: Difference at efficiency×acceptance due to uncertainty in electron energy scale.

	CC	*EC1*	*EC2*	*EC3*
α	0.99746 ± 0.00009	1.0154 ± 0.0001	1.00261 ± 0.00004	0.9971 ± 0.0002

Table 6.2: Alternative α term obtained by using electrons from both CC and EC regions, where CC($0 < |\eta_D| < 0.9$), EC1($1.50 < |\eta_D| < 1.68$), EC2($1.68 < |\eta_D| < 2.50$) and EC3($2.50 < |\eta_D| < 3.20$)

6.3 Summary

Various sources of uncertainties contribute to efficiency×acceptance measurement are combined. FIG 6.7 shows the upper and lower relative uncertainties and the contribution from different sources to the total uncertainties of efficiency×acceptance.

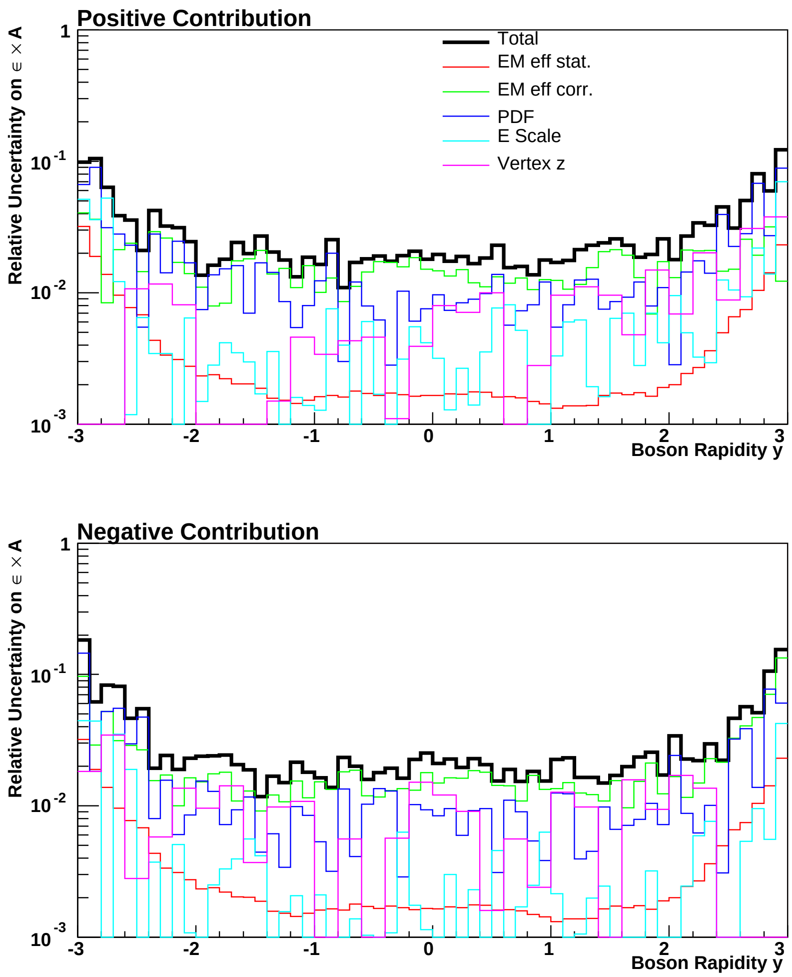

Figure 6.7: Relative systematic uncertainty on efficiency×acceptance as a function of Z boson rapidity.

Chapter 7

$1/\sigma d\sigma/dy$ Measurement [33]

Differential cross section of Z boson between 71 to 111 GeV invariant mass window is calculated with the following equation:

$$\frac{\mathrm{d}\sigma\left(Z/\gamma^{*}\rightarrow e^{+}e^{-}\right)}{\mathrm{d}y}=\frac{N_{i}^{obs}-N_{i}^{bkgd}}{\Delta_{i}\left(\epsilon A\right)_{i}\mathcal{L}}, \tag{7.1}$$

where Δ_i is the bin width. $(\epsilon A)_i$ is efficiency$\times$acceptance of Z boson in each rapidity bin being measured. $\mathcal{L}$ is integrated luminosity for total data used. $N_i^{obs} - N_i^{bkgd}$ is number of Z boson in rapidity bin i, which is the total observed events per bin minus the background events in the same bin.

Due to large uncertainty associated with the current $D\O$ luminosity measurement, ratio of differential cross section $1/\sigma d\sigma/dy$ is presented instead of the differential cross section $d\sigma/dy$.

7.1 Z events and backgrounds

7.1.1 Background sources

The background in this analysis comes from the following sources:

1. Multi-jet event where jets are mis-identified as electrons;
2. WZ event, with W $\rightarrow$ all and Z $\rightarrow e^+e^-$;
3. $W^+W^- \rightarrow e^+e^-\ \nu_e\ \bar{\nu}_e$, invariant mass of electron pair is within 71 to 111 GeV mass window of Z boson;
4. $Z/\gamma^* \rightarrow \tau^+\tau^- \rightarrow e^+e^-\nu_\tau\nu_e\bar{\nu}_\tau\bar{\nu}_e$;
5. $W\gamma$, where W decays to electron, neutrino and photon is mis-identified as an electron.

7.1.2 Multi-jet background

Background subtraction method described in Section 4.2 is used to remove background from multi-jet events. When removing background, bin-by-bin background subtraction method is used for the bins with boson rapidity less than 2.0. Two types of background shapes are used in the bin-by-bin method: The standard background shape is obtained from di-jet events and it is binned in rapidity with width of 0.1. The second type of background shape uses exponential curve. This type of background shape is used to estimate systematic uncertainty from the fitting method.

Comparing to the bins with rapidity less than 2.0, high rapidity bins have fewer events per bin. The bin-by-bin method fails due to no enough events per bin to perform a reasonable fitting. In this case, the ratio method is used. When the ratio method is used, total events are grouped into six separated configurations: CCEC South-South, North-North, and the rest of CCEC events, ECEC South-South, North-North, and the rest of ECEC events. The background for each of above group is fitted separately. In the fitting, both signal and background shapes are taken from the same fitting regions. Since CCCC events are mainly with rapidity less than 2.0, it is not used in the ratio method. The background fraction is assumed to be a constant over each of the six configurations. The number of background for bins with rapidity larger than 2.0 is determined by counting how many events fall into each of the above six configurations, and then obtain the number of background in that bin by applying background ratio on number of events found in each of their respective configurations.

Distributions of fitted background, signal from Monte Carlo simulation, and data are plotted for each calorimeter region on FIG 7.2. The distributions of background from different sources are plotted as a function of rapidity on FIG 7.1. The background fraction for each combination is given on Table 7.1, where CC-CC configuration is shown but not used in the ratio method.

7.1.3 Other sources of background

The other physics processes listed below also contribute to the background. Estimation of these background processes are done by the Monte Carlo simulations:

Region	Fraction(%)
CCCC North North	0.31
CCCC South South	0.35
CCCC Other	0.48
CCEC North North	4.67
CCEC South South	6.97
CCEC Other	8.01
ECEC North North	5.18
ECEC South South	4.64
ECEC Other	0
ALL	5.73

Table 7.1: Background fractions for events collected in different calorimeter regions.

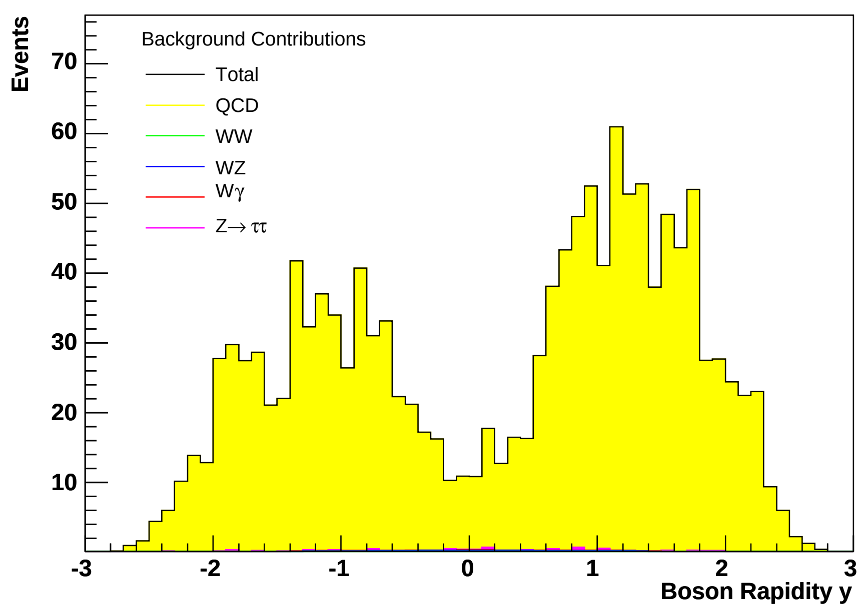

Figure 7.1: Distribution of background from different sources.

Processes	$\sigma Br(mb)$	*K factor*	*generator and cuts*	*number of background events*
WZ$\rightarrow$ all+e^+e^-	8.755×10^{-11}	1.35	PYTHIA	6.4
WW$\rightarrow$ $e^+\nu e^-\nu$	1.015×10^{-10}	1.31	PYTHIA	2.3
Z$\gamma^* \rightarrow \tau\tau$	5.012×10^{-6}	1.375	PYTHIA, Taula	3.8
W$\gamma \rightarrow e\nu\gamma$	3.519×10^{-8}	1.36	MCbyHand	0.8

Table 7.2: Other sources of backgrounds, where k factors are from reference [26], [28], [29], [30], and [15], cross section is calculated using PYTHIA [25], except $W\gamma$ [31]

1. WZ $\rightarrow$ all+e^+e^-: using PYTHIA, with Z decays in electron channel, but W can decay to all possible decay channels;

2. $W^+W^- \rightarrow e^+e^-\nu_e\bar{\nu}_e$: using PYTHIA, with W decays to electron channel;

3. $Z \rightarrow \tau^+\tau^- \rightarrow e^+e^-\nu_\tau\nu_e$, using PYTHIA, TAULA is used in τ decay to electron channel.

Since it is difficult to directly measure the rate of photon mis-identified as a track versus rapidity, the background contribution from $W\gamma$ events is estimated by replacing photon with electron in $W\gamma$ Monte Carlo sample and obtain an upper limit of $W\gamma$ background. When replacing photon with electron, 6% upper limit of photon mis-identification rate [27] is applied. The estimated upper limit of $W\gamma$ background events, with all efficiencies and acceptance applied, is about 0.8 event. Table 7.2 shows more details.

Because the backgrounds from sources other than multi-jet events are small, only multi-jet background is considered in estimating systematic uncertainty from background. This part of systematic uncertainty is estimated by using fixed signal amplitude method, and by using exponential background shape in the fitting. When fixed signal amplitude method is used, fixed signal amplitude is obtained by fitting events all together in one bin, then apply fixed signal amplitude in each fitting. Comparing to the floating signal amplitude results, the difference from fixed signal amplitude fitting is very small. When exponential background shape is used, the amount of background is increased roughly by 13%. In each bin, half of the difference of background from two methods are added to default background as standard background. The remainder of the difference of two methods is used as uncertainty. Table 7.3 shows the distribution of all backgrounds and their uncertainties.

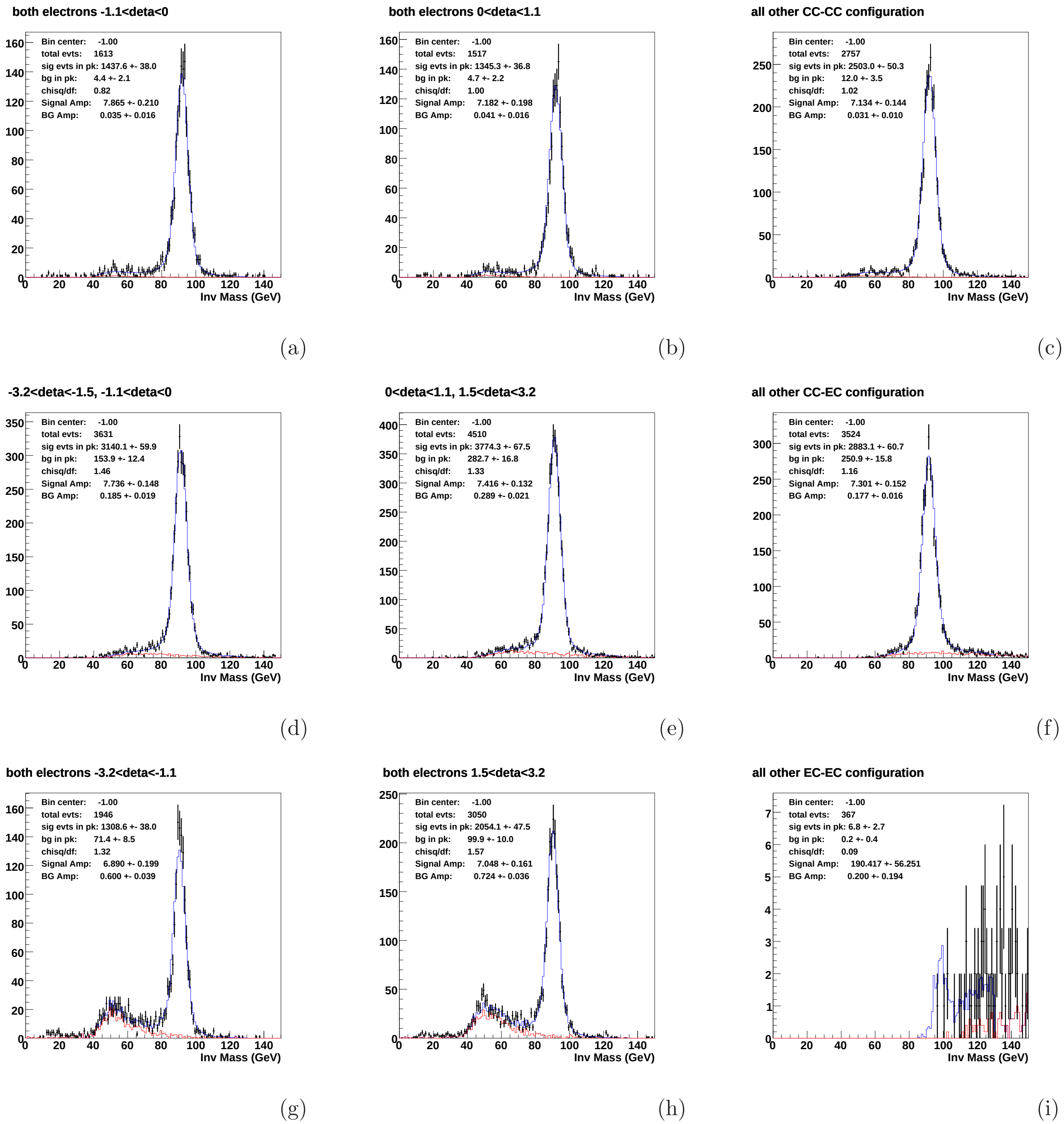

Figure 7.2: Fits to data used to determined background subtraction. Background is determined for CCCC North-North (a), South-South (b), other configuration CCCC (c); CCEC North-North (d), South-South (e), other configuration CCEC (f) and ECEC North-North (g), South-South (h), other configuration ECEC (i)

Table 7.3: Background events and systematic uncertainty

y	WW	WZ	$\tau\tau$	Wγ	jets	SysErr	y	WW	WZ	$\tau\tau$	Wγ	jets	SysErr
-2.95	0.0	0.0	0.0	0.0	0.0	0.0	0.05	0.1	0.2	0.1	0.0	10.4	2.1
-2.85	0.0	0.0	0.0	0.0	0.0	0.0	0.15	0.1	0.2	0.4	0.0	17.1	3.3
-2.75	0.0	0.0	0.0	0.0	0.2	0.0	0.25	0.1	0.2	0.0	0.0	12.4	2.1
-2.65	0.0	0.0	0.0	0.0	1.0	0.2	0.35	0.1	0.2	0.0	0.0	16.2	1.1
-2.55	0.0	0.0	0.0	0.0	1.7	0.3	0.45	0.1	0.2	0.1	0.0	15.9	2.2
-2.45	0.0	0.0	0.0	0.0	4.4	0.8	0.55	0.1	0.2	0.0	0.0	27.9	2.7
-2.35	0.0	0.0	0.2	0.0	5.8	0.9	0.65	0.1	0.2	0.2	0.0	37.7	3.7
-2.25	0.0	0.0	0.0	0.0	10.2	2.2	0.75	0.1	0.2	0.0	0.0	43.1	4.2
-2.15	0.0	0.0	0.0	0.0	13.8	3.0	0.85	0.1	0.2	0.5	0.0	47.4	5.6
-2.05	0.0	0.0	0.0	0.0	12.8	1.2	0.95	0.1	0.2	0.0	0.0	52.2	5.4
-1.95	0.0	0.1	0.2	0.0	27.6	3.1	1.05	0.1	0.2	0.3	0.0	40.6	3.3
-1.85	0.0	0.1	0.3	0.0	29.4	2.2	1.15	0.1	0.2	0.0	0.0	60.7	8.2
-1.75	0.0	0.1	0.0	0.0	27.4	4.1	1.25	0.1	0.2	0.0	0.0	51.1	5.5
-1.65	0.0	0.1	0.2	0.0	28.5	1.7	1.35	0.0	0.1	0.0	0.0	52.6	4.1
-1.55	0.0	0.1	0.0	0.0	21.0	2.3	1.45	0.0	0.1	0.0	0.0	37.8	2.4
-1.45	0.0	0.1	0.1	0.0	21.9	1.9	1.55	0.0	0.1	0.2	0.0	48.1	5.4
-1.35	0.0	0.1	0.0	0.0	41.6	4.3	1.65	0.0	0.1	0.0	0.0	43.5	5.1
-1.25	0.0	0.1	0.2	0.0	31.9	2.4	1.75	0.0	0.1	0.2	0.0	51.7	6.3
-1.15	0.1	0.2	0.0	0.0	36.8	2.3	1.85	0.0	0.1	0.1	0.0	27.3	5.4
-1.05	0.1	0.2	0.1	0.0	33.7	3.8	1.95	0.0	0.1	0.2	0.0	27.5	3.8
-0.95	0.1	0.2	0.0	0.0	26.2	1.6	2.05	0.0	0.1	0.0	0.0	24.4	5.7
-0.85	0.1	0.1	0.0	0.0	40.5	3.7	2.15	0.0	0.0	0.0	0.0	22.4	5.6
-0.75	0.1	0.2	0.3	0.0	30.6	1.9	2.25	0.0	0.0	0.0	0.0	23.0	5.7
-0.65	0.1	0.2	0.0	0.0	32.9	2.9	2.35	0.0	0.0	0.0	0.0	9.4	2.1
-0.55	0.1	0.2	0.0	0.0	22.1	3.6	2.45	0.0	0.0	0.0	0.0	6.0	1.2
-0.45	0.1	0.2	0.0	0.0	20.9	3.7	2.55	0.0	0.0	0.0	0.0	2.3	0.4
-0.35	0.1	0.2	0.0	0.0	16.9	2.8	2.65	0.0	0.0	0.0	0.0	1.3	0.2
-0.25	0.1	0.2	0.0	0.0	16.0	2.1	2.75	0.0	0.0	0.0	0.0	0.4	0.1
-0.15	0.1	0.2	0.2	0.0	9.8	2.5	2.85	0.0	0.0	0.0	0.0	0.0	0.0
-0.05	0.1	0.2	0.1	0.0	10.5	2.5	2.95	0.0	0.0	0.0	0.0	0.0	0.0

FIG 7.3 shows distribution total events, background and Z boson in each rapidity bin.

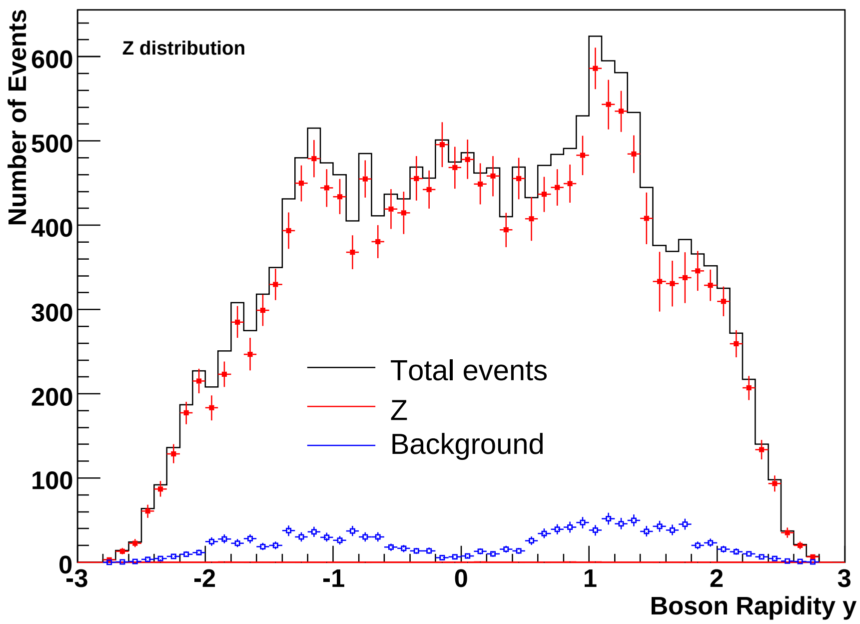

Figure 7.3: Distribution of total events, background and Z boson as function of boson rapidity y.

7.2 $1/\sigma d\sigma/dy$

Ratio of differential cross section of Z boson is determined by:

$$\begin{aligned} \frac{1}{\sigma}\frac{d\sigma(Z/\gamma^* \to e^+e^-)}{dy} &= \frac{1}{\sigma}\frac{N_i^{obs} - N_i^{bkgd}}{\Delta_i(\varepsilon \times A)_i \mathcal{L}} \\ &= \frac{(\varepsilon \times A)_{average}}{N_{total}^{obs} - N_{total}^{bkgd}} \frac{N_i^{obs} - N_i^{bkgd}}{\Delta_i(\varepsilon \times A)_i} \end{aligned} \tag{7.2}$$

Uncertainty of $1/\sigma d\sigma(Z/\gamma^* \to e^+e^-)/dy$ is determined by the following equation:

$$\frac{\delta(\frac{1}{\sigma}\frac{d\sigma}{dy})}{(\frac{1}{\sigma}\frac{d\sigma}{dy})} = \sqrt{\frac{N_i^{obs} + N_i^{bkgd}}{(N_i^{obs} - N_i^{bkgd})^2} + (\frac{\delta(\varepsilon \times A)_i}{(\varepsilon \times A)_i})^2 + (\frac{\delta_i^{bkgd\_sys}}{N_i^{obs} - N_i^{bkgd}})^2} \tag{7.3}$$

Number of observed events within 71 to 111 GeV invariant mass window per rapidity bin y is listed on Table 3.8. Using equation 7.2, $1/\sigma d\sigma/dy$ value per bin are listed on Table 7.4 and

7.5. Uncertainties per bin are also calculated using equation 7.3. FIG 7.4 shows the ratio of the differential cross section distribution between -3 to 3 of rapidity of Z boson.

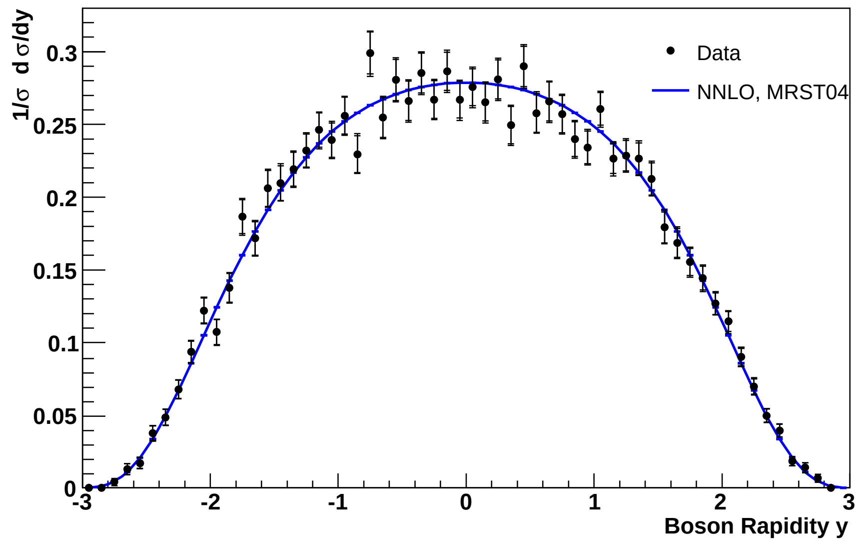

Figure 7.4: Ratio of differential cross section of $Z/\gamma^* \rightarrow e^+e^-$

Since Z boson differential cross section distribution is symmetry over rapidity. negative part of FIG 7.4 can be folded over. When folding over, bin center is adjusted based on method by Lafferty, et al [32]. First the data points of $1/\sigma(d\sigma/dy)_i$ from measurement is fitted with an $8th$ polynomial:

$$g(x) = p_0 + p_1 x + p_2 x^2 + ... + p_8 x^8; \tag{7.4}$$

where x correspondents to rapidity y and g(x) correspondents to differential cross section in this analysis. When data is measured in *large width*, the appropriate value of x_{lw} is equal to:

$$g(x_{lw}) = \frac{1}{\Delta x} \int_{x_1}^{x_2} g(x)dx \tag{7.5}$$

Table 7.6 shows the fitting parameters p_i. FIG 7.5 shows the folded over differential cross section of Z boson.

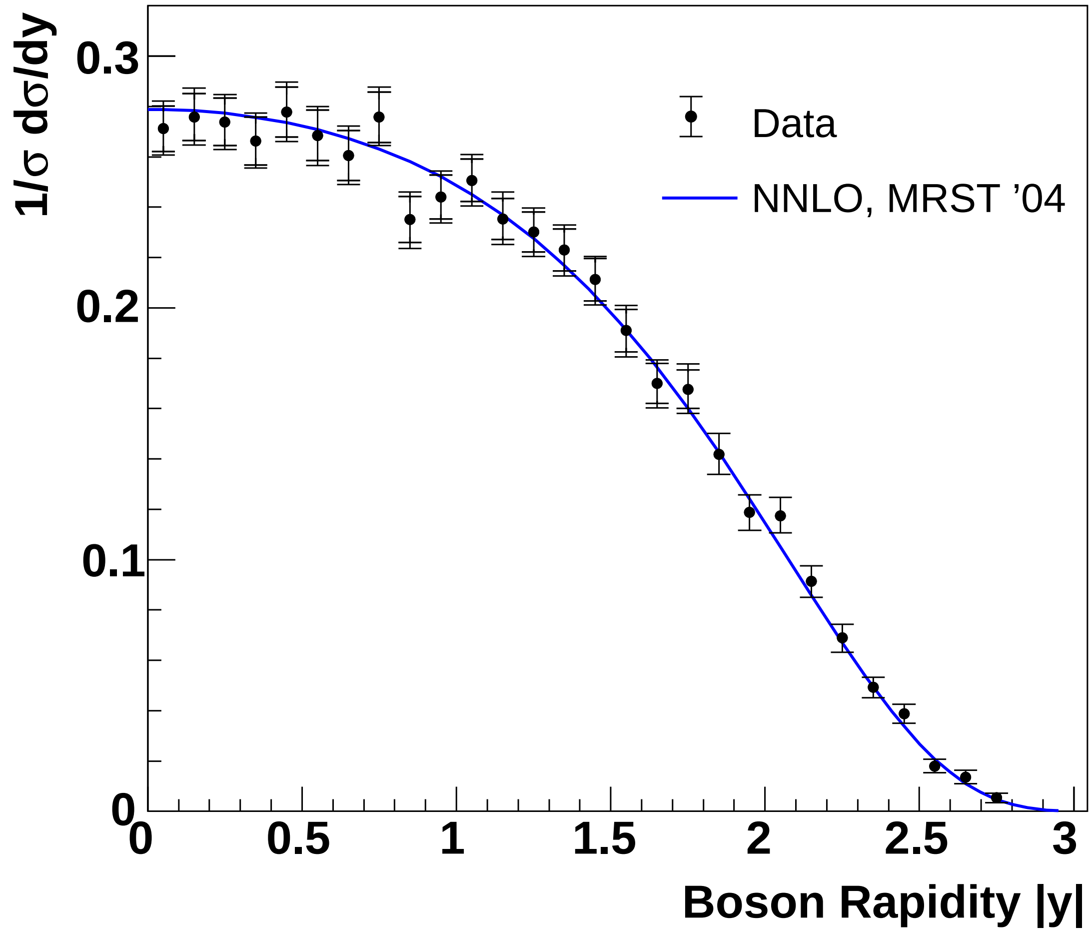

Figure 7.5: Dots are from this measurement.The outer error bars show the total error. Inner error bars show the statistical error alone. The solid line is based on NNLO theoretical calculation based on Anastasiou et al [14] with MRST 2004 PDF.

7.3 Summary

With statistical and systematic uncertainties calculated correctly, differential cross section of Z/γ^* as function of rapidity is shown on FIG 7.5. Result from next to next leading order theory with $MRST$ 2004 PDF is also plotted. The measurement matches theoretical predication well. Table 7.7 shows the values of 1/N dN/dy per $|y|$ bin.

Bin	y	$1/\sigma d\sigma/dy$ ($\pm stat. \pm syst.$)	Corr Unc from Eff	Stat Unc from Eff	PDF Unc	EM Energy Scale Unc	Ve rtex z Unc	Bkgd Unc
1	-2.95	$0.000 \pm 0.000 ^{+0.0000}_{-0.0000}$	$^{+0.0000}_{-0.0000}$	$^{+0.0000}_{-0.0000}$	$^{+0.0000}_{-0.0000}$	$^{+0.0000}_{-0.0000}$	$^{+0.0000}_{-0.0000}$	$\pm$ 0.000
2	-2.85	$0.000 \pm 0.000 ^{+0.0000}_{-0.0000}$	$^{+0.0000}_{-0.0000}$	$^{+0.0000}_{-0.0000}$	$^{+0.0000}_{-0.0000}$	$^{+0.0000}_{-0.0000}$	$^{+0.0000}_{-0.0000}$	$\pm$ 0.000
3	-2.75	$0.004 \pm 0.003 ^{+0.0003}_{-0.0003}$	$^{+0.0000}_{-0.0002}$	$^{+0.0001}_{-0.0001}$	$^{+0.0001}_{-0.0002}$	$^{+0.0002}_{-0.0000}$	$^{+0.0000}_{-0.0001}$	$\pm$ 0.000
4	-2.65	$0.013 \pm 0.004 ^{+0.0005}_{-0.0011}$	$^{+0.0003}_{-0.0004}$	$^{+0.0001}_{-0.0001}$	$^{+0.0004}_{-0.0007}$	$^{+0.0002}_{-0.0005}$	$^{+0.0000}_{-0.0005}$	$\pm$ 0.000
5	-2.55	$0.017 \pm 0.004 ^{+0.0007}_{-0.0008}$	$^{+0.0004}_{-0.0005}$	$^{+0.0001}_{-0.0001}$	$^{+0.0004}_{-0.0005}$	$^{+0.0000}_{-0.0003}$	$^{+0.0002}_{-0.0000}$	$\pm$ 0.000
6	-2.45	$0.038 \pm 0.005 ^{+0.0010}_{-0.0021}$	$^{+0.0005}_{-0.0010}$	$^{+0.0003}_{-0.0003}$	$^{+0.0002}_{-0.0018}$	$^{+0.0002}_{-0.0000}$	$^{+0.0004}_{-0.0001}$	$\pm$ 0.001
7	-2.35	$0.049 \pm 0.005 ^{+0.0021}_{-0.0011}$	$^{+0.0014}_{-0.0008}$	$^{+0.0002}_{-0.0002}$	$^{+0.0014}_{-0.0004}$	$^{+0.0002}_{-0.0002}$	$^{+0.0006}_{-0.0003}$	$\pm$ 0.001
8	-2.25	$0.068 \pm 0.006 ^{+0.0025}_{-0.0020}$	$^{+0.0018}_{-0.0012}$	$^{+0.0002}_{-0.0002}$	$^{+0.0010}_{-0.0011}$	$^{+0.0002}_{-0.0000}$	$^{+0.0008}_{-0.0004}$	$\pm$ 0.001
9	-2.15	$0.094 \pm 0.007 ^{+0.0033}_{-0.0024}$	$^{+0.0016}_{-0.0009}$	$^{+0.0003}_{-0.0003}$	$^{+0.0023}_{-0.0006}$	$^{+0.0000}_{-0.0005}$	$^{+0.0008}_{-0.0013}$	$\pm$ 0.002
10	-2.05	$0.122 \pm 0.009 ^{+0.0031}_{-0.0029}$	$^{+0.0017}_{-0.0020}$	$^{+0.0003}_{-0.0003}$	$^{+0.0021}_{-0.0010}$	$^{+0.0008}_{-0.0001}$	$^{+0.0010}_{-0.0017}$	$\pm$ 0.001
11	-1.95	$0.107 \pm 0.009 ^{+0.0023}_{-0.0031}$	$^{+0.0012}_{-0.0016}$	$^{+0.0002}_{-0.0002}$	$^{+0.0008}_{-0.0017}$	$^{+0.0002}_{-0.0000}$	$^{+0.0000}_{-0.0010}$	$\pm$ 0.002
12	-1.85	$0.138 \pm 0.010 ^{+0.0026}_{-0.0036}$	$^{+0.0011}_{-0.0024}$	$^{+0.0003}_{-0.0003}$	$^{+0.0019}_{-0.0018}$	$^{+0.0004}_{-0.0003}$	$^{+0.0000}_{-0.0013}$	$\pm$ 0.001
13	-1.75	$0.187 \pm 0.012 ^{+0.0043}_{-0.0053}$	$^{+0.0016}_{-0.0034}$	$^{+0.0004}_{-0.0004}$	$^{+0.0028}_{-0.0013}$	$^{+0.0008}_{-0.0006}$	$^{+0.0000}_{-0.0026}$	$\pm$ 0.003
14	-1.65	$0.172 \pm 0.012 ^{+0.0043}_{-0.0038}$	$^{+0.0030}_{-0.0019}$	$^{+0.0003}_{-0.0003}$	$^{+0.0028}_{-0.0016}$	$^{+0.0006}_{-0.0007}$	$^{+0.0000}_{-0.0024}$	$\pm$ 0.001
15	-1.55	$0.206 \pm 0.012 ^{+0.0044}_{-0.0042}$	$^{+0.0037}_{-0.0027}$	$^{+0.0004}_{-0.0004}$	$^{+0.0014}_{-0.0024}$	$^{+0.0006}_{-0.0012}$	$^{+0.0000}_{-0.0008}$	$\pm$ 0.002
16	-1.45	$0.210 \pm 0.012 ^{+0.0058}_{-0.0028}$	$^{+0.0044}_{-0.0019}$	$^{+0.0004}_{-0.0004}$	$^{+0.0035}_{-0.0009}$	$^{+0.0004}_{-0.0009}$	$^{+0.0000}_{-0.0008}$	$\pm$ 0.001
17	-1.35	$0.219 \pm 0.012 ^{+0.0051}_{-0.0044}$	$^{+0.0030}_{-0.0027}$	$^{+0.0003}_{-0.0003}$	$^{+0.0031}_{-0.0013}$	$^{+0.0008}_{-0.0002}$	$^{+0.0003}_{-0.0021}$	$\pm$ 0.002
18	-1.25	$0.232 \pm 0.011 ^{+0.0043}_{-0.0037}$	$^{+0.0036}_{-0.0025}$	$^{+0.0004}_{-0.0004}$	$^{+0.0020}_{-0.0008}$	$^{+0.0000}_{-0.0004}$	$^{+0.0003}_{-0.0023}$	$\pm$ 0.001
19	-1.15	$0.246 \pm 0.012 ^{+0.0035}_{-0.0054}$	$^{+0.0027}_{-0.0038}$	$^{+0.0004}_{-0.0004}$	$^{+0.0013}_{-0.0024}$	$^{+0.0004}_{-0.0005}$	$^{+0.0011}_{-0.0027}$	$\pm$ 0.001
20	-1.05	$0.239 \pm 0.012 ^{+0.0049}_{-0.0048}$	$^{+0.0038}_{-0.0027}$	$^{+0.0004}_{-0.0004}$	$^{+0.0019}_{-0.0020}$	$^{+0.0003}_{-0.0001}$	$^{+0.0011}_{-0.0026}$	$\pm$ 0.002
21	-0.95	$0.256 \pm 0.013 ^{+0.0043}_{-0.0043}$	$^{+0.0026}_{-0.0039}$	$^{+0.0004}_{-0.0004}$	$^{+0.0032}_{-0.0014}$	$^{+0.0003}_{-0.0005}$	$^{+0.0009}_{-0.0000}$	$\pm$ 0.001
22	-0.85	$0.230 \pm 0.013 ^{+0.0063}_{-0.0040}$	$^{+0.0030}_{-0.0031}$	$^{+0.0004}_{-0.0004}$	$^{+0.0046}_{-0.0007}$	$^{+0.0017}_{-0.0000}$	$^{+0.0008}_{-0.0000}$	$\pm$ 0.002
23	-0.75	$0.299 \pm 0.015 ^{+0.0035}_{-0.0071}$	$^{+0.0026}_{-0.0054}$	$^{+0.0005}_{-0.0005}$	$^{+0.0009}_{-0.0040}$	$^{+0.0012}_{-0.0002}$	$^{+0.0013}_{-0.0017}$	$\pm$ 0.001
24	-0.65	$0.255 \pm 0.014 ^{+0.0048}_{-0.0055}$	$^{+0.0028}_{-0.0048}$	$^{+0.0005}_{-0.0005}$	$^{+0.0031}_{-0.0010}$	$^{+0.0001}_{-0.0004}$	$^{+0.0011}_{-0.0014}$	$\pm$ 0.002
25	-0.55	$0.281 \pm 0.014 ^{+0.0056}_{-0.0051}$	$^{+0.0040}_{-0.0034}$	$^{+0.0005}_{-0.0005}$	$^{+0.0022}_{-0.0029}$	$^{+0.0017}_{-0.0003}$	$^{+0.0013}_{-0.0000}$	$\pm$ 0.002
26	-0.45	$0.266 \pm 0.014 ^{+0.0056}_{-0.0054}$	$^{+0.0046}_{-0.0031}$	$^{+0.0004}_{-0.0004}$	$^{+0.0017}_{-0.0036}$	$^{+0.0005}_{-0.0002}$	$^{+0.0012}_{-0.0000}$	$\pm$ 0.002
27	-0.35	$0.285 \pm 0.014 ^{+0.0053}_{-0.0058}$	$^{+0.0049}_{-0.0037}$	$^{+0.0005}_{-0.0005}$	$^{+0.0008}_{-0.0037}$	$^{+0.0002}_{-0.0003}$	$^{+0.0003}_{-0.0016}$	$\pm$ 0.002
28	-0.25	$0.267 \pm 0.013 ^{+0.0053}_{-0.0045}$	$^{+0.0042}_{-0.0036}$	$^{+0.0004}_{-0.0004}$	$^{+0.0028}_{-0.0008}$	$^{+0.0008}_{-0.0017}$	$^{+0.0003}_{-0.0015}$	$\pm$ 0.001
29	-0.15	$0.287 \pm 0.013 ^{+0.0061}_{-0.0066}$	$^{+0.0053}_{-0.0038}$	$^{+0.0005}_{-0.0005}$	$^{+0.0017}_{-0.0029}$	$^{+0.0016}_{-0.0005}$	$^{+0.0011}_{-0.0043}$	$\pm$ 0.001
30	-0.05	$0.267 \pm 0.013 ^{+0.0050}_{-0.0069}$	$^{+0.0040}_{-0.0048}$	$^{+0.0004}_{-0.0004}$	$^{+0.0020}_{-0.0025}$	$^{+0.0011}_{-0.0003}$	$^{+0.0010}_{-0.0040}$	$\pm$ 0.001

Table 7.4: $1/\sigma d\sigma/dy$ per rapidity bin, with uncertainties

Bin	y	$1/\sigma d\sigma/dy$ ($\pm stat. \pm syst.$)	Corr Unc from Eff	Stat Unc from Eff	PDF Unc	EM Energy Scale Unc	Ve rtex z Unc	Bkgd Unc
31	0.05	$0.276 \pm 0.013\ ^{+0.0055}_{-0.0059}$	$^{+0.0040}_{-0.0041}$	$^{+0.0005}_{-0.0005}$	$^{+0.0027}_{-0.0023}$	$^{+0.0009}_{-0.0000}$	$^{+0.0022}_{-0.0033}$	$\pm$ 0.001
32	0.15	$0.265 \pm 0.013\ ^{+0.0050}_{-0.0063}$	$^{+0.0035}_{-0.0043}$	$^{+0.0005}_{-0.0005}$	$^{+0.0020}_{-0.0025}$	$^{+0.0003}_{-0.0008}$	$^{+0.0021}_{-0.0032}$	$\pm$ 0.002
33	0.25	$0.281 \pm 0.013\ ^{+0.0055}_{-0.0057}$	$^{+0.0042}_{-0.0046}$	$^{+0.0005}_{-0.0005}$	$^{+0.0024}_{-0.0017}$	$^{+0.0007}_{-0.0003}$	$^{+0.0020}_{-0.0026}$	$\pm$ 0.001
34	0.35	$0.250 \pm 0.013\ ^{+0.0042}_{-0.0057}$	$^{+0.0030}_{-0.0046}$	$^{+0.0004}_{-0.0004}$	$^{+0.0022}_{-0.0023}$	$^{+0.0003}_{-0.0006}$	$^{+0.0018}_{-0.0023}$	$\pm$ 0.001
35	0.45	$0.290 \pm 0.014\ ^{+0.0055}_{-0.0061}$	$^{+0.0032}_{-0.0052}$	$^{+0.0005}_{-0.0005}$	$^{+0.0029}_{-0.0028}$	$^{+0.0010}_{-0.0002}$	$^{+0.0029}_{-0.0005}$	$\pm$ 0.001
36	0.55	$0.258 \pm 0.013\ ^{+0.0062}_{-0.0043}$	$^{+0.0034}_{-0.0037}$	$^{+0.0004}_{-0.0004}$	$^{+0.0036}_{-0.0008}$	$^{+0.0020}_{-0.0012}$	$^{+0.0026}_{-0.0004}$	$\pm$ 0.002
37	0.65	$0.266 \pm 0.013\ ^{+0.0047}_{-0.0055}$	$^{+0.0031}_{-0.0038}$	$^{+0.0004}_{-0.0004}$	$^{+0.0015}_{-0.0029}$	$^{+0.0022}_{-0.0001}$	$^{+0.0000}_{-0.0015}$	$\pm$ 0.002
38	0.75	$0.257 \pm 0.013\ ^{+0.0048}_{-0.0047}$	$^{+0.0033}_{-0.0028}$	$^{+0.0004}_{-0.0004}$	$^{+0.0019}_{-0.0023}$	$^{+0.0013}_{-0.0004}$	$^{+0.0000}_{-0.0014}$	$\pm$ 0.002
39	0.85	$0.240 \pm 0.012\ ^{+0.0045}_{-0.0053}$	$^{+0.0025}_{-0.0041}$	$^{+0.0004}_{-0.0004}$	$^{+0.0019}_{-0.0013}$	$^{+0.0000}_{-0.0006}$	$^{+0.0007}_{-0.0006}$	$\pm$ 0.003
40	0.95	$0.234 \pm 0.011\ ^{+0.0049}_{-0.0045}$	$^{+0.0029}_{-0.0031}$	$^{+0.0003}_{-0.0003}$	$^{+0.0028}_{-0.0009}$	$^{+0.0000}_{-0.0015}$	$^{+0.0007}_{-0.0006}$	$\pm$ 0.003
41	1.05	$0.261 \pm 0.011\ ^{+0.0047}_{-0.0061}$	$^{+0.0032}_{-0.0035}$	$^{+0.0003}_{-0.0003}$	$^{+0.0014}_{-0.0033}$	$^{+0.0009}_{-0.0006}$	$^{+0.0025}_{-0.0033}$	$\pm$ 0.001
42	1.15	$0.227 \pm 0.010\ ^{+0.0053}_{-0.0063}$	$^{+0.0024}_{-0.0034}$	$^{+0.0003}_{-0.0003}$	$^{+0.0018}_{-0.0028}$	$^{+0.0014}_{-0.0000}$	$^{+0.0022}_{-0.0029}$	$\pm$ 0.003
43	1.25	$0.229 \pm 0.010\ ^{+0.0054}_{-0.0044}$	$^{+0.0026}_{-0.0029}$	$^{+0.0003}_{-0.0003}$	$^{+0.0029}_{-0.0009}$	$^{+0.0014}_{-0.0002}$	$^{+0.0025}_{-0.0022}$	$\pm$ 0.002
44	1.35	$0.226 \pm 0.011\ ^{+0.0056}_{-0.0042}$	$^{+0.0035}_{-0.0028}$	$^{+0.0003}_{-0.0003}$	$^{+0.0029}_{-0.0010}$	$^{+0.0004}_{-0.0004}$	$^{+0.0025}_{-0.0022}$	$\pm$ 0.002
45	1.45	$0.213 \pm 0.011\ ^{+0.0053}_{-0.0034}$	$^{+0.0044}_{-0.0023}$	$^{+0.0004}_{-0.0004}$	$^{+0.0016}_{-0.0021}$	$^{+0.0003}_{-0.0005}$	$^{+0.0020}_{-0.0000}$	$\pm$ 0.001
46	1.55	$0.179 \pm 0.011\ ^{+0.0055}_{-0.0042}$	$^{+0.0038}_{-0.0028}$	$^{+0.0003}_{-0.0003}$	$^{+0.0015}_{-0.0012}$	$^{+0.0011}_{-0.0000}$	$^{+0.0017}_{-0.0000}$	$\pm$ 0.003
47	1.65	$0.169 \pm 0.010\ ^{+0.0047}_{-0.0043}$	$^{+0.0032}_{-0.0016}$	$^{+0.0003}_{-0.0003}$	$^{+0.0016}_{-0.0012}$	$^{+0.0012}_{-0.0000}$	$^{+0.0008}_{-0.0027}$	$\pm$ 0.003
48	1.75	$0.155 \pm 0.009\ ^{+0.0042}_{-0.0047}$	$^{+0.0020}_{-0.0024}$	$^{+0.0003}_{-0.0003}$	$^{+0.0019}_{-0.0012}$	$^{+0.0004}_{-0.0001}$	$^{+0.0007}_{-0.0025}$	$\pm$ 0.003
49	1.85	$0.144 \pm 0.008\ ^{+0.0037}_{-0.0044}$	$^{+0.0010}_{-0.0031}$	$^{+0.0002}_{-0.0002}$	$^{+0.0011}_{-0.0015}$	$^{+0.0010}_{-0.0005}$	$^{+0.0022}_{-0.0014}$	$\pm$ 0.002
50	1.95	$0.127 \pm 0.007\ ^{+0.0036}_{-0.0027}$	$^{+0.0022}_{-0.0016}$	$^{+0.0002}_{-0.0002}$	$^{+0.0014}_{-0.0009}$	$^{+0.0005}_{-0.0001}$	$^{+0.0019}_{-0.0012}$	$\pm$ 0.002
51	2.05	$0.115 \pm 0.007\ ^{+0.0030}_{-0.0045}$	$^{+0.0015}_{-0.0019}$	$^{+0.0002}_{-0.0002}$	$^{+0.0003}_{-0.0028}$	$^{+0.0011}_{-0.0000}$	$^{+0.0008}_{-0.0020}$	$\pm$ 0.002
52	2.15	$0.090 \pm 0.006\ ^{+0.0032}_{-0.0029}$	$^{+0.0019}_{-0.0010}$	$^{+0.0002}_{-0.0002}$	$^{+0.0013}_{-0.0008}$	$^{+0.0004}_{-0.0002}$	$^{+0.0006}_{-0.0015}$	$\pm$ 0.002
53	2.25	$0.070 \pm 0.005\ ^{+0.0031}_{-0.0026}$	$^{+0.0015}_{-0.0010}$	$^{+0.0002}_{-0.0002}$	$^{+0.0012}_{-0.0004}$	$^{+0.0002}_{-0.0004}$	$^{+0.0014}_{-0.0009}$	$\pm$ 0.002
54	2.35	$0.050 \pm 0.005\ ^{+0.0018}_{-0.0017}$	$^{+0.0010}_{-0.0011}$	$^{+0.0002}_{-0.0002}$	$^{+0.0007}_{-0.0005}$	$^{+0.0001}_{-0.0004}$	$^{+0.0010}_{-0.0007}$	$\pm$ 0.001
55	2.45	$0.039 \pm 0.004\ ^{+0.0018}_{-0.0010}$	$^{+0.0006}_{-0.0008}$	$^{+0.0002}_{-0.0002}$	$^{+0.0016}_{-0.0001}$	$^{+0.0005}_{-0.0000}$	$^{+0.0003}_{-0.0000}$	$\pm$ 0.000
56	2.55	$0.019 \pm 0.003\ ^{+0.0006}_{-0.0009}$	$^{+0.0003}_{-0.0006}$	$^{+0.0001}_{-0.0001}$	$^{+0.0004}_{-0.0006}$	$^{+0.0002}_{-0.0000}$	$^{+0.0002}_{-0.0000}$	$\pm$ 0.000
57	2.65	$0.014 \pm 0.003\ ^{+0.0007}_{-0.0008}$	$^{+0.0004}_{-0.0006}$	$^{+0.0001}_{-0.0001}$	$^{+0.0004}_{-0.0005}$	$^{+0.0001}_{-0.0001}$	$^{+0.0004}_{-0.0000}$	$\pm$ 0.000
58	2.75	$0.007 \pm 0.003\ ^{+0.0005}_{-0.0004}$	$^{+0.0001}_{-0.0003}$	$^{+0.0001}_{-0.0001}$	$^{+0.0005}_{-0.0001}$	$^{+0.0001}_{-0.0001}$	$^{+0.0002}_{-0.0000}$	$\pm$ 0.000
59	2.85	$0.000 \pm 0.000\ ^{+0.0000}_{-0.0000}$	$^{+0.0000}_{-0.0000}$	$^{+0.0000}_{-0.0000}$	$^{+0.0000}_{-0.0000}$	$^{+0.0000}_{-0.0000}$	$^{+0.0000}_{-0.0000}$	$\pm$ 0.000
60	2.95	$0.000 \pm 0.000\ ^{+0.0000}_{-0.0000}$	$^{+0.0000}_{-0.0000}$	$^{+0.0000}_{-0.0000}$	$^{+0.0000}_{-0.0000}$	$^{+0.0000}_{-0.0000}$	$^{+0.0000}_{-0.0000}$	$\pm$ 0.000

Table 7.5: $1/\sigma d\sigma/dy$ per rapidity bin, with uncertainties

Table 7.6: Parameters for folding differential cross section

p_0	p_1	p_2	p_3	p_4	p_5	p_6	p_7	p_8
69.489403	0.486850	-7.536885	-1.570841	2.109438	0.057027	-2.273616	1.210376	-0.172999

Table 7.7: $1/\sigma d\sigma/dy$ per $|y|$ bin with invariant mass between $71 < M_{ee} < 111$ GeV.

Bin	$\lvert y\rvert$	$1/\sigma d\sigma/dy(\pm stat. \pm syst.)$
1	0.05	0.271 $\pm$ 0.009 $\pm$0.007
2	0.15	0.276 $\pm$ 0.009 $\pm$0.006
3	0.25	0.274 $\pm$ 0.009 $\pm$0.005
4	0.35	0.266 $\pm$ 0.010 $\pm$0.005
5	0.45	0.278 $\pm$ 0.010 $\pm$0.006
6	0.55	0.269 $\pm$ 0.010 $\pm$0.005
7	0.65	0.260 $\pm$ 0.010 $\pm$0.006
8	0.75	0.276 $\pm$ 0.010 $\pm$0.007
9	0.85	0.235 $\pm$ 0.009 $\pm$0.006
10	0.95	0.244 $\pm$ 0.009 $\pm$0.004
11	1.05	0.251 $\pm$ 0.008 $\pm$0.005
12	1.15	0.235 $\pm$ 0.008 $\pm$0.005
13	1.25	0.230 $\pm$ 0.008 $\pm$0.004
14	1.35	0.223 $\pm$ 0.008 $\pm$0.005
15	1.45	0.211 $\pm$ 0.008 $\pm$0.006
16	1.55	0.191 $\pm$ 0.008 $\pm$0.004
17	1.65	0.170 $\pm$ 0.008 $\pm$0.004
18	1.75	0.168 $\pm$ 0.008 $\pm$0.005
19	1.85	0.142 $\pm$ 0.007 $\pm$0.004
20	1.95	0.119 $\pm$ 0.006 $\pm$0.003
21	2.05	0.117 $\pm$ 0.006 $\pm$0.003
22	2.15	0.091 $\pm$ 0.005 $\pm$0.003
23	2.25	0.069 $\pm$ 0.004 $\pm$0.003
24	2.35	0.049 $\pm$ 0.004 $\pm$0.002
25	2.45	0.039 $\pm$ 0.003 $\pm$0.002
26	2.55	0.018 $\pm$ 0.003 $\pm$0.001
27	2.65	0.014 $\pm$ 0.003 $\pm$0.001
28	2.75	0.005 $\pm$ 0.002 $\pm$0.0004

Chapter 8
Discussions and Conclusions

In order to know how well the data and theory in agreement, the next to next leading order theory with different PDF sets is presented in this chapter. The author gives a side by side comparison with data and theory. Conclusions and discussions are also given at the end of this chapter.

8.1 Differential cross section from theoretical calculation

In the next to next leading order theoretical calculation, center of mass energy is set to $\sqrt{s} = 1.96$ TeV. Number of light quark flavor is 5, and $\alpha_t = 1/128$ to consist with Tevatron parameters. Table 8.1 shows specific value of α_s used with different PDF sets. The next to next leading order theory is based on *Anastasiou, et al* [14]. In all calculations, Z boson invariant mass window is 71 to 111 GeV.

The next to next leading order theoretical calculation predicts different values of cross section with different PDF inputs: 239.375 *pb* by using CTEQ6M, 248.856 *pb* by using MRST2004 and 260.602 *pb* by using the latest Alekhin PDF set. But there are only slightly differences in shape of rapidity distributions.

Because Monte Carlo generator *RESBOS* used in this analysis is a next leading order events generator, K factors are shown on FIG 8.3, 8.4 and 8.5. These plots show the differences between the next leading order and the next to next leading order results. Table 8.2 shows the total cross section from theoretical calculation with different PDF sets.

8.2 The χ^2 test between data and theory [34]

Results from theoretical calculations using different PDF sets are compared with this measurement using χ^2 *Goodness-of-Fit* test. χ^2 between experiment and theory is defined as following:

	CTEQ6M	*CTEQ6L*	*LO MRST*	*NLO MRST*	*NNLO MRST*
α_s	0.118	0.130	0.130	0.119	0.1155

Table 8.1: Specific α_s values used in theoretical calculation with different PDF sets

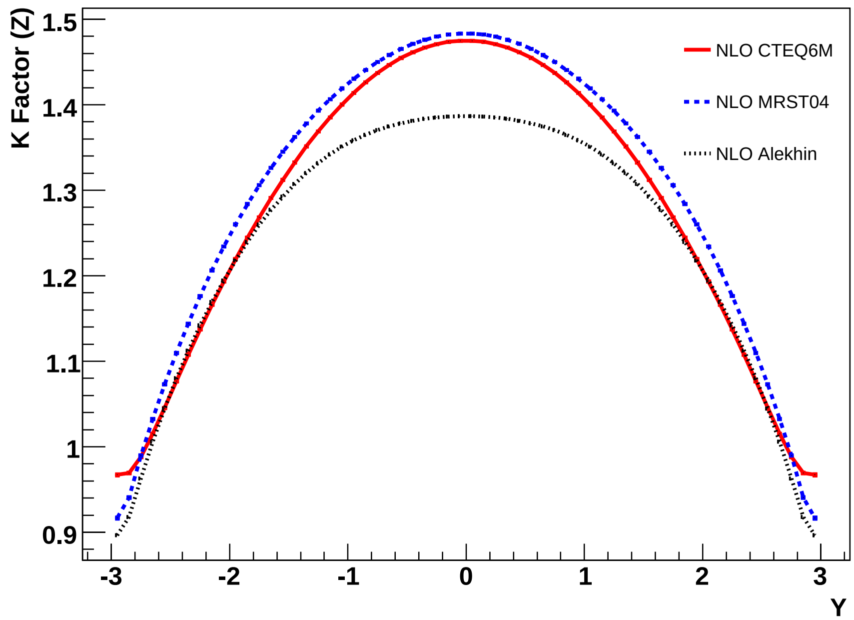

Figure 8.1: Difference in ratio from NLO to LO, using different PDF input with theoretical calculation

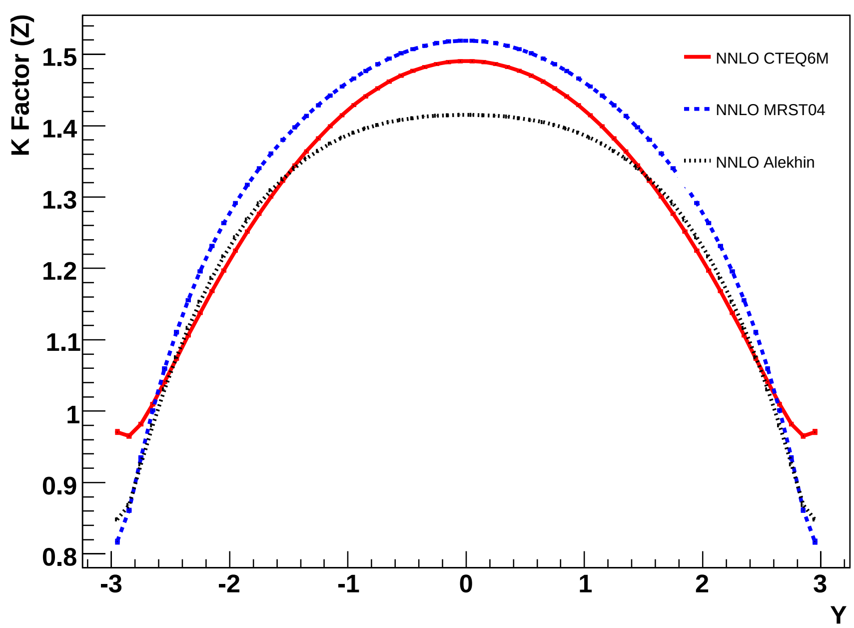

Figure 8.2: Difference in ratio from NNLO to LO, using different PDF input with theoretical calculation

Cross Section	*CTEQ6*	*MRST*	*Alekhin*
LO	172.928	174.182	192.576
NLO	237.249	242.989	255.073
NNLO	239.375	248.856	260.602

Table 8.2: Total cross section with different PDF sets from theoretical calculation, note in NNLO calculation, NLO CTEQ PDF (CETQ6M) is used

$$\chi^2 = \sum_{i=1}^{n} \frac{(N_i^{exp} - N_i^{theory})^2}{(\delta N_i^{theory})^2} \tag{8.1}$$

Where n is number of data bins, N_i^{exp} is number of events observed at i-th bin and N_i^{theory} is number of events predicted by theory at bin center. In order to judge how good that the differential cross section predicted by theory in agreement with experimental data, a simple relationship between number of events N_i and differential cross section $\sigma_i = 1/N_i dN_i/dy$ is assumed:

$$\sigma_i = \alpha_i N_i \tag{8.2}$$

Under this assumption, uncertainty of experimental measurement $\delta\sigma_i^{exp} = \alpha\sqrt{N_i^{exp}}$. Equation 8.1 can be rewritten as:

$$\chi^2 = \sum_{i=1}^{n} (\frac{\sigma_i^{theory} - \sigma_i^{exp}}{\delta\sigma_i^{exp}})^2 \frac{\sigma_i^{exp}}{\sigma_i^{theory}} \tag{8.3}$$

Notice in equation 8.3 uncertainty from theory disappears.

The theoretical result is calculated with PDF sets from MRST2004 (NNLO, NLO, LO), CTEQ6M (NLO), CTEQ6L (LO), and Alekhin (NNLO, NLO, LO). Since CTEQ6 does not provide NNLO PDF, NNLO theoretical calculation with CTEQ still uses NLO CTEQ6M. χ^2 test results of data and theoretical calculation are shown on TABLE 8.3.

χ^2	*CTEQ6*	*MRST*	*Alekhin*
LO	54.9044	34.1234	36.0688
NLO	11.0689	12.4222	11.0968
NNLO	11.2143	13.0108	11.5376

Table 8.3: χ^2 test results between data and theory with various PDF inputs, $ndf = 28$

χ^2 test results indicate, at the leading order calculation, MRST PDF provides the best match

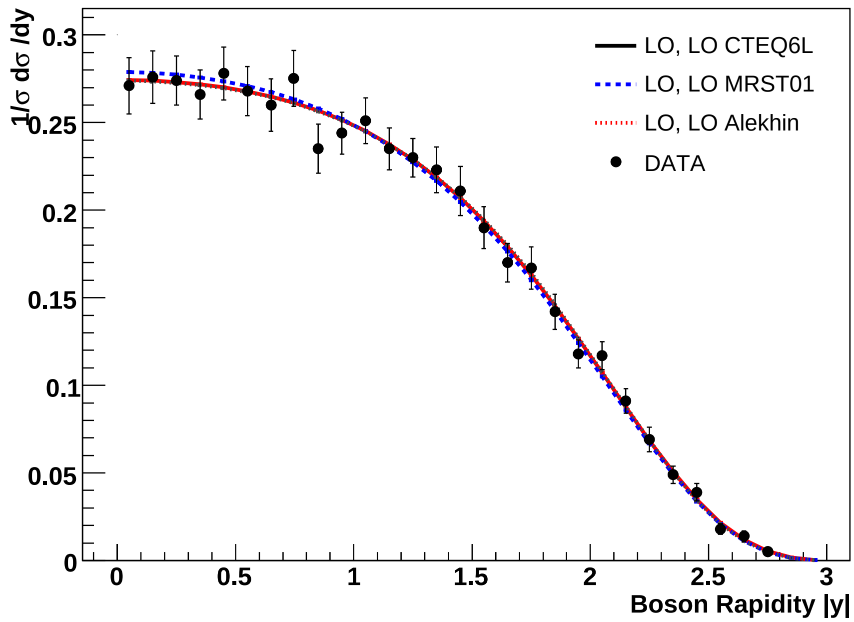

Figure 8.3: $1/\sigma d\sigma/\mathrm{dy}$ plot from data, the leading order theoretical calculation with the leading order MRST2001, Alekhin and CTEQ6L PDF sets.

to the data. With the next to next leading order calculation, CTEQ and Alekhin results both show better agreement with data than MRST's. With the next to next leading order calculation, CTEQ provides the best result. FIG 8.3, FIG 8.4, FIG 8.5 also support the results from χ^2 test.

Fig 8.3 compares ratio of differential cross section from data to the leading order calculation with the leading order PDF sets. FIG 8.4 shows the shapes from the next to leading order calculation. FIG 8.5 shows the shapes from the next to next leading order calculation. The results with different PDF inputs are all similar in shape. This indicates the shape of rapidity distribution is not sensitive to PDFs.

Although different PDF inputs predict different values of the total cross section in theoretical calculation (FIG 8.6), but their shapes are not sensitive to PDFs. In order to use this data to test the PDFs, it is necessary to obtain high quality luminosity value to determine the total cross section.

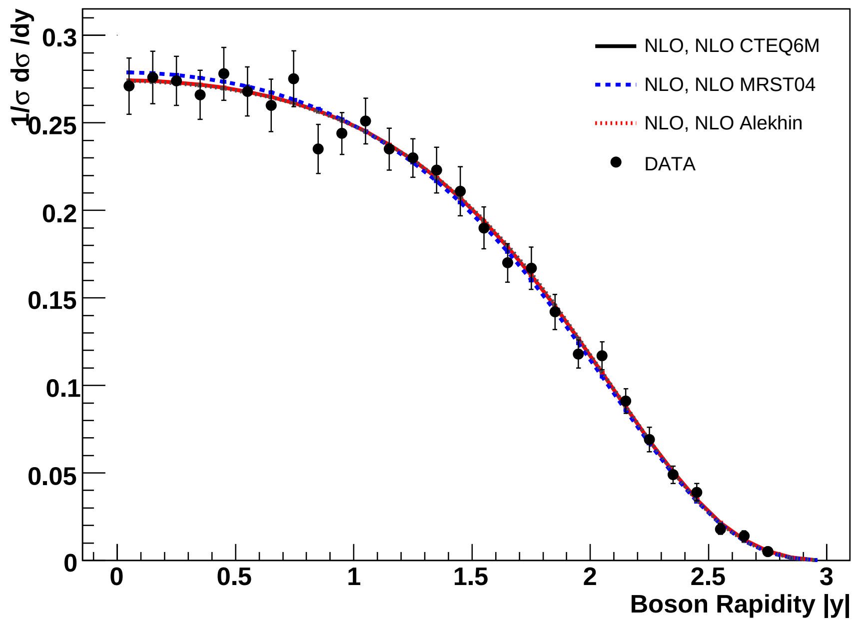

Figure 8.4: $1/\sigma \mathrm{d}\sigma/\mathrm{dy}$ plot from data, the next to leading order theoretical calculation with the next to leading order MRST2004, Alekhin, and CTEQ6M PDF sets.

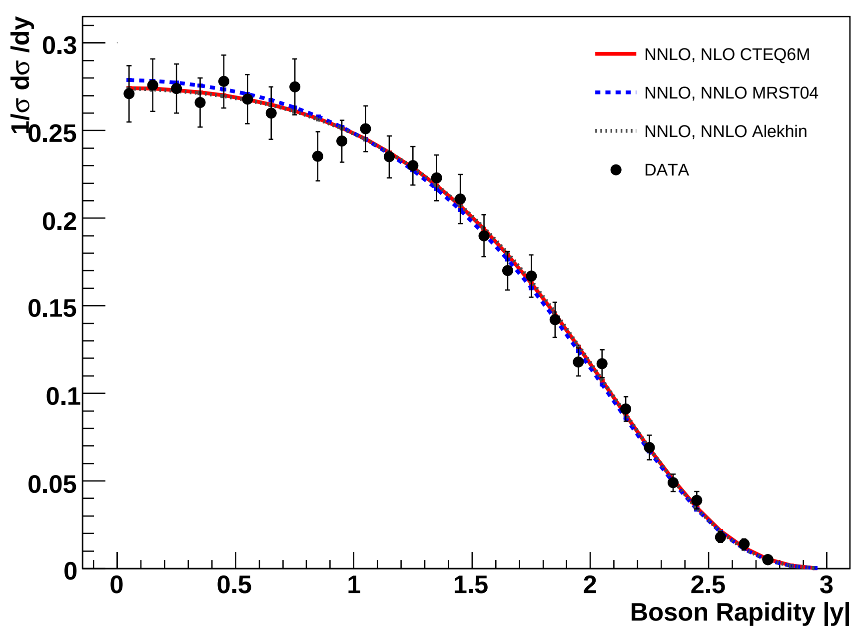

Figure 8.5: $1/\sigma \mathrm{d}\sigma/\mathrm{dy}$ plot from data, the next to next leading order theoretical calculation with the next to next leading order MRST2004, Alekhin, and the next leading order CTEQ6M PDF sets

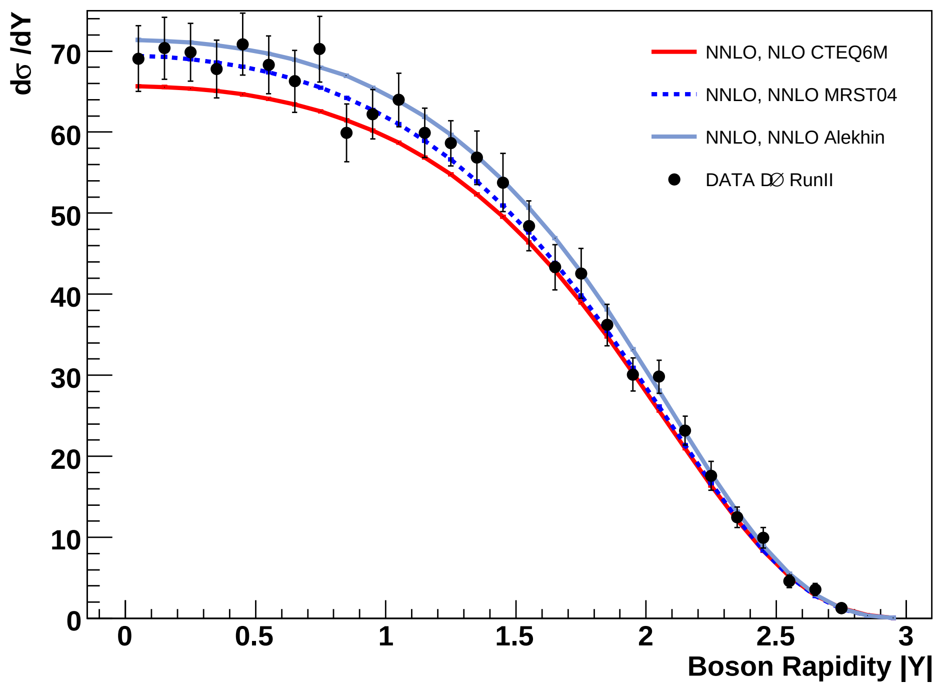

Figure 8.6: dσ/dy plot from data, the next to next leading order theoretical calculation with the next to next leading order MRST2004, Alekhin, and the next leading order CTEQ6M PDF sets

8.3 Further discussions

Theorists suggest that there is difference on the P_T distribution for high rapidity and low rapidity Z bosons [35]. However, with the current amount of events, it is hard to favor one PDF set over another by comparing the difference between theory and the measurement. It is even harder to observe the difference in P_T spectrum between the low and high rapidity Z bosons. With increased luminosity and reduced luminosity uncertainty in the near future at $D\O$, $Z/\gamma^* \rightarrow e^+e^-$ differential cross section measurement will be a useful tool to test the PDFs.

8.4 Conclusions

The ratio of differential cross section distribution $1/\sigma d\sigma/dy$ of e^+e^- pair at 71 to 111 GeV Z boson mass range has been measured at center of mass energy $\sqrt{s} = 1.96$ TeV. The results agree well with the next to next leading order theoretical predictions with different PDF sets. With the increased total luminosity and improved accuracy in luminosity measurement, the measurement of differential cross section distribution can provide an important tool to better understand the parton distribution functions and the next to next leading order theoretical calculation.

Bibliography

[1] See website: http://www-d0.fnal.gov

[2] S. Avachi, et al., Nucl. Instrum. Meth. A **338**, 185 (1994)

[3] S. Alekhin, JETP Lett. 82(2005), 628, and Phys. Rev. D **68**, 014002 (2003)

[4] J. Pumplin, D. R. Stump, J. Huston, H. L. Lai, P. Nadolsky, W. K. Tung, JHEP **0207** 012 (2002)

[5] A. D. Martin, R. G. Roberts, W. J. Stirling, R. S. Thorne, Phys. Lett. B **604** 61 (2004)

[6] Vrap source code: http://www.slac.stanford.edu/~lance/Vrap/

[7] *DØ* Collaboration, Phys. Rev. Lett. **86** 1707 (2001), and Phys. Rev. D **64** 032003 (2001)

[8] A. Martin, R. Roberts, W. Stirling, R. Thorne, Eur. Phys. J. C **28** 455 2003

[9] CTEQ Collaboration: J. Pumpin et al., JHEP **0207** 012 (2002)

[10] E. Eichten, K. Lane, M. Peskin, Phys. Rev. Lett. **50** 811 (1983)

[11] F. Abe, et al., Phys. Rev. Lett. **77** 5336 (1996)

[12] B. Abbott et al., Phys. Rev. Lett. **82** 2457 (1999)

[13] C. Balzs, J. Qiu and C. -P. Yuan, Phys. Lett. B **355** 548 (1995)

[14] C. Anastasiou, L. Dixon, K. Melnikov, F. Petriello, Phys. Rev. D **69**, 094008 (2004)

[15] Thomas Nunnemann, *DØ* Internal Note 4476

[16] *DØ* Collaboration, Nucl. Instr. Meth. A**338** 185 (1994)

[17] *DØ* Collaboration, Nucl. Instr. Meth. A **565** 463 (2006)

[18] Ming Yan, *DØ* Internal Note 4047

[19] Bad run and LBN list by *DØ* Jet/Met Group

[20] *DØ* Official Run Database by *DØ* data quality coordination

[21] C. Balazs and C. P. Yuan, Phys. Rev. D **56**, 5558 (1997)

[22] P. Golonka, Z. Was, Eur. Phys. J. C **45**, 97 (2006)

[23] Sarah Eno, Marco Verzocchi, *DØ* Internal Note 4165

[24] Jan Stark, Understanding and modeling the CAL energy resolution, a presentation at the *DØ* W Mass meeting, January 13, 2006.

[25] T. Sjostrand, S. Mrenna, P. Skands, JHEP **0605** 026 (2006)

[26] J. M. Campbell and R. K. Ellis, Phys. Rev. D **60**, 113006 (1999)

[27] Oleksiy Atramentov et. al., *DØ* Internal Note 4976

[28] M. Cacciari, S. Frixione, M. L. Mangano, P. Nason, and G. Ridolfi, JHEP **04**, 068 (2004)

[29] R. Bonciani, S. Catani, M. L. Mangano, and P. Pason, Nucl. Phys. B **529**, 424 (1998)

[30] S. Catani, M. L. Mangano, P. Nason, and L. Trenradue, Phys. Lett. B **378**, 329 (1996)

[31] Sean Mattingly and Andrew Askew, *DØ* Internal Note 4686

[32] G. D. Lafferty, and T. R. Wyatt, Nucl. Instrum. Meth. A **355**, 541 (1995)

[33] *DØ* Collaboration, hep-ex/0702025; FERMILAB-Pub-07-040-E

[34] H. Wojciechowski, Phys Rev C **72** 044601 (2005)

[35] S. Berge, P. Nadolsky, F. Olness, C.-P. Yuan, Phys. Rev. D **72** 033015 (2005)